DISSERTATION

IGNITION AND COMBUSTION OF LIQUID HYDROCARBON DROPLETS IN PREMIXED FUEL/AIR MIXTURES AT ELEVATED PRESSURES AND TEMPERATURES

Submitted by

Siddhesh Bharat Bhoite

Department of Mechanical Engineering

In partial fulfillment of the requirements

For the Degree of Doctor of Philosophy

Colorado State University

Fort Collins, Colorado

Fall 2022

Doctoral Committee:

Advisor: Bret Windom
Co-Advisor: Anthony J. Marchese

Daniel B. Olsen
Karan Venayagamoorthy

ABSTRACT

IGNITION AND COMBUSTION OF LIQUID HYDROCARBON DROPLETS IN PREMIXED FUEL/AIR MIXTURES AT ELEVATED PRESSURES AND TEMPERATURES

The combustion of two fuels with disparate reactivity such as natural gas and diesel in internal combustion engines has the potential to increase fuel efficiency, reduce fuel costs and reduce pollutant formation in comparison to traditional diesel or spark-ignited engines. However, dual-fuel engines are presently constrained by uncontrolled fast combustion (i.e., engine knock) as well as incomplete combustion and a better understanding of dual-fuel combustion processes is necessary to overcome these challenges. In addition to dual-fuel engines, this work is also motivated by abnormal combustion phenomenon that has been observed in highly boosted, spark ignited, natural gas engines, which is caused by engine lubricant oil droplets entering the cylinder and serving as unwanted ignition sources for the natural gas/air mixture. To study the fundamental combustion processes of ignition and flame propagation in dual-fuel engines and abnormal combustion triggered by lubricant oil droplets, single isolated liquid hydrocarbon droplets were injected into premixed CH_4/O_2/Inert mixtures at elevated temperatures and pressures.

In this research, a rapid compression machine (RCM) was used in combination with a newly developed piezoelectric droplet injection system that is capable of injecting single liquid hydrocarbon droplets of 40 to 500 μm along the stagnation plane of the RCM combustion chamber. A high-speed Schlieren optical setup was used for imaging the combustion events in the chamber. Experiments were conducted for diesel fuel and lubricant oil droplets at various initial diameters

(50 μm < d_o < 500 μm), various CH_4/O_2/Inert equivalence ratios (0 < ϕ < 1.2) and various compressed temperatures (740 K < T_c < 1000 K).

Dual fuel experiments revealed multiple modes of droplet ignition, droplet combustion, and premixed flame propagation, which depend on the initial droplet temperature, droplet diameter, droplet velocity, and stoichiometry of the $CH_4/O_2/N_2$/Ar mixture. In the case of small droplets, spherical ignition events were observed that transition into spherical non-premixed flames that envelope the droplet, producing an outwardly propagating spherical premixed flame. For larger droplet diameters moving at moderate velocity, the ignition event occurs near the droplet surface on the leeward side of the droplet and subsequently creates a non-premixed flame that envelopes the droplet and a non-spherical premixed flame. For droplets moving with high velocities, the ignition event occurs in the wake of the droplet, multiple diameters from the droplet surface, and creates a flame that propagates toward the droplet. Spherical, outwardly propagating premixed flames were observed for diesel droplet ignition in stoichiometric $CH_4/O_2/N_2$/Ar mixtures, whereas elongated premixed flames were observed in lean $CH_4/O_2/N_2$/Ar mixtures.

The experiments conducted to understand abnormal combustion caused by lubricant oil droplets provided a valuable dataset of ignition delay periods of various petroleum and ester-based lubricant oils at a wide range of thermodynamic and mixture conditions. In concert with the experiments, a combined analytical droplet evaporation model and computational combustion model were developed that simulate the evaporation, ignition, and combustion processes observed in the experiments. The ignition delay dataset was used to successfully develop and validate a surrogate chemical kinetic mechanism suitable for mimicking the ignition characteristics of different lubricant oils. The experiments also revealed the different thermodynamic and mixture conditions at which the lubricant oil droplets did not show ignition. At compressed pressure of 24

bar and varied compressed temperatures of 740 K < T_c < 900 K in $CH_4/O_2/N_2$/Ar mixture of ϕ = 0.6, two ester-based oils (EBO3 and EBO4) showed no ignition. The experiments and modeling indicate the minimum and maximum droplet sizes for which ignition will occur, the location and mode of ignition in the vicinity of the liquid droplet and the conditions under which the ignition event will transition into a propagating premixed flame. These experimental observations further enhance our understanding of lubricant oil combustion and provide qualitative information of engine operating conditions which can lower the abnormal combustion occurrence in natural gas engines.

The results of this study advance the fundamental understanding of dual fuel combustion and provide the practical knowledge to inform which lubricant oil types and droplet sizes promote or inhibit abnormal combustion in natural gas engines.

ACKNOWLEDGEMENTS

I remember vividly the time I decided to start my PhD in the field of combustion and advanced engines at Colorado State University in Dr. Anthony Marchese's group. This decision was one of the most important decisions of my life which has shaped me as the person I am today. I want to thank my advisor Dr. Anthony Marchese for taking a chance on me and allowing my curiosities to nurture and giving me the intellectual freedom to explore my research passion.

I would like to thank Dr. Bret Windom for his continuous support during my PhD specially with the fun ideas and supporting me to perform CFD simulations for the same. Thank you for giving me the research freedom and allowing the ideas to take shape. You have taught me the ideology of thinking beyond the scope and applying the learnings of one engineering topic to different engineering problems for getting solutions. Special thanks to my committee members Dr. Daniel Olsen and Dr. Karan Venayagamoorthy for their time and valuable feedback. I would also like to extent my thanks to Caterpillar Inc. for financially supporting my work and providing the engineering guidance. Thank you to David Montgomery, Jaswinder Singh, Glen Martin, Jon Anders for their continuous support. Your weekly push and feedbacks have helped significantly to make my PhD a success. Thank you to all my powerhouse colleagues, graduate students, undergraduate students Miguel Valles, Diego Bestel, Andrew Zdanowicz, Iris Kressler, Manav Sharma, Jeffrey Mohr, and Parneeth Lokini for their continuous support and friendship. You were my family away from home.

I would like to thank Isabelle Clement for her love and support all the way long and ensuring my well-being every single day. Thank you for spending time with me and being with me even

during the hardest of the days. My PhD journey would not have been this fun and successful without you being around.

Finally, I would like to thank my dad Bharat Bhoite and my mother Rajashree Bhoite who supported my decision of pursuing PhD and being patient with the time it took. Thank you both for giving me complete freedom to explore my life choices and supporting my every decision. You both have taught me important lessons and values in life which has helped me to be the person I am today. My PhD wouldn't be possible without your continuous love and support.

DEDICATION

I am dedicating this dissertation to my late grandfather Dayanand Maruti Pawar who always wanted to see me as a successful engineer building machines. He gave me the engineering vision during my early childhood and this vision has always motivated me to push myself to learn more and be a successful engineer.

TABLE OF CONTENTS

LIST OF TABLES

LIST OF FIGURES

CHAPTER 1: INTRODUCTION

Concerns over climate change and recent advancements in battery electric vehicles and hybridization of engines for on-road vehicle transportation have led to an increased effort for improvement of engine technologies to reduce emissions, particularly carbon dioxide, carbon monoxide, unburned hydrocarbon (UHC), particulate matter (PM), and nitric oxides (NOx) and achieve a nearly net zero emissions from engine operations. The U.S. Environmental Protection Agency (EPA) has also initiated regulations on greenhouse gas emissions (GHG) and fuel efficiency standards for light-duty vehicles in 2018 and heavy-duty vehicles by 2025 [2][3]. Internal combustion (IC) engines powered by natural gas has traditionally a greater advantage as compared to the diesel and gasoline fuels in terms of cost and emissions. Energy consumption from the transportation sector will remain at approximately 25% of the total U.S energy use through the year 2040 [1]. Most of this energy requirement will be accomplished using internal combustion engines.

Natural gas primarily comprises of methane which has a higher heating value and higher hydrogen-to-carbon ratio as compared to petroleum fuels. Thus, natural gas produces 25% less carbon dioxide as compared to gasoline and diesel fuels to produce the same amount of energy [4]. The use of natural gas also provides an economic incentive as natural gas is traditionally less expensive as compared to petroleum fuels. Due to these advantages, efforts are undertaken to convert commercial gasoline and diesel engines to natural gas engines. The Energy Information Administration (EIA) projection also shows an increase in the use of natural gas engines in the transportation sector, specifically in heavy-duty applications, such as trucks, buses, mining equipment, marine ships, construction equipment, and agricultural equipment [1]. Most of these

heavy-duty applications utilize diesel engines for high power density. Therefore, efforts are being made to convert these high-compression ratio diesel engines into natural gas engines.

1.1. Dual Phase Combustion in Natural Gas Engines

There are two potential ways one can envision the conversion of diesel engines into natural gas engines. The first method is using premixed natural gas/air mixtures in the engines and introducing a small pilot injection of diesel to serve as an ignition source of natural gas/air mixtures. This concept of using two fuels with desperate reactivities is termed dual fuel combustion. The second method is to convert the diesel compression ignition engines to spark-ignited natural gas engines. This method involves changing the infrastructure of diesel engine to introduce the spark plug assembly in the engine configuration. In spark-ignited engines, abnormal combustion is observed which is caused by lubricant oil droplets entering the combustion domain through the piston skirt. The abnormal combustion is a dual-phase (lubricant oil droplets and natural gas/air) phenomenon as well.

1.1.1. Fundamental Study of Dual Fuel Combustion

Diesel engines can be converted into dual-fuel diesel/natural gas engines by introducing natural gas in the intake manifold of the engine along with air and directly injecting a smaller amount of diesel fuel to serve as an ignition source. The fuel cost savings of dual-fuel engines increase with an increase in the substitution percentage of natural gas. However, since natural gas substitution schemes often utilize high compression ratio engines, the natural gas substitution percentage is often limited by engine knock and uncontrolled fast combustion [5][6]. Maximizing

the natural gas substitution percentage requires a greater understanding of the processes leading to uncontrolled combustion rates in dual-fuel engines.

The high expense of developing, fabricating, and testing new engines has motivated engine manufacturers to develop computational fluid dynamic (CFD) models for predicting engine behavior. These CFD models utilize various sub-models that simulate combustion chemistry, liquid fuel injection processes, gaseous intake and exhaust processes, heat transfer to cylinder walls, and in-cylinder fluid mechanics to understand the behavior of a full engine[5]. However, there is a need to maximize the accuracy of these engine CFD models by independently validating each sub-model under engine-like operating conditions (i.e., elevated temperature and pressure).

To accurately simulate the dual fuel combustion process in engines, chemical kinetic mechanisms must accurately capture both the ignition kinetics of the diesel/natural gas blend in the vicinity of the diesel spray and the premixed flame propagation of the natural gas flame that is initiated after ignition. Hockett and coworkers[6] developed a dual-fuel natural gas/diesel reduced chemical kinetic mechanism consisting of 141 species and 709 reactions by separately reducing a detailed n-heptane mechanism[7][8] and a detailed C_5 mechanism[9] using the direct relation graph method[10]. The reduced natural gas/diesel mechanism was tested and validated against ignition delay computations with the complete detailed chemical kinetic mechanisms and $CH_4/O_2/He$ experimental premixed laminar flame speeds at 40 and 60 atm. However, no experimental data were available to independently test the ability of the mechanism to accurately reproduce the ignition delay of the diesel/natural gas blend in the vicinity of the spray and the transition of that ignition event into a propagating flame.

A Rapid Compression Machine (RCM) is one such device that gives engine-like conditions in a controlled environment with negligible turbulence and allows to collect the crucial ignition

delay data for various diesel/natural gas blends for further validating the natural gas/diesel mechanism, hence addressing the gaps in the current understanding of these phenomena. In this work, we examine the RCM experimental system of ignition of a single liquid fuel droplet in a gaseous fuel/air mixture at elevated temperature and pressure in an RCM as a means to study the fundamental combustion processes of ignition and flame propagation in dual fuel engines and to generate experimental data that can be used to independently test and validate the dual fuel chemical kinetic mechanisms.

1.1.2. Abnormal Combustion Triggered by Lubricant Oil Droplets

In addition to dual-fuel engines, this work is also motivated by abnormal combustion observed in spark-ignited, highly boosted natural gas engines, which damages engine components due to rapid pressure rise in the engine cylinders, as shown in Figure 1.1. Most Original Engine Manufacturers (OEM) face a common issue of abnormal engine combustion occurring at low-speed, high intake pressure, and high-load engine conditions. A term called a Superknock or Low Speed Preignition (LSPI) or Load Induced Rapid Combustion (LIRC) is coined for such abnormal combustion. This phenomenon generally occurs a few times per thousand cycles and causes a rapid heat release and higher combustion pressures which can severely damage the engine components under continuous operation in this regime. Typical characteristic pressure traces for regular engine cycles and an LSPI cycle is as shown in Figure 1.1. The occurrence of abnormal combustion events limits the engine OEMs' ability to operate at higher load conditions and to further improve engine efficiency.

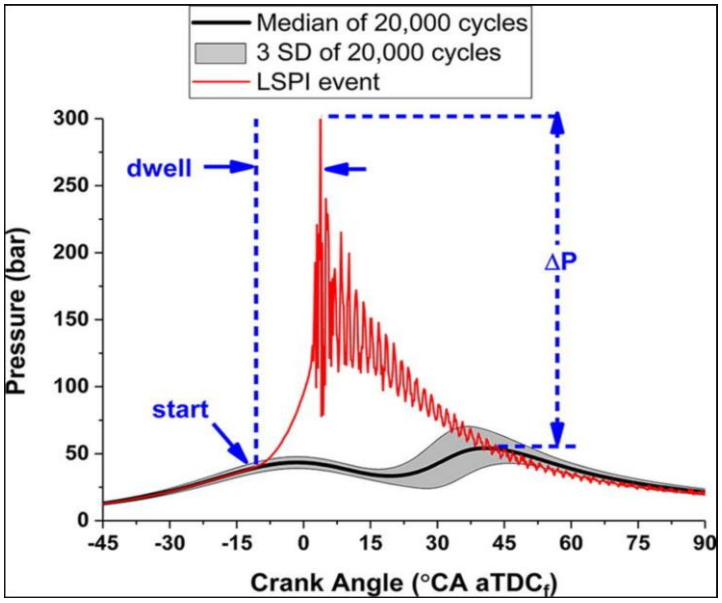

Figure 1.1. Engine Cycle with LSPI event (red) and regular engine cycle (black)

Many studies have been carried out by engine OEMs and research institutes around the world, but the exact reasons for the abnormal LSPI combustion in natural gas engines are still not well understood [12][13][14]. Figure 1.2 shows the root cause diagram highlighting the possible factors that alone or in a combination can result in causing the LSPI phenomenon in an IC engine.

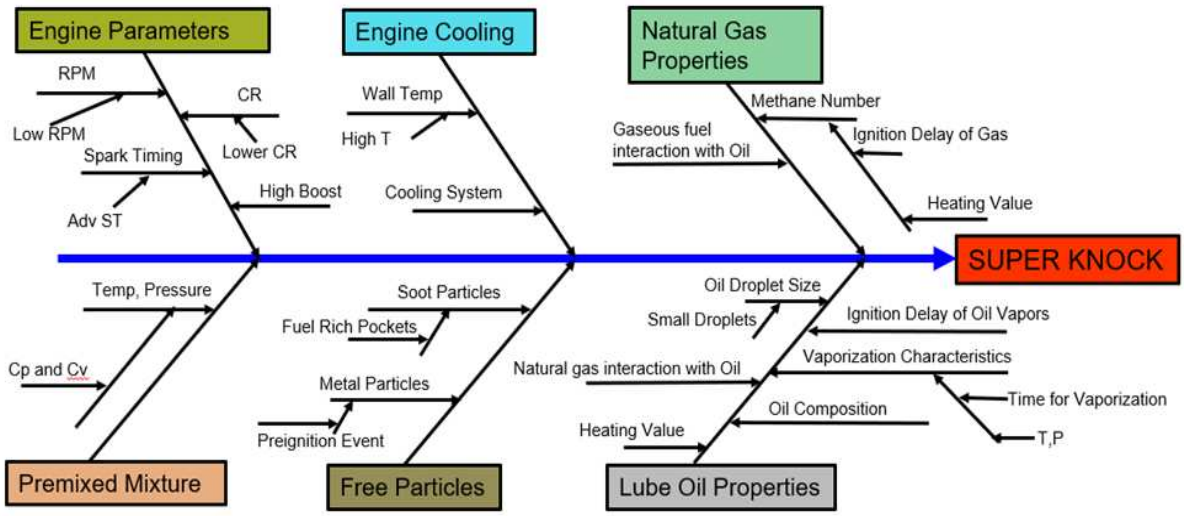

Figure 1.2. Engine Cause Diagram showing different factors influencing LSPI or super knock event

Inoue et al. [4] studied a highly boosted spark-ignited (SI) engine to show the effect of engine parameters and spark plug characteristics on possible causes of the LSPI combustion cycle. A 1.6L in-line four-cylinder SI engine with direct injection and turbocharging was used in this study with a compression ratio of 10.5 and an injection pressure of 120 bar. The results from this study are summarized in Table 1.1, which shows the effect of the engine parameters on the LSPI combustion event.

Table 1.1. Effect of Engine Parameters on the occurrence of LSPI phenomenon

Engine Parameters	**Effect on LSPI combustion**
Intake Pressure	Increases with increase in intake pressure
Lambda	Higher occurance with lean conditions
Intake Air Temperature	No significant influence was observed
Ignition Timing	LSPI event occurance increases with retart spark timing
Injection Timing	LSPI event occurance increases with retart injection timing
Intake Valve Opening	Higher occurrence with advance intake opening
Blow-by Oil	A higher blow-by oil increases the occurance of LSPI event

Inoue et al. [15] also carried out a study to see the influence of spark plug characteristics on the LSPI event. They found that the spark plug characteristic like heat range, ground electrode length, center electrode diameter, the orientation of ground electrode, and spark gap have minimal effect on the LSPI occurrence, and no significant correlation was observed between LSPI and other engine parameters. Palaveev et al. [11] studied the superknock or LSPI combustion in a turbocharged direct injection SI engine. This study combined a theoretical consideration with detailed experimental and numerical studies focusing on autoignition in the vicinity of the droplets as a cause of preignition. Figure 1.3 shows the logic tree used for studying the potential trigger mechanisms of preignition. They found out that the main cause of the LSPI event was the autoignition of lubricant oil droplets which entered the combustion chamber via piston rings and

ignited, causing a second flame in the combustion domain. A decrease in ignition delay of the lubricating oil droplets was observed with decreased droplet size and increased initial temperature of droplets. It was found that adding a proper additive in the lubricant oil can potentially suppress LSPI events. It was also observed that the increased amount of fuel near the cylinder wall strongly increases the occurrence of LSPI events. Articles published by other research institutes and industries also supported the claim made by Palaveev [16][17].

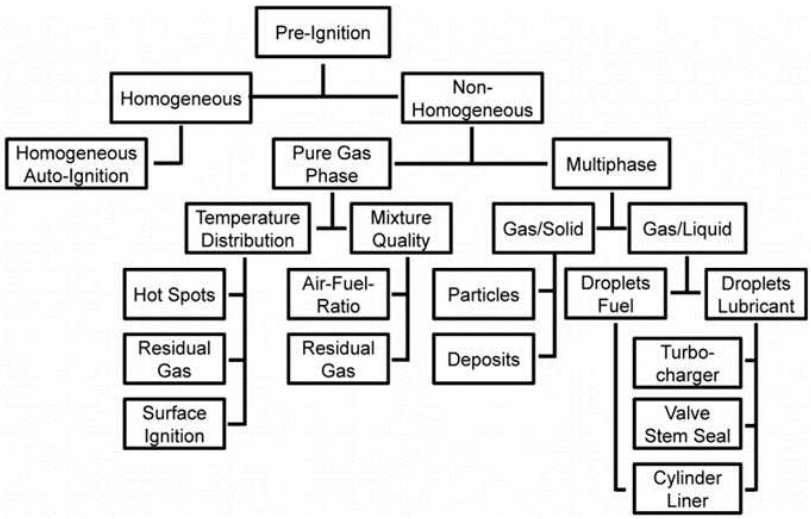

Figure 1.3. Logic Tree for studying potential trigger mechanisms of Preignition [11]

Willand et al. [18] conducted experimental and numerical investigations and concluded that hot spots, deposits, lubricant droplets, residual gas, and autoignition of the fuel-air mixture are potential sources of preignition. The study also pointed out the influence of intake valve opening on the occurrence of high-pressure waves. Zahdeh et al. [19] conducted an experimental investigation where a correlation was obtained between the lubricant film impingement on cylinder walls and the observed preignition rate. A strong interrelation was observed between the preignition event and super knock (LSPI) event in the investigation study by Bradley et al. [20].

There was also an experimental study conducted by Gunther et al. [12] to see the probability of the preignition event concerning the enthalpy of the mixture.

In addition to the above studies, which focus on engine parameters, there are several studies carried out by other researchers showing the importance of studying the lubricant oil composition on the occurrence of the LSPI phenomenon. Park et al. [21] show the effect of molybdenum, zinc, calcium, magnesium, phosphorus, and boron concentration on the probability of occurrence of an LSPI event.

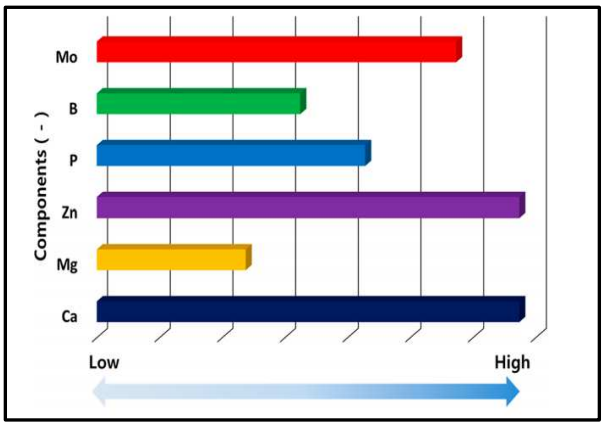

Figure 1.4. Effects of Lubricant components on preignition [14]

Based on the study, calcium, molybdenum, and zinc were some of the components that strongly influence the occurrence of LSPI events. Zahdeh et al. [14] and Dahnz et al. [22] also related the preignition occurrence to the floating lubricant particles, where the experimental and numerical approach was taken to understand the parameters to improve or even eliminate the LIRC combustion events. There are other articles [11][23][24][25][26][27][28][29] that support the research findings of Park et al. indicating the lubricating oil additive as a potential cause of LSPI event. It was also observed that calcium in lubricant oil increases the tendency of LSPI events, whereas the components with phosphate and boron have less tendency to trigger LSPI events.

With the understanding of the possible causes for LSPI event, the exact mechanism resulting in this event is still unclear and hence requires a more detailed analysis in a controlled environment mimicking engine-like condition. If oil droplet ignition triggers combustion in a premixed fuel/air mixture, there is a need to understand the local thermodynamic and mixture conditions under which such an event occurs. Due to an engine's stratification in temperature and fuel distribution, it is challenging to find the local conditions under which such an event occurs.

Many researchers have also utilized advanced computational fluid dynamics (CFD) to predict the phenomenon of LSPI events. Zhu et al. [30] conducted a computational study to develop counter measures to mitigate the increased severity of the LSPI events and highlighted the capability of advanced CFD combustion technology to develop highly optimized solutions for higher efficiency and higher power density natural gas engines. In his study, the lubricant oil was modeled as a heavy hydrocarbon surrogate. Some key results from the study include having a center-rich fueling strategy that lowers the LSPI events by reducing the fuel oil interaction near the liner walls. Sotiropoulou et al. [31] also used advanced CFD combustion technologies to develop a sophisticated lean burn pre-combustion chamber to minimize the occurrence of the LSPI phenomenon. In this study, the lubricating oil droplet was modeled as a high-order alkane surrogate, similar to the approach taken by Zhu et al. [30].

Carrying out CFD studies provides an additional understanding of the different possible scenarios in which different parameters can be investigated for in-depth study on the problem under consideration. However, with CFD studies, there is always a caution associated with whether the physics used in the study is relevant to the problem under consideration. In understanding the LSPI phenomenon, one of the problems associated with CFD models is the accuracy of the chemical kinetic mechanism of the lubricating oil under consideration. Many researchers in the

past have used a surrogate fuel to represent the ignition properties of lubricating oil. This assumption is valid only for a few thermodynamic conditions, and as the thermodynamic parameters are swept over a wide range of conditions, the properties of the surrogate fuel no longer represent the properties of the lubricating oil. To develop better CFD models, it is crucial to understand the lubricating oil properties like evaporation and combustion characteristics, and the composition of lubricating oil to develop better chemical kinetic mechanisms representing an accurate behavior of the lubricating oil under various engine-like conditions.

Similar to the solution for the dual fuel challenges discussed in Section 1.1.1, an RCM can be used to study the evaporation and combustion characteristics of lubrication oils and provide valuable ignition delay data that can be used for developing and validating the chemical kinetic mechanism for lubricating oils. The developed and validated mechanism can then be used for carrying out multi-dimensional CFD studies on actual engines to understand the LSPI phenomenon and develop strategies for preventing such events. Sullivan et al. [32], in their master thesis, carried out a study of lubricating oil ignition in an RCM under sporadic pre-ignition conditions for various commercial oils. These oils were exposed to high-temperature pulses resulting in sporadic evaporation of the oil, producing oil vapors that mix with the surrounding fuel/air mixture resulting in flame propagation. This study gave a relative understanding of the chemical ignition delay of different lubricant oils, but the evaporation characteristics were not quantified as the lubricant oils were sporadically heated to a very high temperature which vaporized different oils instantly. Hirose et al. [35], in their study of understanding the preignition behavior of 2-stroke gas engines, carried out some experiments in a single-piston RCM. In this study, the oil was spilled at the bottom of the combustion chamber, which moved in the other regions of the combustion chamber by strong turbulence coming from the piston motion and ignited in the hot combustion domain.

These experiments had limitations as the droplets were experiencing high turbulence, which could potentially affect the development of the chemical kinetic mechanism. Ohtomo et al. [33] studied the mechanism of lubricant oil droplets initiating preignition in highly boosted downsized gasoline engines. In this study, the lubricant oils were tested in an RCM integrated with a piezoelectric droplet generator. Various sizes of lubricant oil droplets were generated and tested to study the ignition characteristics of various sizes of lubricant oil droplets and to observe the potential ignition in the surrounding gasoline/air mixture. This study gave a fundamental understanding of droplet evaporation and combustion phenomenon. The ignition delay period of lubricant oil droplets decreases with a decrease in droplet diameter and an increase in droplet temperature. It was also found that the lubricant oil temperature in the engine before the compression stroke should be around 300^{o}C to trigger the abnormal combustion.

Fei et al. [34] also conducted a similar study investigating single lubricating oil droplets in a premixed combustible mixture at engine-relevant conditions. The study supported the work carried out by Ohtomo et al.[33] with a similar trend in results. Yi et al. [36] also conducted a numerical and experimental study of evaporation and autoignition characteristics of lubricating oil droplets in natural gas in-cylinder engine conditions. A constant volume chamber was used for the experiments where the droplet was suspended in the hot environment of the chamber, and a high-speed camera was used to observe the droplet and study its evaporation and ignition characteristics. Yi et al. also show similar trends observed in the investigation carried out by other researchers [33][34]. Even with many efforts to understand the LSPI phenomenon, the exact reasons are still not well understood and require more work to further understand the LSPI phenomenon and develop validated chemical kinetic mechanism for CFD models, specifically for natural gas engines.

The proposed work focuses on an experimental and computational study to quantify the LSPI events in a controlled environment by injecting isolated lubricant oil droplets in natural gas/air mixtures. Studying the lubricant oil evaporation/ignition characteristics with negligible turbulence helps in isolating the chemical kinetics from other complex processes of engine operations, thus allowing to perform fundamental studies to understand the LSPI occurrence in natural gas engines.

1.2. Droplet Injection in Rapid Compression Machine

Even though Section 1.1.1 and Section 1.1.2 are two distinct challenges, both these studies focus on similar dual-phase flow phenomena (i.e., diesel/natural gas or lubricant oil/natural gas). To focus on the fundamentals of chemical kinetics and avoid the complexity associated with diesel spray in natural gas engines, the study of droplets at high temperature and pressure conditions provides geometric simplicity and an ideal platform for understanding the interaction of two fuels of disparate reactivities. Furthermore, for the LSPI phenomenon, lubricant oils leak in the natural gas engine chamber as isolated droplets. Hence for both these studies, an RCM integrated with a droplet generator can be used to perform experiments at engine-relevant conditions, which can further aid the development and validation of chemical kinetics and the CFD models.

Droplet ignition/combustion in a premixed fuel-air environment under engine-like conditions (e.g., elevated temperature and pressure) represents an ideal environment to study dual fuel ignition processes and investigate the abnormal combustion phenomenon triggered by lubricant oil droplets. Several recent droplet combustion studies have been conducted using RCMs or shock tubes to produce elevated temperature and pressure. Kim et al. [37][38][39][40] used a single-piston RCM geometry with large diameter droplets (400–600 μm) suspended using a K-type, fine wire thermocouple (50 μm wires, 100 μm bead diameter) in the combustion chamber to study

single and bi-component droplet ignition to investigate the effects of fuel volatility and reactivity. Gould et al. [41] studied the vaporization and combustion of suspended heptane droplets in methane/oxidizer/inert mixtures in an opposed piston RCM. Ohtomo et al. [33] injected and suspended lubricant oil droplets of 100 μm to 400 μm in air and gasoline-air mixtures in a single piston Rapid Compression and Expansion Machine (RCEM) to investigate the conditions under which a single oil droplet initiates the combustion of gaseous fuel-air mixtures. Niegemann et al. [42] established a strategy of using a shock tube in combination with an injection system to study the influence of the lubricant oil droplets on the ignition of fuel/air mixtures. Niegemann and coworkers concluded that the amount and composition of the injected liquid fuel are important factors determining the extent of the interference with the ongoing autoignition of the premixed fuel/air gas.

Combustion of single droplets as a means to elucidate the underlying physics of sprays has been studied for nearly 70 years, with the first studies investigating droplet combustion occurring in the 1950s [43]. Despite the long history of research on the combustion of liquid fuel droplets, relatively little research has been done to date on the combustion of a high reactive liquid hydrocarbon droplet in less reactive gaseous fuel/oxidizer mixture at engine-relevant temperatures and pressures [44][45]. As described herein, a new method has been developed to inject single isolated liquid hydrocarbon droplets into premixed methane/oxidizer/inert mixtures at elevated temperatures and pressures using an opposed-piston rapid compression machine in combination with a newly developed piezoelectric droplet injection system that is capable of injecting single liquid hydrocarbon droplets along the stagnation plane of the combustion chamber.

The work presented shows the ability of the RCM integrated with a droplet generator to inject single liquid hydrocarbon droplets of 40 to 500 μm along the stagnation plane of the combustion

chamber with various fuel-oxidizer stoichiometry subject to rapid temperature and pressure increase. This dissertation also includes the details about the design, fabrication, and operating characteristics of the droplet generator, along with the details of integration and control of the droplet generator in the RCM. The experimental technique described herein was used to optically capture the ignition event in the vicinity of a spherical hydrocarbon droplet and subsequent bifurcation into an outwardly propagating, premixed gaseous fuel/air flame. Results show the RCM system integrated with the droplet generator to perform fundamental research on dual fuel combustion and lubricant oil-triggered abnormal combustion phenomena. Experiments were conducted with a certification diesel and four different lubricant oils at various droplet diameters ($50\ \mu m < d_o < 500\ \mu m$), various methane/air equivalence ratios ($0 < \phi < 1.2$) and various compressed temperatures ($700\ K < T_c < 1000\ K$). This work allows for an enhanced understanding of the dual-phase combustion phenomenon, which will aid the engine OEMs in achieving high performance in dual-fuel engines and minimize the occurrence of abnormal combustion phenomena observed in highly boosted spark-ignited natural gas engines.

CHAPTER 2: EXPERIMENTAL SETUP

2.1. Droplet Generator Design

The first design iteration of the droplet generator utilized a stack actuator fixed at the head of the droplet generator using an adhesive, as shown in Figure 2.1. This piezoelectric stack was actuated using the square voltage waves, which deflect a plunger connected on top of the piezoelectric stack. The motion of the plunger results in a pressure wave in the fluid, which was introduced into the droplet generator using an external pump. The original idea was to use the pressure wave in the liquid fuel and pass it through the nozzle, which would result in the formation of the droplet. The nozzle was placed in location using a press-fit washer. Spring was also introduced between the nozzle washer and the plunger to support the plunger's continuously transitional motion and help reduce the loading on the piezoelectric stack.

The droplet maker prototype assembled and tested was a piston design (a plunger) driven by a piezoelectric stack actuator which can be seen in Figure 2.1. The main components of the design were the piezoelectric stack, a plunger made of stainless steel, a Swagelok stainless steel housing, and variable diameter nozzles ranging from 50 µm to 500 µm. The piezoelectric stack actuator is a purely linear actuator with microsecond response times and was able to provide high forces capable of lifting the plunger to generate pressure waves in the fluid and push the fluid through the nozzle to create droplets. The actuator chosen from the piezo drive provides a maximum of 20.1 µm displacement at a maximum voltage of 150V. This voltage was controlled with Thorlabs Piezo electric driver and a pulse generator to create high-impulse pulses transferred to the piston. The piezoelectric actuator was bonded to a ¼" NPT Swagelok end cap using Hysol epoxy and connected directly to the ¼" NPT T-joint. A three-stage piston is contained within the T joint with

reducing diameters shown in Figure 2.1. The piston is fitted with a 2-008 size Viton O-ring. The tiered design and increased length from previous iterations increase the force of pressure the piston can apply to the oil. The connector used to join the nozzle element with the reducing bushing is a ¼" Swagelok NPT fitting, as shown in Figure 2.1. The nozzle element consists of a Swagelok ¼" NPT to ¼" pipe thread adapter that contains the press-fit Teflon seal and the nozzle.

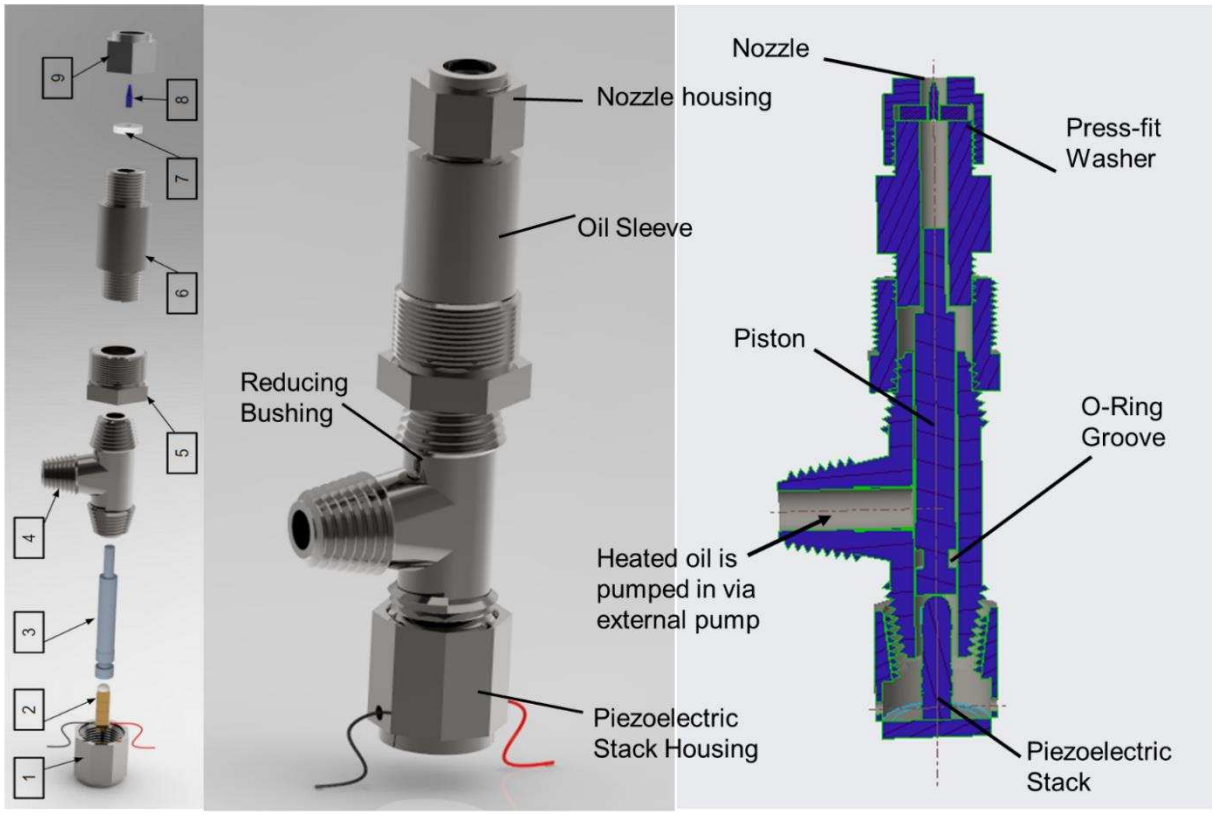

Figure 2.1. (A) Exploded view of the model of Piezoelectric Stack Droplet Generator, (B) Solid model of the Droplet Generator, and (C) Cross-sectional view of Droplet Generator

A change was introduced in the design where the droplet generator body was shortened, which required some redesigning of the driver plunger. This design change made the droplet generator more efficient in terms of fewer parts and small space design suitable for mounting on the RCM chamber and not interfering with the schlieren imaging lenses on the outside. The plunger design was changed from a simple cylinder that was about half an inch in length with an O-ring groove

in the middle into what is referred to as the wedding cake design. The wedding cake design is a cylinder with three different diameter steps going from the most significant section near the stack actuator and the thinnest section at the nozzle. This redesign limits the volume of fluid in the oil sleeve and gives additional fluid push much closer to the nozzle.

Table 2.1. Bill of Materials for the piezoelectric stack droplet generator with part number provided for locating the parts in the assembly provided in Figure 2.1

Part Number	Description	Quantity
1	1/4"Swagelok NPT end cap	1
2	Piezoelectric stack	1
3	Piston	1
4	1/4"Swagelok NPT T-Joint	1
5	1/2" to 1/4" reducing bushing	1
6	Sapphire Nozzle	1
7	Oil Sleeve	1
8	1/4"Teflon Washer	1
9	Swagelok 1/4" pipe nut	1

The first iteration of the droplet generator design was then tested and faced some issues in operation. The design limitations are as follows:

1. Many moving parts in the design resulted in increased friction, resulting in the less efficient transfer of fluid motion.
2. The gap between walls was wide and caused the fluid to stay in the big gap rather than get compressed by the plunger.
3. Preloading the piezoelectric stack was potentially impossible as it requires a high-stiffness spring, which generally comes with a higher thickness and cannot fit in the small gap.
4. Continuous supply for the fluid was not possible using the pump as it dripped the fluid through the nozzle.

5. O-ring in the moving component resulted in additional friction, which dampened the parts' motion, creating more problems for droplet formation.
6. High-stress point was present at the plunger head and piezo stack contact point, which can damage the components over continuous use.
7. There were significant gaps in the assembly where the fluid could get collected, resulting in dampening the pressure wave and the pressure in the fluid was unable to reach the nozzle for creating droplets.
8. The piezoelectric stack, though, supplies a high force but was limited to only 20 µm in displacement and hence was unable to displace enough fluid to create the droplets.

With all the above limitations, the droplet generator's first iteration was unable to generate droplets as required. However, the design taught the improvements required for the subsequent iterations. With these learnings, a new design was proposed to overcome the limitations observed in the first design. A pancake design of a droplet generator, as shown in Figure 2.2, was proposed, which utilizes a disc shape piezoelectric element instead of a stack design. This design had fewer moving parts and hence resulted in fewer frictional losses. Also, since a disc shape piezoelectric element has a more extensive surface area, the force exerted by the element is distributed to a larger volume of fluid which increases the strength of the pressure fluctuation in the fluid and can help in a consistent and robust droplet formation through the nozzle. The disc shape of a piezo electric element was selected from TDK Corporation limited, namely the Piezo Haptic Actuators – Powerhap. This piezoelectric disc's general features include a larger displacement, high acceleration, large force, and fast response time when subjected to a voltage square wave. The operational voltage for the piezoelectric element is -20V to 120V with operating temperatures of -40C to 85C.

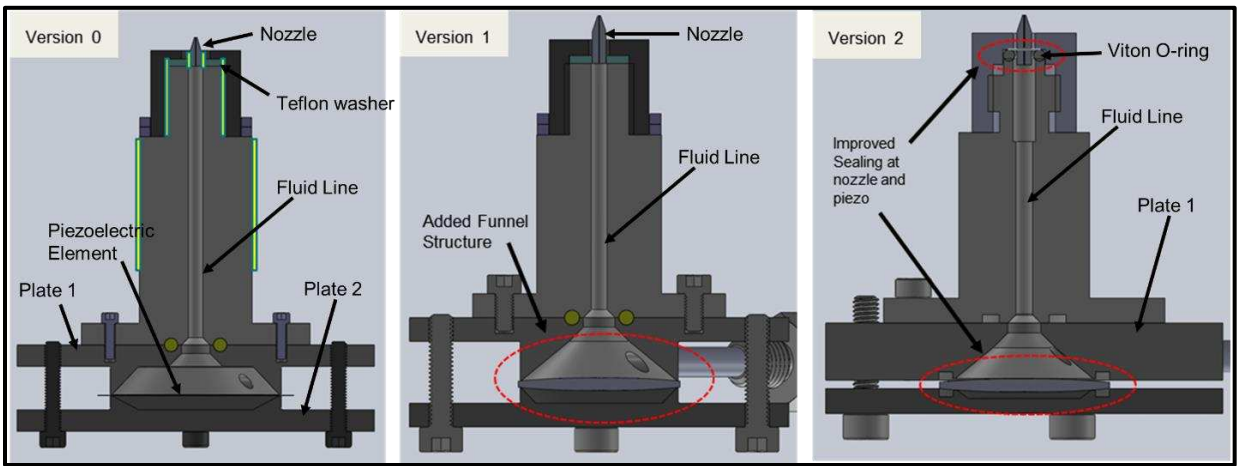

Figure 2.2. Version 0,1,2 of the Pancake Droplet Generator Design using piezoelectric disc highlighting the changes introduced in each iteration using the red marker.

As shown in Figure 2.2, the first iteration of the droplet generator design involved using a knife edge and bolts to hold the piezoelectric disc in position. A long sleeve was provided along with the threads to ensure its integration into the RCM combustion chamber. However, with this iteration, a quick change was introduced in the design, and a funnel structure was introduced to ensure no losses in the transfer of pressure force from piezoelectric disc deflection to the fluid. Droplet generator Version 1 worked very well with consistent and robust droplet formation but had a few limitations, which are as follows:

1. Knife edge to hold the piezoelectric element damaged the piezoelectric element and required its constant replacement.
2. The fluid leakage was observed around the knife edge holding the piezoelectric element and at the tip of the nozzle, which was held together using the Teflon washer.

These limitations were overcome in Version 2 of the droplet generator design. In Version 2, the knife edge design was replaced by a soft Viton O-ring to hold the piezoelectric element. Using this design, the structural integrity of the piezoelectric element was achieved, and the lifetime of

the piezoelectric element was improved. Using the Viton O-ring design also helped solve the problems of fluid leakage around the piezoelectric element. A Viton O ring was also used in compression near the nozzle. This O-ring holds the nozzle at the tip of the droplet generator and provides sealing for the fluid to stay within the body of the droplet generator, and no leaks were observed in this design.

The testing of Version 2 of the droplet generator was first carried out using heptane and diesel as the base fuel. This version worked very well with heptane and diesel fuel with the consistent formation of droplets. The droplet sizes were also controllable using the supplied amplitude and pulse width of the square wave to the piezoelectric element and by using different size nozzles. Although Version 2 functioned as desired, there was a limitation associated with this design. This design iteration could not create droplets using highly viscous lubricant oils.

To overcome this limitation, a modification to design Version 2 was proposed, including ports for cartridge heaters. The idea was to heat up the lubricant oil in the droplet generator to reduce its viscosity and make the lubricant oil flow readily within the droplet generator body, thus ensuring a good droplet formation. Version 3 of the droplet generator design with cartridge heaters installed is shown in Figure 2.3. This design iteration worked well in handling the high-viscosity lubricant oils and successfully demonstrated the droplet formation using high-viscosity oil. With the capability of handling the highly viscous oils and ensuring good sealing of the liquid fuel within the droplet generator, the next step involved integrating the droplet generator into the RCM chamber.

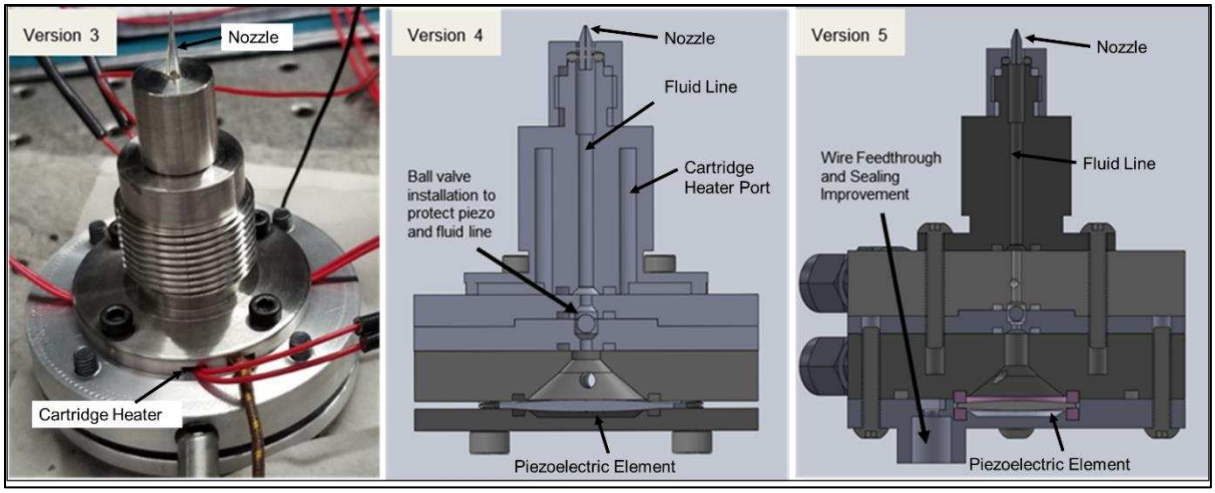

Figure 2.3. Version 3,4 and 5 of the Pancake Droplet Generator Design using a Piezoelectric Disc highlighting the changes introduced in each iteration using the red marker.

Version 3 droplet generator design had one limitation regarding its integration with the RCM chamber. The design could not seal the liquid fuel under high pressure and temperature conditions under RCM compression stroke. This limitation can result in breaking the piezoelectric element, and the overhead tank can explode if the chamber pressure is exposed to the overhead tank. So, to ensure the safe operation of injecting droplets in the RCM chamber and avoiding high-pressure leaks, a ball valve mechanism was designed and introduced in Version 4 of the droplet generator, as shown in Figure 2.3. The introduction of the ball valve ensures that the high-pressure experience in the combustion chamber during RCM compression does not travel in the droplet generator's fluid line and helps protect the fluid line connected to the overhead tank. Finally, in Version 5, wire feedthrough was provided to ensure sealing from pressure leaks through an electrical connection to the piezoelectric element to ensure a robust operation of the droplet generator, as shown in Figure 2.3.

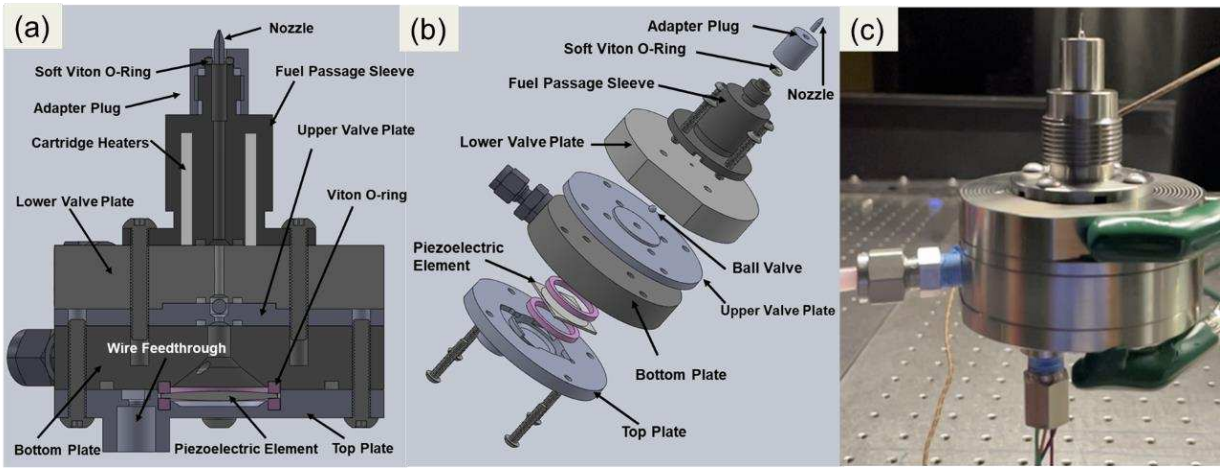

Figure 2.4. (a) Solid model of the piezoelectric droplet generator, (b) exploded view of a solid model of the droplet generator, and (c) a photograph of the fabricated droplet generator

Figure 2.4 shows the droplet generator's final design, which accounts for all the specifications required to perform single droplet ignition/evaporation experiments in the RCM. In this final design, an additional outer Viton O ring is provided near the piezoelectric element to ensure double sealing of the liquid fuel present within the droplet generator. While numerous piezoelectric droplet generators have been described in the literature [46][47], the droplet generator as developed and described herein has multiple novel characteristics, including the ability to preheat highly viscous liquid droplets and to prevent backflow into the device after compression and ignition of the gaseous fuel/air mixture into which the droplets are injected. The droplet generator consists of a piezoelectric element, a fuel reservoir, a fuel passage with a check valve, cartridge heaters, and a nozzle. The main body of the droplet generator is fabricated in multiple sections from stainless steel. This design ensures effective liquid hydrocarbon sealing within the droplet generator's body under elevated pressure conditions. Viton O-rings are installed between each device section to ensure effective sealing. A hermetically sealed wire connector by PAVE technologies model 2411 – 2 is provided at the top plate of the droplet generator, which provides

electrical connections to the piezoelectric element. The droplet nozzle is held using a soft Viton O-ring in an adapter plug.

A ball valve assembly was designed and placed upstream of the bottom plate holding the piezoelectric element and downstream of the fuel passage sleeve. NPH cartridge heaters of 30 W, 0.3175 cm diameter, and 1.905 cm long are integrated into the fuel passage sleeve of the droplet generator to heat the liquid fuel to elevated temperatures. A thermocouple port is provided near the cartridge heaters to cycle the power supplied to the cartridge heaters using a PID controller to maintain a constant liquid fuel temperature as it exits the nozzle.

A TDK PowerHap^{TM} haptic actuator was used as the piezoelectric element. The operational range of the piezoelectric element is from -20 V to 120 V, which produces elongation in the element ranging from -55 μm to 220 μm depending upon the applied square wave voltage. The elongation results in a pressure wave in the fluid that travels to the nozzle and produces a droplet. The applied square wave voltage and duration depend on the liquid fuel viscosity. Lower viscosity fuels such as n-heptane and diesel require a square wave ranging from 30 V to 50 V with a pulse width ranging from 0.7 to 1 ms to obtain the optimal droplet trajectory, which for the experiments described herein consists of a vertically launched droplet with an apex at 2.2 cm above the nozzle and a total time of flight of 180 ms in the combustion chamber.

Conversely, highly viscous lubricant oils require 100 V with a pulse width range of 1 to 3 ms. The droplet generator design can shoot low viscosity fuel droplets to an apex of approximately 200 cm above the nozzle in benchtop configuration in atmospheric air at maximum voltage. Droplet size control is achieved using quartz nozzles of various diameters ranging from 40 μm to 500 μm, designed at Colorado State University (CSU) and fabricated at Argonne National Laboratory.

The development of this novel droplet generator system was required to overcome unique challenges regarding the precise injection of droplets into high-pressure/temperature chemically reacting environments. Specifically, the novel aspects of the droplet generator include:

1. The droplet generator configuration includes an integrated check valve assembly that prevents the back flow of the liquid fuel into the droplet generator under high-pressure conditions in the test (combustion) chamber during RCM compression and combustion events. It also ensures that the liquid fuel reservoir and piezoelectric element are not exposed to high-pressure conditions, a critical safety requirement.
2. This new design can inject lubricant oils (and other high viscous fluids) having viscosities up to ~ 350 cSt.
3. The droplet generator includes an integrated and controlled heating system to preheat liquid droplets.
4. As integrated with the RCM, the piezoelectric droplet generator can precisely control the injection timing relative to the RCM compression process.

2.2. Integration of Droplet Generator with RCM apparatus

An opposed-piston RCM, as shown in Figure 2.5, is used to produce elevated pressure and temperature conditions using a combination of pneumatic and hydraulic systems. The RCM was manufactured by Marine Technology, LTD of Galway, Ireland [48][49]. As configured for the experiments described herein, the RCM has a compression ratio of 11.6 and produces compressed pressures ranging from 16 bar – 40 bar depending on the inert gases used (e.g., N2 and Ar mixtures). The RCM combustion chamber is cylindrical with an uncompressed stroke of 355.6 mm, compressed piston separation of 20 mm, and a bore of 38.1 mm. Traditionally, RCM

apparatuses such as that employed in this work are used to perform autoignition studies of fuels without any external ignition sources. In RCM autoignition experiments, fuel/oxidizer conditions are selected such that autoignition occurs within 1 to 200 ms after the compression stroke with the ignition delay period obtained from high-speed pressure data. The measured ignition delay periods are then compared against a chemically reacting flow model as a means to test detailed or reduced chemical kinetic mechanisms.

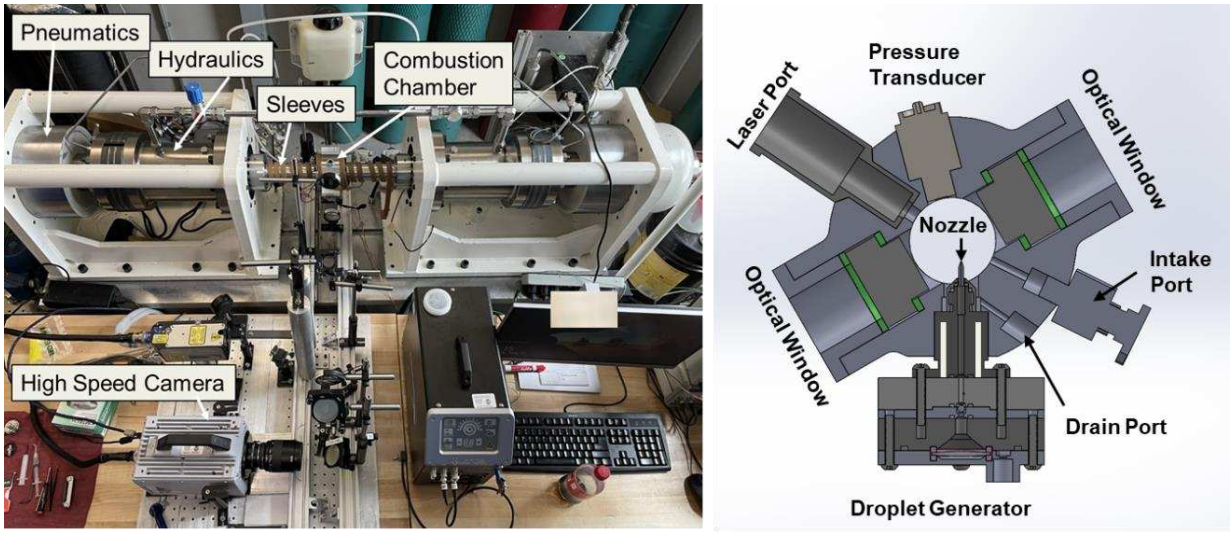

Figure 2.5. (a) Dual opposed piston rapid compression machine and (b) cross-section of a solid model of the rapid compression machine combustion chamber with integrated droplet generator.

For this research described herein, as shown in Figure 2.5(b), the RCM combustion chamber was integrated with the droplet generator described above to study the ignition characteristics of the liquid fuel in a gaseous fuel/oxidizer/inert mixture. To ensure the sealing of the gaseous fuel/oxidizer/inert mixture within the combustion chamber, a copper crush washer was used between the combustion chamber and the droplet generator. A liquid drain port was provided in the combustion chamber, as shown in Figure 2.5(b), to ensure the emptying of the residual liquid fuel between each individual experiment to minimize the formation and ignition of a liquid pool

near the chamber walls. The optical windows provided in the chamber are 1.05 inches in diameter, allowing visualization of a large volume of the combustion chamber domain. Nylon washers are used between the sapphire windows to ensure the sealing of the combustion gases.

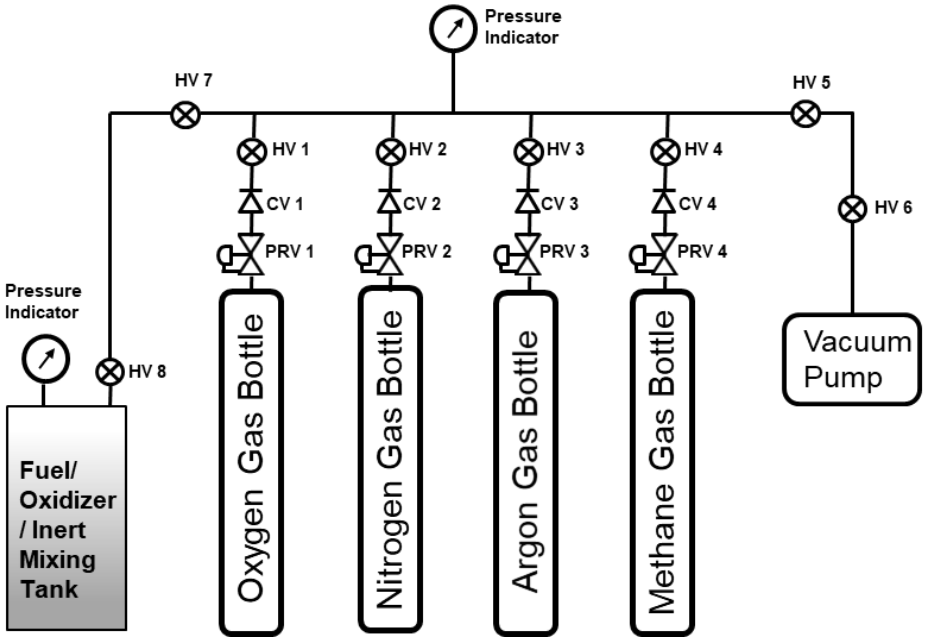

Figure 2.6. Schematic diagram of gaseous $CH_4/O_2/N_2/Ar$ mixing system for the rapid compression machine, including all pressure regulator valves (PRV), manually operated valves (HV), and check valves (CV).

A fuel/oxidizer/inert mixing tank was used for precisely blending the gaseous reactants, as shown schematically in Figure 2.6. The reactant mixtures were created using the partial pressure technique adapted from ASTM Standard D4051 – 10. The partial pressures of methane (CH_4), oxygen (O_2), and inert gases comprising of nitrogen (N_2) and argon (Ar) were measured using an MKS model 722B53TCD2FA pressure transducer. A more detailed procedure used to blend the gaseous reactants in the mixing tank can be found in Mohr et al. [50]. Blending the gaseous reactants in the mixing tank is necessary to ensure the creation of a homogenous mixture as compared to introducing the reactants directly into the RCM combustion chamber.

Furthermore, the mixing tank is also temperature controlled, allowing to set the temperature of the reactant mixture to the initial temperature required for the experiments. The total reactant mass in the mixing tank is sufficient to conduct 10 to 15 experimental cases. In this study, different reactant blends were created to vary the equivalence ratio over a range of $0 < \phi < 1.2$. The oxidizer/inert mixture used was 21 % O_2 and 79% inert for all cases. The specific concentrations of N_2 and Ar in the inert component of the mixtures were varied as a means to vary the specific heat ratio of the gaseous mixture to obtain a wide range of compressed temperatures ranging from $740\ K < T_c < 1000\ K$.

2.3. High Pressure Droplet Injection and Timing the Droplet Injection with RCM Pistons

Droplet generators are often limited only to atmospheric pressure operations [46][47]. Injecting a droplet into the RCM combustion chamber at high pressure (P1) conditions requires an experimental configuration that provides a pressure balance between the liquid fuel reservoir and the gases in the combustion chamber, as shown in Figure 2.7. For each experiment, the liquid fuel reservoir is maintained at a given height to create the static pressure required to prime the tip of the nozzle with fuel. To maintain consistent droplet formation, a thorough priming process is performed to remove air bubbles from the liquid fuel lines and within the droplet generator. For creating droplets at higher pressure conditions, a pressure balance is achieved by simultaneously introducing the gaseous fuel/oxidizer/inert mixture from the mixing tank to the combustion chamber and the back side of the liquid fuel reservoir, as shown in Figure 2.7. After filling the gaseous fuel/oxidizer/inert mixture in the combustion chamber and establishing the pressure balance, hand valve 1 and hand valve 2 are closed for both the combustion chamber and the liquid fuel reservoir. The piezoelectric element is then triggered with an external pulse generator, which

introduces a pressure wave that pushes the liquid fuel upward, opens the ball valve within the droplet generator, and expels the fuel through the nozzle to produce a single liquid fuel droplet with an upward vertical trajectory.

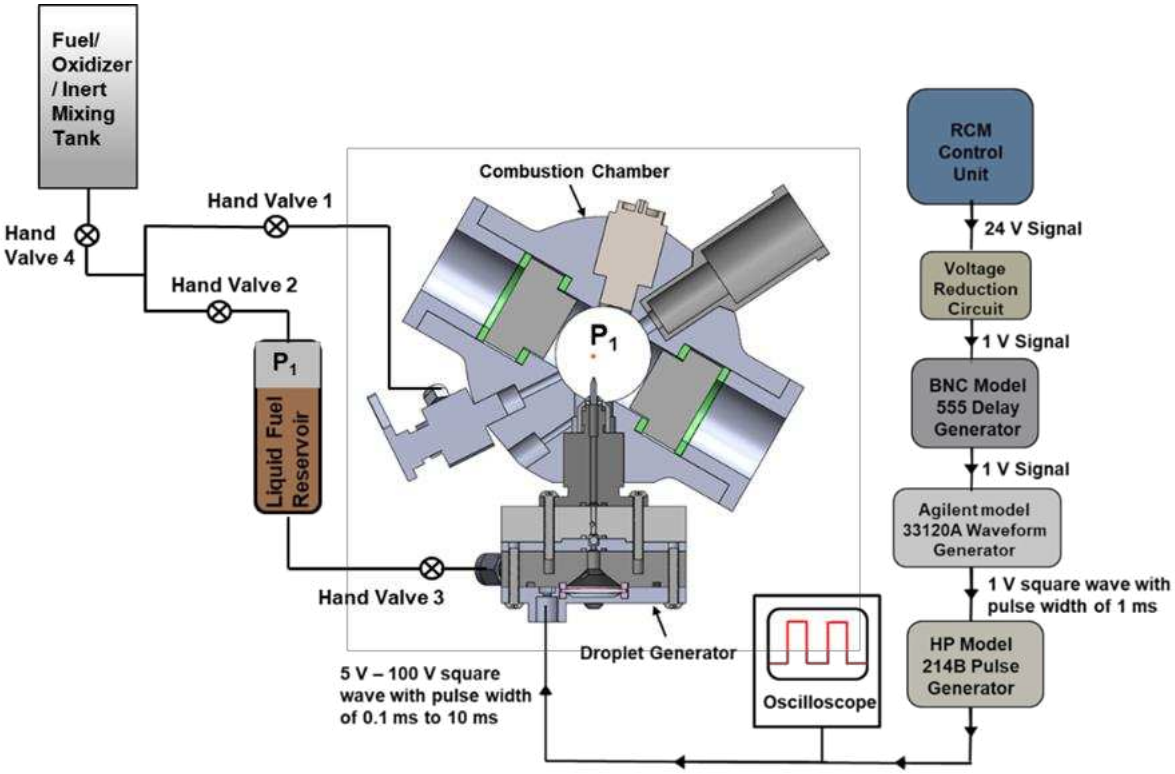

Figure 2.7. Rapid compression machine combustion chamber and droplet generator configuration for high pressure droplet injection and RCM electrical connection configuration for droplet injection timing control.

Figure 2.7 also shows the schematic diagram of the electronic systems used for triggering the piezoelectric element and timing the droplet injection with RCM piston displacement. To ensure the droplets injected in the combustion chamber experience the high temperature and pressure conditions for sufficient time, the trigger timing of the piezoelectric element is delayed by 100 ms (just before the piston displacement) using BNC model 555 delay generator, which receives an input signal from the RCM control unit. A voltage reduction circuit is used to keep the supplied voltage within the nominal operating voltage of the delay generator. Once the delay generator is

triggered, a signal is sent to the Agilent model 33120A waveform generator that generates a 1 V square wave with a pulse width of 1 ms. This square wave is then given to the HP Model 214B pulse generator, which produces a square wave of 5 to 100 V with a pulse width ranging from 0.1 to 10 ms. Depending on the liquid fuel under consideration, a different set of voltage amplitude and pulse width settings are required to produce single droplets. A strong dependency was observed between the liquid fuel viscosity and the signal required for producing droplets. For creating droplets with heavy viscous lubricant oils, cartridge heaters provided in the fuel passage sleeve were used to heat the lubricant oil to reduce the oil viscosity, which allowed the lubricant oil to flow readily within the droplet generator, assisting the droplet formation process. Heating the lubricant oil within the fuel passage sleeve provides a robust and safe method for handling the heated lubricant oils as hot temperatures are confined within the droplet generator body.

Figure 2.8 is a plot showing representative data acquisition and control signals obtained during an RCM experiment, including two piston displacement profiles from linear displacement transducers, a pressure profile, and the voltage signal profile from the delay generator. The RCM pistons have an inherent delay of approximately 100 ms before moving from the bottom dead center (BDC) to the top dead center (TDC) after the RCM unit is triggered, as shown in Figure 2.8. The optimal droplet trajectory provides a total time of flight of approximately 180 ms from injection to apex to impact. In addition, the compression time of the RCM pistons is approximately 20 ms. Therefore, the timing of the droplet injection into the combustion chamber is the key to maximizing the total induction period available for the droplets to ignite in the gaseous fuel/oxidizer/inert mixture.

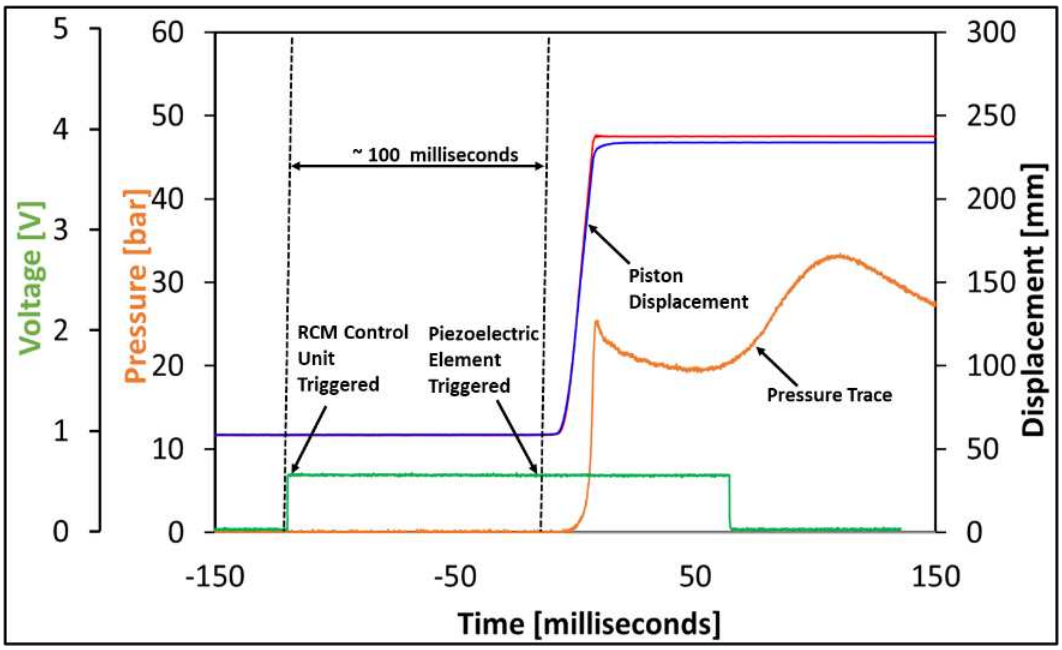

Figure 2.8. Data acquisition and control signals were obtained during a representative rapid compression machine experiment, including piston displacement, combustion chamber pressure, and voltage signal from the RCM control unit used to trigger the droplet generator.

2.4. Optical Imaging System

A Schlieren optical setup, as shown in Figure 2.9, is used to visualize the injection of the liquid fuel droplet, the evaporation profile of the droplet, the ignition of the droplet, and the propagation of the premixed flame in the gaseous fuel/oxidizer/inert mixture. High-speed Schlieren imaging is performed using a Photron FASTCAM SA5 camera at 50,000 fps. A pair of custom-fabricated 2.603 cm diameter sapphire optical windows are used to provide optical access for the camera and light source. The Schlieren system developed previously by Dumitrache et al. [51] was used for this study. A narrow band LED emitter ($\lambda = 400 - 405$ nm) and a dielectric mirror are used to allow only the reflection of light in the wavelength range of 400 to 410 nm, which limits the intensity of light hitting the photo sensor of the camera. This technique results in high quality Schlieren images that are used to measure droplet diameter, ignition delay period for the nonpremixed flame, and the position/velocity of the flame front of the propagating premixed flame. In addition, the

Schlieren images qualitatively indicate the location of vaporized fuel as the liquid fuel travels along its trajectory.

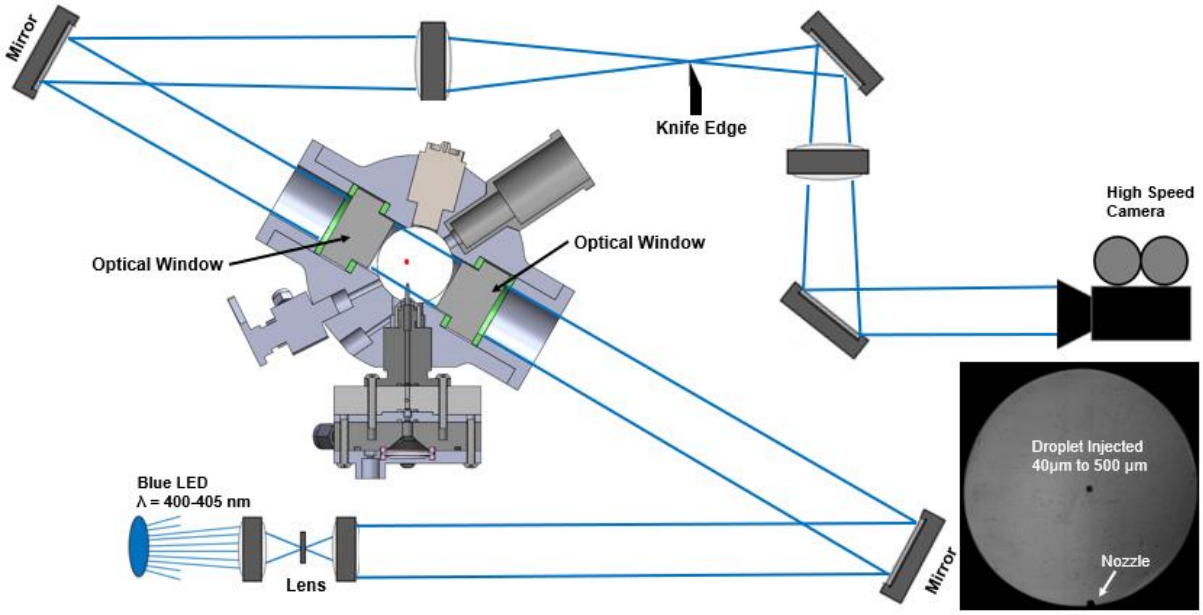

Figure 2.9. RCM Optical setup layout. The optical path of the Schlieren beam is shown in blue. Schlieren images of diesel droplets injected into the air in an opposed-piston rapid compression machine (RCM) showing the minimum (40 µm) and maximum (500 µm) liquid droplet size produced using a piezoelectric droplet generator.

The light from the LED, as shown in Figure 2.9, was passed through a slit that spatially filtered the beam and was subsequently collimated and steered through the combustion chamber domain using a pair of mirrors. As the light leaves the combustion chamber, it is focused on a knife edge that partially blocks the light beam. If the density disturbance is present in the mixture inside the combustion chamber, some of the light is steered away from the knife edge and reaches the camera. The droplet size is controlled by using nozzles of various diameters (40 to 500 µm) and by varying the pulse width and amplitude of the square wave supplied to the piezoelectric element. While the droplet size is controlled, in part, by the nozzle diameter, the droplet size is measured optically using an image analysis program (ImageJ), with a calibration factor (i.e., pixels per inch)

based on an image calibration at identical chamber conditions which resulted in an uncertainty of ± 40 μm in the droplet diameter. Ignition delay of the droplets is reported by visualizing the images and quantified as the difference between the time when pistons reach TDC and the first appearance of diffusion flame around the droplet.

2.5. Experimental Setup Validation

Initial testing and validation of the experimental setup were carried out using diesel as the liquid fuel and a mixture of methane/air at $\phi = 0.65$ as the gaseous medium. The nozzle size used for the test was 80 μm. The initial temperature and pressure for the gaseous fuel/air medium were 318 K and 1 bar, respectively, before RCM firing, and the initial droplet temperature was 318 K. The corresponding pressure and temperature at TDC were 26 bar and 854 K, respectively. For this experiment, both pistons arrived at TDC simultaneously with zero offset, which resulted in a near vertical droplet trajectory along the stagnation plane of the RCM, as evidenced by the droplet remaining in the field of view during the entire sequence in Figure 2.10.

As shown in Figure 2.10, the droplet was injected at time t = 0 ms, and the droplet injection process created two droplets. The smaller droplet size was 100 μm, and the larger droplet size was 270 μm. Both droplets remained in the field of view, and their trajectories reached their apex as the piston reached the TDC (t = 25 ms). Since both pistons reached TDC simultaneously (piston timing offset ≈ 0 ms), a perfect adiabatic core was established with negligible observed turbulence in the field of view. At t = 55 ms, the smaller droplet auto-ignited, which created an outwardly propagating premixed methane/air flame as observed at t = 56 ms and onwards. This premixed flame initially develops as a circular flame and slowly became elongated as it approached RCM pistons, cylinder walls, and the droplet injector tip.

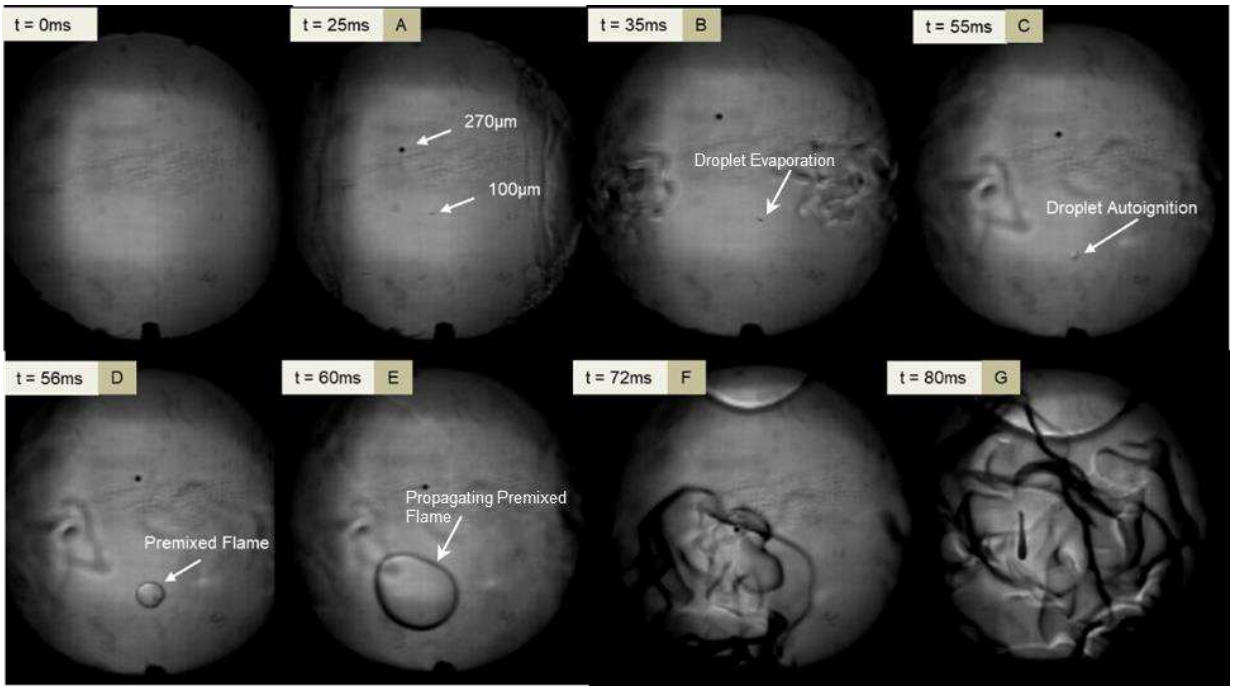

Figure 2.10. A sequence of Schlieren images from a High-Speed Camera at 50,000 fps showing dual fuel diesel droplet combustion in methane/air mixture of $\phi = 0.65$.

As the larger droplet began its downward trajectory and the premixed flame continued to propagate into a premixed methane/air mixture (t = 72 ms), the larger droplet traversed through the premixed flame front. By traversing the premixed flame front, the larger droplet was subjected to the elevated temperature of the post combustion gases, resulting in increased evaporation rate and flame temperature and subsequent autoignition. Since the methane/air mixture was lean (ϕ = 0.65), there was sufficient oxygen content (6.2 mol%) in the post combustion gases of the premixed flame, causing ignition of the droplet. As seen at time t = 80 ms, the larger droplet continued to burn, as evidenced by the trail of particulate matter.

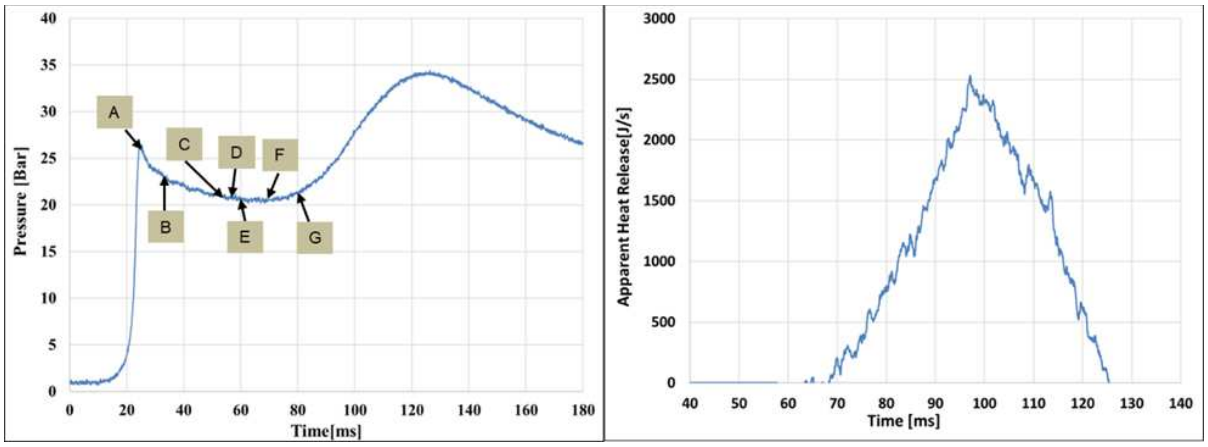

Figure 2.11. Pressure and apparent heat release rate for the dual fuel diesel droplet combustion in methane/air mixture of $\phi = 0.65$.

Figure 2.11 contains plots of measured pressure and apparent heat release rate during the combustion phenomena observed in Figure 2.10. The pressure data in Figure 2.11 and the Schlieren images in Figure 2.10 are notated with the letters A through G for comparison between the visual images of droplet combustion followed by premixed flame propagation and their effects on the measured combustion chamber pressure and apparent heat release rate.

Point C on the pressure curve coincides with the ignition of the smaller 100 µm droplet, followed by ignition and propagation of the premixed flame (points D, E, and F on the pressure curve). During this early stage of flame propagation, the increase in pressure observed from the propagating flame is balanced by the decrease in pressure due to heat loss to the combustion chamber walls. As the premixed flame continues to propagate after point F, the apparent heat release rate from combustion overcomes the heat loss to the combustion chamber walls, and the pressure rises until a peak pressure of 34 bar is observed at 122 ms after droplet injection. Based on the shape of the pressure curve and the associated apparent heat release rate plot, it appears that the premixed flame propagated to the wall where flame quenching occurred without end-gas autoignition. Previous work with laser ignited fuel/air mixtures in the same rapid compression

machine showed that it is possible to observe end-gas autoignition depending on the reactivity and temperature history of the end gas.

2.6. Conclusions

The novel piezoelectric droplet generator integrated with the rapid compression machine provides a valuable experimental setup in which a single isolated liquid hydrocarbon droplet can be injected into the air or gaseous fuel-air mixtures at elevated temperature and pressure conditions. Coupled with the high-speed Schlieren imaging diagnostics, the experimental setup can be used to study multiphase flow/droplet behaviors in reacting and non-reacting environments at thermodynamic states that have traditionally been too difficult to achieve and/or control.

The RCM can achieve temperatures up to 1000 K and pressures up to 40 bar (conditions emulating many real engineering applications) in the matter of ms without significant flow field disturbances. When coupled with optical access and high-speed diagnostics, this unique experiment offers remarkable capabilities to study sub- and supercritical droplet/phase change phenomenon and their auto-ignition behavior in a controlled and well characterized environment and, as such, provides data that is central to validating multidimensional fluid dynamic models. In addition to performing experiments at high pressures/temperatures, traditional experimental methods studying droplet dynamics and combustion often employ large, fiber-supported droplets, which are far larger than droplets observed in real combustion applications (mm dimensions rather than a micron). The droplet generator described here offers the ability to inject droplets in a free stream without a droplet suspension device within a range of diameters seen in real injectors and avoids the influence of the suspension device (e.g., unrealistic heat transfer and fluid mechanic effects) on the physical phenomenon being studied. With the ability to tightly control the operating

conditions, numerous experiments can be conducted by researchers using the experimental setup descried in this section which are as follows,

1. Fundamental studies on dual fuel combustion and lubricant oil triggered abnormal combustion phenomena described in this dissertation.
2. Fundamental multiphase flow behaviors, including sub- to the supercritical phenomenon, to understand the role of these physics in reacting and non-reacting flow systems, including but not limited to:
    a. Liquid droplet evaporation characteristics and the role of vapor-liquid equilibrium in non-reacting mixtures at various/relevant thermodynamic conditions (high pressures/temperatures).
    b. The study of the super- and trans-critical phenomenon of any standard liquid and to investigate the impact of multiple droplets under such supercritical conditions.
3. Analysis of droplet phase behaviors and potential combustion in varying/controlled flow fields, including varying degrees of turbulence.
4. A low cost/low fuel volume (microliters) cetane number measurement of next-generation low lifecycle carbon fuels, including sustainable aviation fuels and advanced carbon neutral fuels.

In this study, the above experimental setup is used to study the underlying fundamentals associated with dual fuel combustion and abnormal combustion triggered by lubricant oil droplets in natural gas engines by injecting various sizes of diesel and lubricant oil droplets ($50\ \mu m < d_o < 500\ \mu m$) in air and methane-air mixtures at elevated temperatures and pressure conditions.

CHAPTER 3: TRANSIENT ANALYTICAL DROPLET EVAPORATION MODEL

3.1. Droplet Evaporation Modeling Theory and Setup

In conjunction with the experiments, a computational modeling study was also conducted to develop models for understanding the dual fuel combustion and the lubricant oil droplet triggered abnormal combustion observed in natural gas engines. The modeling approach was divided into two sections:

1. Transient analytical droplet evaporation model
2. Converge CFD model to tackle droplet ignition and combustion

The transient evaporation model was developed by utilizing the fundamental theory of droplet evaporation, as shown in Figure 3.1, to accurately capture the evaporation rates of the fuel and oil droplets at various thermodynamic conditions. In this model, the properties of different fuels was specified without relying on default properties generally available within the commercial CFD software. This chapter discusses the transient analytical modeling approach and the parametric study results in detail. The data from the transient analytical evaporation model was used as an input condition to the Converge CFD model to simulate the combustion characteristics of different fuel and lubricants oil droplets.

The transient analytical droplet evaporation model utilizes the well-defined fundamental theory presented by Law et al. in the Combustion Physics textbook [52]. The developed model accounts for the heat transfer from the gas phase to the droplet surface, evaporation at the droplet surface, and heat transfer from the surface to the droplet interior. The surface temperature of the

droplet is calculated by assuming a unity lewis number, which equates to the mass and the heat transfer numbers associated with droplet evaporation theory.

$$B_{h,v} = B_{m,v} \tag{3.1}$$

where $B_{h,v} = \frac{C_p(T-T_s)}{q_v}$ is the heat transfer number and $B_{m,v} = \frac{Y_{F,s}-Y_{F,\infty}}{1-Y_{F,s}}$ is the mass transfer number. The above equation is solved for finding the droplet surface temperature and other parameters involved during droplet evaporation using a Transient Stepwise Quasi Steady iterative droplet evaporation model developed in MATLAB™ which uses the known pressure and temperature history from RCM experiments as shown in Figure 3.2. The above equation is solved at each time interval of the RCM experimental cycle, which helps study droplet evaporation in a transient high temperature and pressure environment as observed in the RCM combustion chamber.

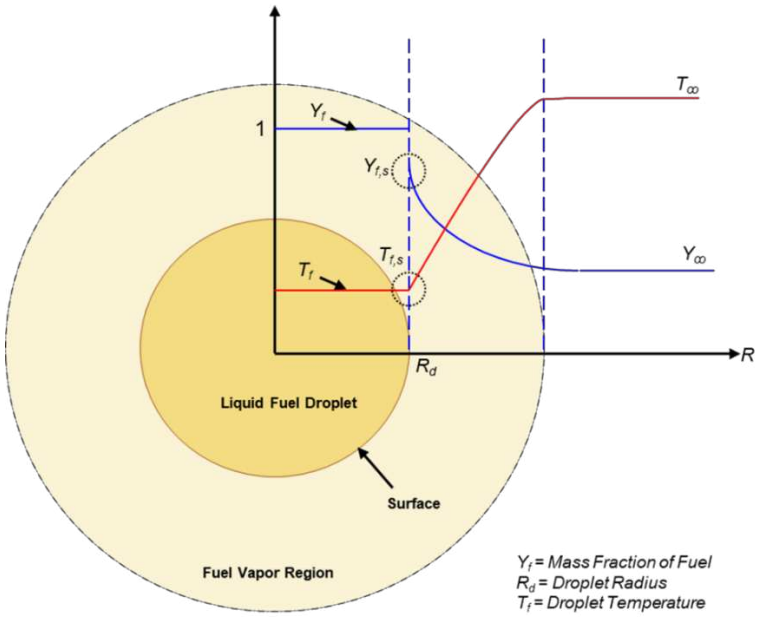

Figure 3.1. Schematic of the classical theory of droplet evaporation subjected to high ambient temperature

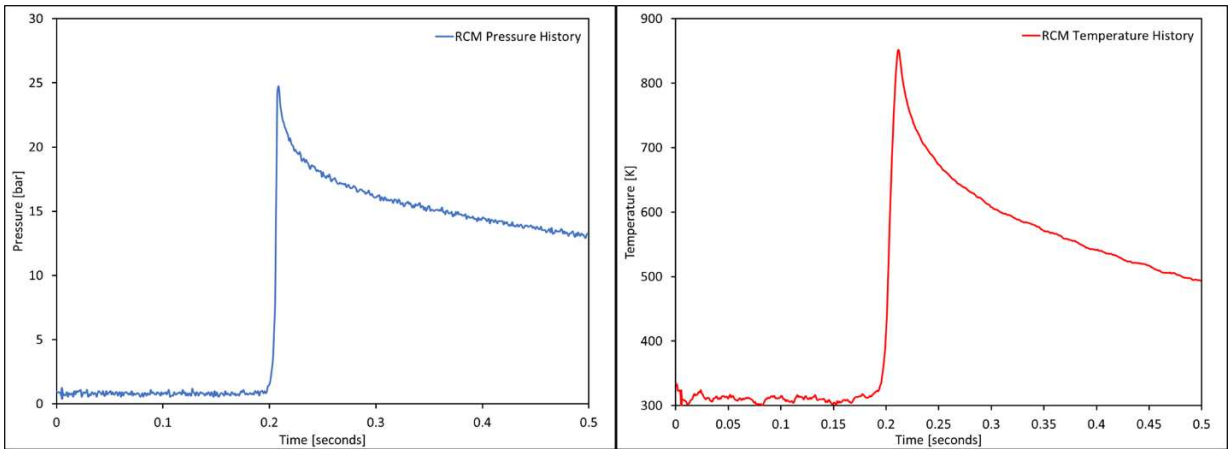

Figure 3.2. Typical Pressure and Temperature Profile during RCM Compression Stroke

The use of the RCM pressure history in the model allows to naturally account for the heat loss taking place near the wall of the RCM chamber and sleeves, which results in a decrease in surrounding temperature, as shown in Figure 3.2. As the surrounding temperature falls as RCM pistons reach TDC, the droplet's evaporation rate also decreases due to decreased surface temperature. The model accurately predicts this behavior of reduced surface temperature and gives the profile of the surface temperature of the droplet, as shown in Figure 3.3.

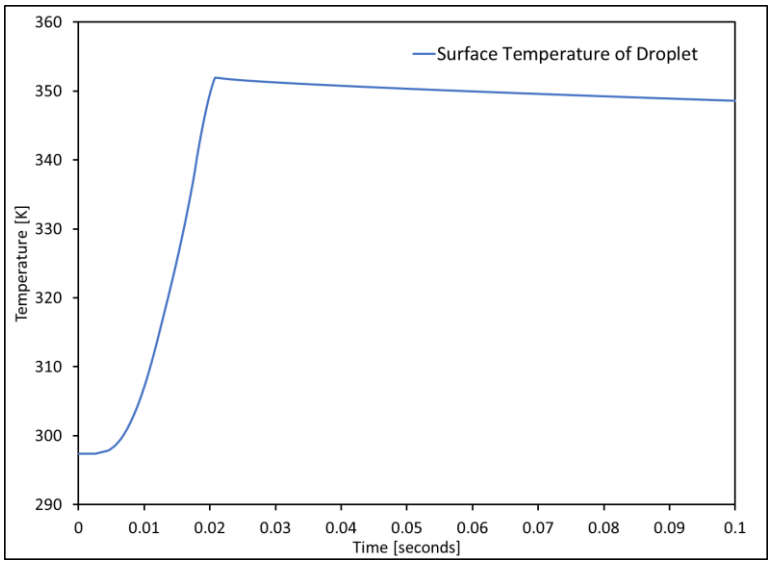

Figure 3.3. A typical droplet surface temperature profile when subjected to high pressure and temperature conditions of RCM

After the evaluation of surface temperature, the surface evaporation rate is determined analytically by solving the classical theory of droplet evaporation as described in the book of combustion physics by Law [52]. The theory of evaporation developed by Law et al. considers the liquid droplet to be stationary and not in a state of motion. However, in the RCM, the droplets are injected vertically into the RCM chamber, and the droplet follows a parabolic projectile which enhances the droplet evaporation rate due to additional convection introduced by droplet motion. To account for this increase in the evaporation rate by convection, a frossling empirical relation was used in the model, which relates the droplet evaporation rate at a quiescent condition when the droplet is stationary to the evaporation rate observed in the case of moving droplets.

$$\frac{k_u}{k_q} = 1 + aRe^n \quad \text{where a ~ 0.3 and n ~ 0.23-0.3} \tag{3.2}$$

where k_u is the evaporation rate of moving droplet, k_q is the evaporation rate of the quiescent droplet, and Re is the Reynolds number.

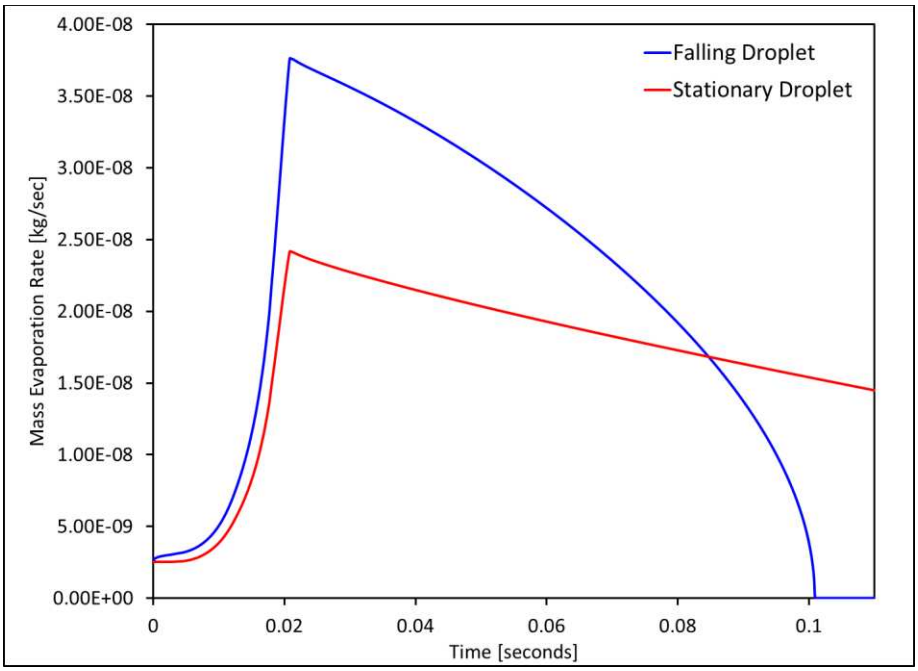

Figure 3.4. Comparison of the evaporation rate of a typical droplet falling under gravity and a stationary droplet

Figure 3.4 shows an enhanced evaporation rate for a droplet falling under gravity, whereas a stationary droplet has a lower evaporation rate when subjected to the RCM pressure and temperature history. The droplet under motion completely evaporated at ~ 100 milliseconds, at which the mass evaporation rate goes to zero, as shown in Figure 3.4. However, since the evaporation rate is low for the stationary droplet, it takes a longer time for it to evaporate completely, and as shown in Figure 3.4, the stationary droplet was not able to evaporate completely within the simulation runtime. The next step in the model development was introducing the heat losses occurring within and at the droplet surface. The theory provided by Deprédurand et al. [53] was used to resolve heat transfer around the droplet. The heat loss into the droplet interior was calculated as follows,

$$q = c_p(T_{interior} - T_{surface}) \tag{3.3}$$

where c_p is the specific heat of the liquid fuel, $T_{interior}$ is the interior temperature of the droplet and $T_{surface}$ is the surface temperature of the droplet. For calculating the interior temperature of the droplet, a condition of thermodynamic equilibrium was assumed for the heat transfer between the liquid droplet surface and the surrounding gases, and the following equation was used for solving the interior droplet temperature.

$$mc_p \frac{dT}{dt} = -hA_s(T_{interior} - T_{surface}) \tag{3.4}$$

where h is the overall heat transfer coefficient and $\frac{dT}{dt}$ is the gradient in the temperature in the gaseous phase. Integrating the above and applying the initial conditions, $T_{interior}$ can be calculated as follows,

$$T_{interior} = T_s + (T_i - T_{surface})e^{\frac{(-6ht)}{(\rho c_p D)}} \tag{3.5}$$

where T_i is the initial temperature of the droplet, D is the diameter of the droplet, and h is the heat transfer coefficient which is calculated using the theory of falling droplets [54]

$$h = \frac{Nu\ K}{D} \tag{3.6}$$

where Nu is the Nusselt number, K is the thermal conductivity, and D is the diameter of the droplet. The nusselt number for the falling droplet is calculated as follows,

$$Nu = 2 + \left(0.6Re^{\frac{1}{2}}Pr^{\frac{1}{3}}\right) \tag{3.7}$$

where Re is the Reynolds number and Pr is the Prandtl number of the liquid fuel droplet.

Solving the above equations allows calculating and accounting for various heat losses occurring near the droplet surface and in the droplet's interior. Considering the various heat losses associated with droplet evaporation and accounting for the heat loss from the RCM walls makes the model reliable for studying the evaporation of single isolated droplets subjected to the RCM chamber thermodynamic conditions. A comparison between the evaporation rate of a droplet when heat loss is considered and neglected is shown in Figure 3.5.

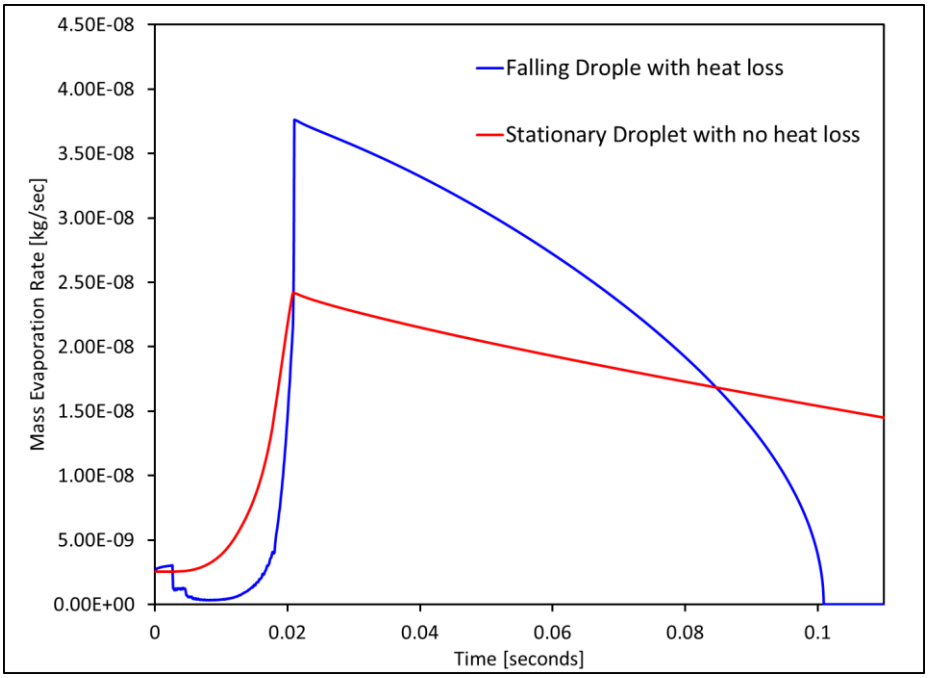

Figure 3.5. Comparison of the evaporation rate of a typical droplet falling under gravity with heat loss considered and a stationary droplet without considering heat loss

Figure 3.5 clearly shows that considering the heat loss associated with the droplet evaporation phenomenon in high temperature environment results in an initial slow rate of evaporation. However, as the droplet velocity increases during its downward trajectory, the evaporation rate is enhanced due to convection observed with the moving droplet. Accounting for the necessary physics associated with droplet evaporation, a sensitivity study was carried out to

determine the evaporation model's performance. The following parameters were considered for doing the sensitivity study.

1. Farfield temperature
2. Liquid droplet surface temperature
3. Liquid droplet velocity
4. Liquid droplet size

3.2. Sensitivity of Droplet Evaporation Modeling

3.2.1. Farfield Temperature

A 150 µm diesel droplet at 300 K initial surface temperature falling under gravity was subjected to 1 bar surrounding pressure, and a variable surrounding temperature ranging from 750 K to 1050 K. Figure 5 shows the result of the d^2 law of droplet size regression and the mass evaporation rate of the droplet for various farfield temperatures ranging from 750 K to 1050 K.

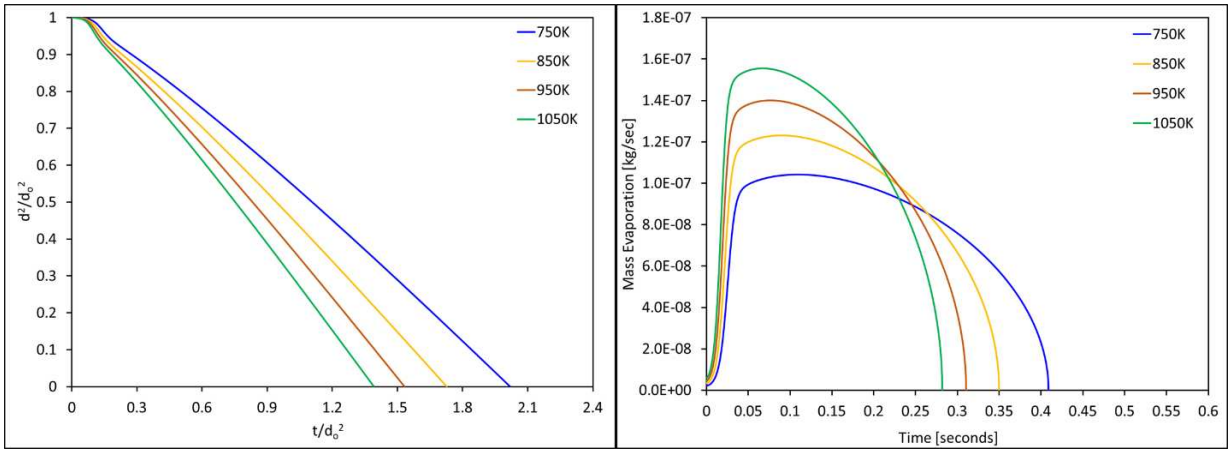

Figure 3.6. (a) Normalized droplet regression and (b) mass evaporation rate of a 150 µm diesel droplet

As shown, the droplet's evaporation rate is lowest at a lower farfield temperature of 750K and increases with increasing the surrounding temperature. At 1050K, the highest evaporation rate was

observed for 150 µm droplet. Also, the total lifetime for complete droplet evaporation increases with a decrease in the surrounding temperature.

3.2.2. Droplet Sizes

Different size diesel droplets at 300 K initial surface temperature falling under gravity were subjected to 1 bar surrounding pressure and 950 K surrounding temperature. Figure 3.7 shows the result of the mass evaporation rate for various droplet sizes when subjected to thermodynamic conditions similar to those observed in the Rapid Compression Machine.

As shown, the droplets' mass evaporation rate is significantly influenced by the droplet size. A smaller droplet evaporates quickly, but as the droplet size increases, the magnitude of the evaporation rate is increased due to an increase in the heat losses within the droplet interior. The overall evaporation lifetime of droplets increases with an increase in droplet sizes.

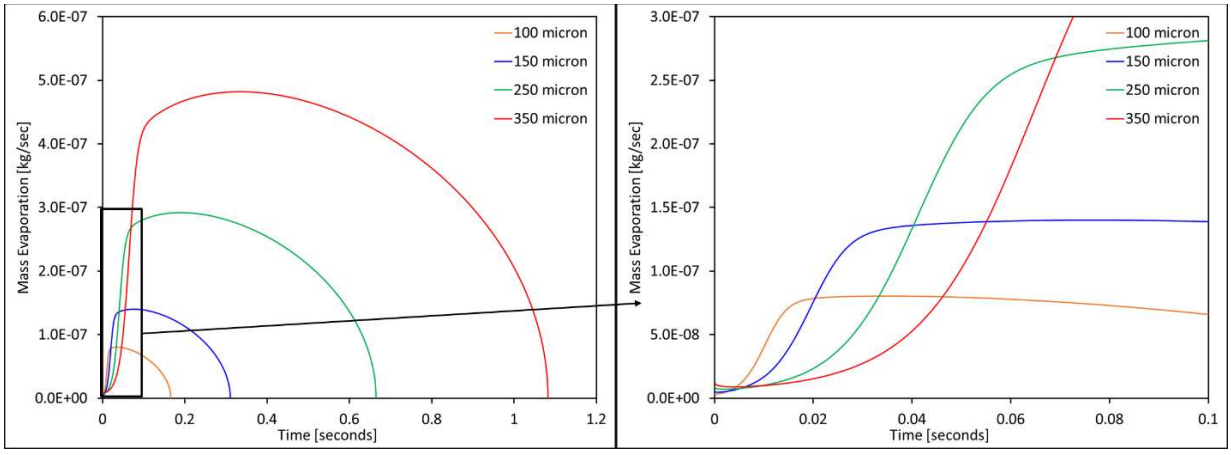

Figure 3.7. Mass evaporation rate for different diesel droplet sizes subjected to pressure and temperature of 1 bar and 950 K

3.2.3. Initial Liquid Droplet Temperature

A diesel droplet of 350 µm falling under gravity was subjected to 1 bar surrounding pressure and 950 K surrounding temperature. The surface temperature of the droplet was varied to study its effect on the droplet's evaporation rate. The temperature of the droplet was varied from room temperature of 300 K to its boiling point of 538 K. Figure 3.8 shows the result of the mass evaporation rate of the droplet for different droplet surface temperatures when subjected to the thermodynamic conditions similar to those observed in the Rapid Compression Machine.

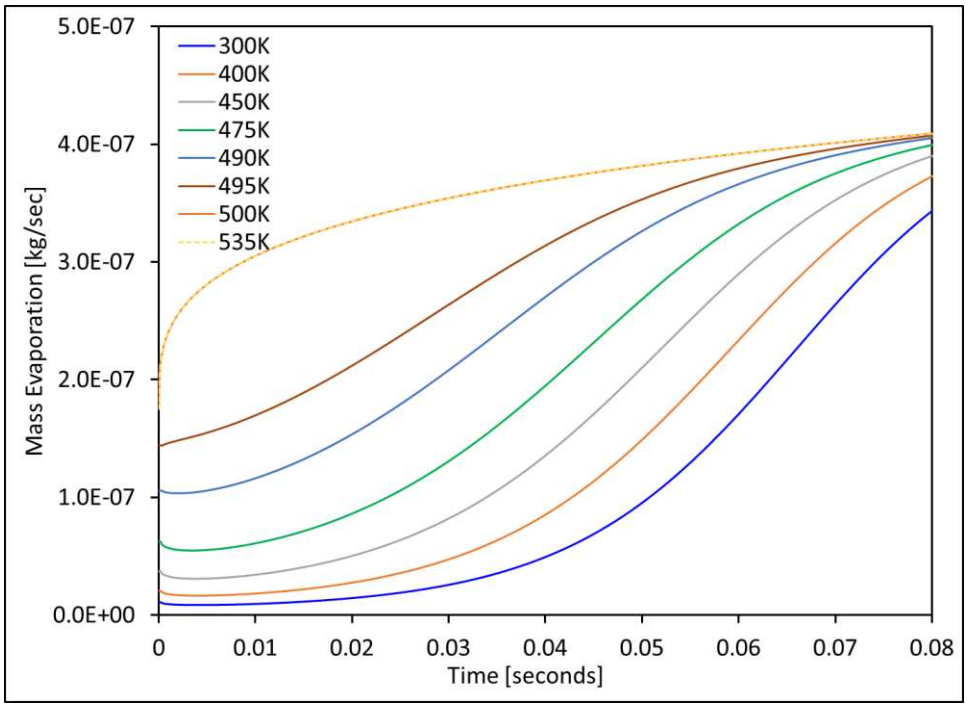

Figure 3.8. Mass evaporation rates for various diesel droplet surface temperatures subjected to pressure and temperature of 1 bar and 950 K

As shown in Figure 3.8, an increase in evaporation rate is observed with an increase in the surface temperature of the droplet. At surface temperatures closer to the boiling point of the liquid, the curvature of the mass evaporation profile flips, and the evaporation rate increases significantly, as observed for the surface temperature of 500 K and 535 K in Figure 3.8.

3.2.4. Droplet Velocity

A diesel droplet of 150 µm with a surface temperature of 300 K was subjected to 1 bar surrounding pressure and 950 K surrounding temperature. The moving velocity of the droplet was varied to study its influence on the evaporation rate. Figure 3.9 shows the result of the mass evaporation rate of 150 µm diesel droplet moving at different velocities and the influence of droplet velocity on the droplet diameter regression rate.

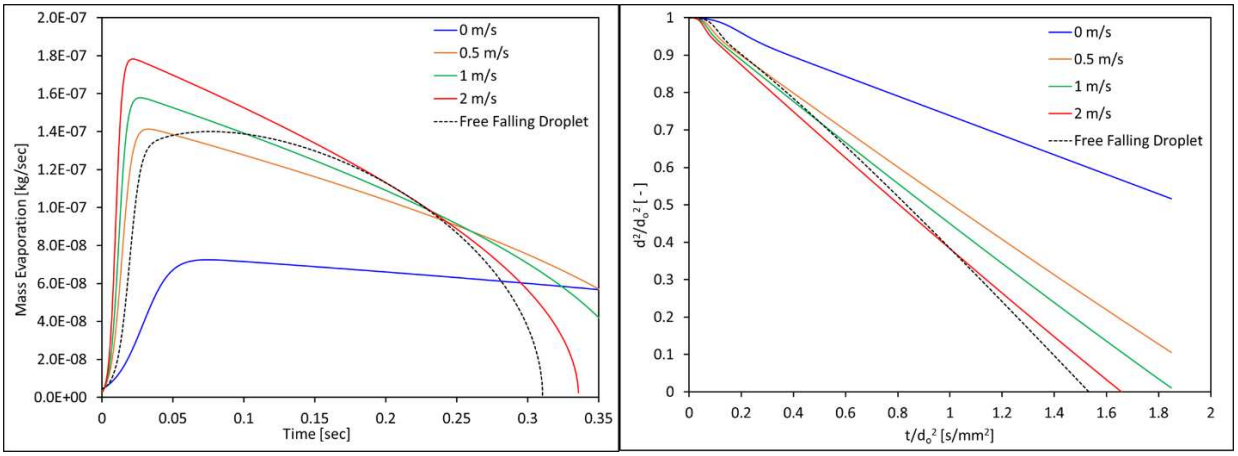

Figure 3.9. (a) Mass evaporation rate and (b) normalized droplet regression rate for a 150 µm diesel droplet at the surface temperature of 300 K subjected to various velocity profiles

As shown in Figure 3.9, it can be concluded that the droplet's mass evaporation rate increases with the droplet velocity increase. The black dotted line indicates the droplet evaporation rate and droplet regression rate when the droplet is injected from the nozzle. The initial mass evaporation rate is lower as droplet velocity is low since the droplet travels toward the apex against gravity. However, during the downward journey of the droplet, the velocity of the droplet is constantly increasing, resulting in increased convection and, thus faster evaporation and lower overall droplet evaporation time, as shown in Figure 3.9.

3.3. Validation of Droplet Evaporation Modeling

The sensitivity study shows that the transient analytical droplet evaporation model is sensitive to the initial droplet size, initial droplet temperature, droplet motion, and surrounding temperature. To further validate the evaporation model, a literature survey was carried out to collect an experimental dataset of droplet evaporation and compare the model developed to the available dataset. An evaporation study of heptane droplets carried out by Pinheiro et al. [55] in 2019 was selected as the dataset to compare the transient analytical droplet evaporation model. The necessary well-known properties of heptane were then provided to the model, and simulations were carried out at the same experimental conditions given by Pinheiro et al. in their work. The heptane droplet size of 500 µm at an initial droplet temperature of 300 K with surrounding temperature varied from 473 K to 748 K, and surrounding pressure maintained at 1 bar was used as the simulation conditions.

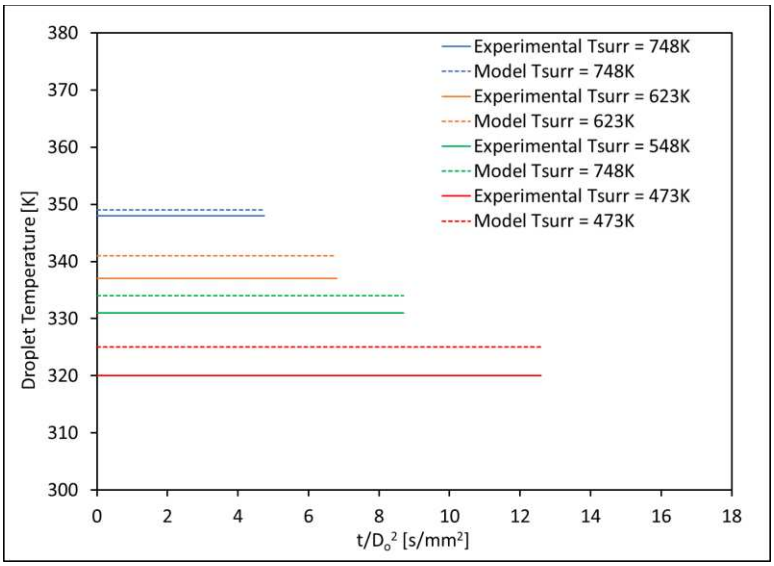

Figure 3.10. Experimental and Simulated Surface Temperatures of 500 µm heptane droplet when subjected to different surrounding temperatures ranging from 473 K to 748 K

As shown in Figure 3.10, the heptane droplet's surface temperature increases with the surrounding temperature. A good agreement is observed between the simulation and the experimental dataset for predicting the surface temperatures of the heptane droplets. Since a constant temperature is maintained in the surrounding, the surface temperature of the droplet remains steady, and no decrease in surface temperature is observed. As shown, the predictability of surface temperature observed in the experiments increases with increasing the surrounding temperature. At 748 K, the surface temperature prediction is 349 K which is very close to the surface temperature observed by Pinheiro et al. in their study.

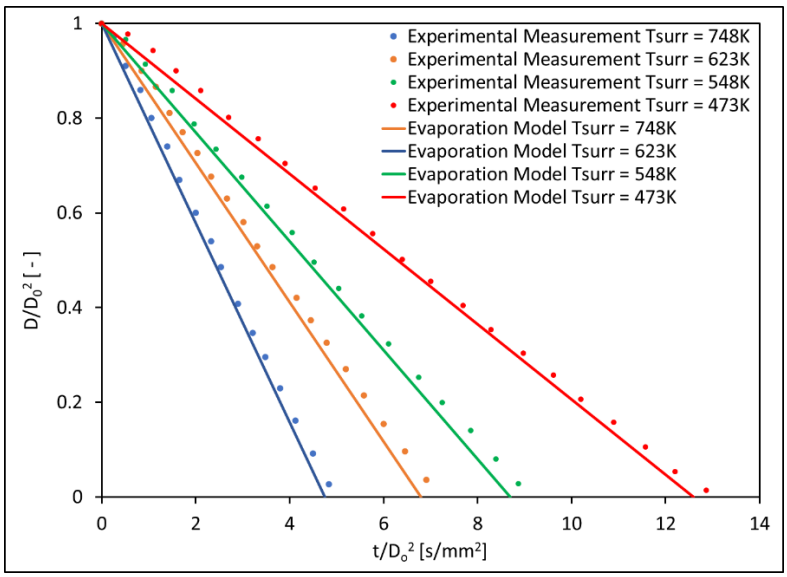

Figure 3.11. Experimental and Simulated droplet regression rate of 500 µm heptane droplet when subjected to different surrounding temperatures ranging from 473 K to 748 K

With a good agreement observed between the experimental and simulated droplet surface temperatures, a further comparison was carried out between the experiments and the evaporation model for predicting the droplet regression rate and overall droplet lifetime. As seen in Figure 3.11, a good agreement is observed between the experimental and the simulated droplet regression rate. The evaporation model can predict the droplet regression rate close to the experimental

observations. A good agreement was also observed for predicting the overall droplet evaporation lifetime for all temperature conditions at which experiments were conducted.

3.4. Conclusion

The transient analytical droplet evaporation model was successfully developed using the classical droplet evaporation theory. Enhanced convection due to droplet motion was also introduced into the model. Since classical droplet evaporation theory does not account for the different heat losses associated with droplet evaporation, additional parameters are included in the model based on the study of Deprédurand et al. [53] to include all the heat fluxes associated with an evaporating droplet in a hot ambient environment. The model developed was found to be sensitive to the following parameters,

1. Farfield Temperature
2. Initial Liquid Droplet Temperature
3. Droplet Velocity
4. Droplet Sizes

A sensitivity and validation study of the transient analytical droplet evaporation model was successfully conducted. The validated evaporation model was then used to perform a three-dimensional computational fluid dynamic (CFD) study to understand the ignition and combustion characteristics of single hydrocarbon droplets in air and methane/air mixtures at various thermodynamic conditions. For CFD studies, the droplet's evaporation rate and its surface temperature predicted from the analytical droplet evaporation model were used as an input conditions to model the evaporating droplet. Details about the CFD models are provided in Chapter 4.

CHAPTER 4: COMPUTATIONAL COMBUSTION MODEL

4.1. CONVERGE CFD code and Numerical Scheme

Modeling of two fuels of disparate reactivities, namely the high reactivity fuel diesel interacting with low reactivity fuel methane and air was carried out using CONVERGE^{TM} version 3.0.21. The entire geometry of RCM was used in the simulation along with the complete stroke of the RCM pistons from bottom dead center to top dead center. CONVERGE^{TM} code uses a cartesian style mesh and solves the surface fluxes of mass, momentum, and energy transport using a cell-centered finite volume method using 2nd-order central differencing. The time marching method used a fully implicit form of the transport equation. The PISO method, a predictor corrector method, was used to couple the velocity and pressure fields. This method first solves the velocity field and then implicitly updates the velocity field using the implicit pressure solution.

In Converge^{TM}, partial differential equations (PDE) for mass, momentum, and energy equations are solved simultaneously to find the pressure gradient. Turbulence and species equations are also solved in addition to the above mentioned equations. The compressible form of the mass and momentum PDEs using Einstein notation are respectively,

$$\frac{\partial \rho}{\partial t} + \frac{\partial \rho u_i}{\partial x_i} = 0, \tag{4.1}$$

and,

$$\frac{\partial \rho u_i}{\partial t} + \frac{\partial \rho u_i u_j}{\partial x_j} = -\frac{\partial P}{\partial x_i} + \frac{\partial \sigma_{ij}}{\partial x_j} + S_i, \tag{4.2}$$

where the viscous stress tensor, σ_{ij}, is given by,

$$\sigma_{ij} = \mu\left(\frac{\partial u_i}{\partial x_j} + \frac{\partial u_j}{\partial x_i}\right) + \left(\mu' - \frac{2}{3}\mu\right)\frac{\partial u_k}{\partial x_k}\delta_{ij}. \tag{4.3}$$

In the above equations, ρ is the density, u_i is the velocity component, P is the pressure, S is the source term, μ is the dynamic viscosity, μ' is the dilation viscosity (assumed to be zero), and δ_{ij} is the Kronecker delta. The turbulence model was employed by replacing the viscosity with the sum of molecular and turbulent viscosity according to,

$$\mu_{tot} = \mu + \mu_t = \mu + C_\mu \rho \frac{k^2}{\varepsilon} \tag{4.4}$$

where C_μ is a model constant, k is the turbulent kinetic energy, and ε is the turbulent dissipation rate. A more detailed description of the transport equations' turbulent forms can be found in the converge manual [56]. The energy equation is given as,

$$\frac{\partial \rho e}{\partial t} + \frac{\partial u_j \rho e}{\partial x_j} = -P\frac{\partial u_j}{\partial x_j} + \sigma_{ij}\frac{\partial u_i}{\partial x_j} + \frac{\partial}{\partial x_j}\left(K\frac{\partial T}{\partial x_j}\right) + \frac{\partial}{\partial x_j}\left(\rho D \sum_m h_m \frac{\partial Y_m}{\partial x_j}\right) + S, \tag{4.4}$$

where e is the specific internal energy, K is the thermal conductivity, T is the temperature, D is the mass diffusivity, h_m is the specific enthalpy of species m, Y_m is the mass fraction of species m, and S is an energy source term. While using the turbulence modeling, the thermal conductivity is replaced by the sum of molecular and turbulent conductivity according to,

$$K_{tot} = K + K_t = K + c_p \frac{\mu_t}{Pr_t}, \tag{4.5}$$

where c_p is the constant pressure specific heat capacity and Pr_t is a user-specified turbulent Prandtl number. The species transport equation is defined as,

$$\frac{\partial \rho_m}{\partial t} + \frac{\partial \rho_m u_j}{\partial x_j} = \frac{\partial}{\partial x_j}\left(\rho D \frac{\partial Y_m}{\partial x_j}\right) + S_m, \tag{4.6}$$

where ρ_m is the density of species *m* (i.e., $\rho_m = \rho Y_m$) and S_m is the source term for species m due to chemical reaction. The species transport equation is solved explicitly in the code. For calculating the molecular mass diffusivity, a user-supplied Schmidt number, *Sc,* is used and is given as,

$$D = \frac{\nu}{Sc}. \tag{4.7}$$

The turbulent mass diffusivity replaces the molecular mass diffusivity according to,

$$D_t = \frac{\nu_t}{Sc_t}, \tag{4.8}$$

where $\nu_t = \mu_t/\rho$ is the turbulent kinematic viscosity and Sc_t is a user-supplied turbulent Schmidt number. For all the RCM simulations in this work Sc_t = 0.78, which is a typical value for air was used. The Redlich-Kwong equation of state was employed using air's critical pressure and temperature, as explained in the CONVERGE™ theory manual [56], for coupling the pressure, density, and temperature in the compressible transport equations. The gas phase properties are defined in the input file *gas.dat.* This file consists of dynamic viscosity, μ, and thermal conductivity, *k*, as functions of temperature from 0 K to 5000 K.

The time step size was controlled by employing a variable time step method which limits the timestep by considering various parameters. Converge™ uses three different Courant-Friedrichs-

Lewy (CFL) numbers: the convection-based CFL number, diffusion-based CFL number, and Mach-based CFL number. These numbers are defined as follows,

$$CFL_u = u\frac{\Delta t}{\Delta x}, \tag{4.9}$$

$$CFL_\nu = \nu\frac{\Delta t}{\Delta x^2}, \tag{4.10}$$

$$CFL_{mach} = a\frac{\Delta t}{\Delta x}, \tag{4.11}$$

where u is the velocity, ν is the kinematic viscosity, a is the speed of sound, Δx is the cell width, and Δt is the time step size. If CFL_u =1, then the time step is limited such that a massless species in the simulation cannot travel more than one cell width.

The timestep was also controlled depending on the chemical reaction rate in the domain. While solving for the chemistry, the maximum allowable timestep was,

$$\Delta t_{chem} = \Delta t_{prev} \times \min\left[\frac{T}{\Delta T}\right] \times mult\_dt\_chem, \tag{4.12}$$

where Δt_{prev} is the previous time step, T is the initial cell temperature, ΔT is the temperature change due to chemical reaction, and *mult_dt_chem* is a user-specified input. Thus, if *mult_dt_chem* = 0.5, then the time step is restricted such that any cell's temperature change is less than 50% of the initial cell temperature.

Details about the working algorithm of PISO can be found in the CONVERGE™ manual [56]. In each PISO loop, transport equations in their discretized form are solved iteratively using a point-

wise selective over-relaxation algorithm. This method repeatedly solves the transport equations until the iteration error for each solution variable converges within the user-specified error tolerance.

$$error_{\varphi} = \frac{\Delta\varphi}{norm}, \tag{4.13}$$

where φ is a solution variable, $\Delta\varphi$ is the change in the solution variables between successive SOR iterations, and the *norm* is a normalization value for φ. After completing the PISO loop, a final iteration is carried out using the point-wise Jacobi method is used to ensure the conservation of the solution variables. After this, turbulence equations are solved using new solution variables.

4.2. Geometry

All the simulations carried out in this work used a complete RCM geometry. The piston motion from the bottom dead center (BDC) to the top dead center (TDC) was modeled in the three-dimensional CFD simulations based on the data obtained from the linear transducer of RCM for the actual piston displacement in experiments. A base mesh of 1.5 mm was used for the simulations. Temperature and velocity gradients were modeled using adaptive mesh refinement, which was coupled with the spherical embedding along the droplet source term to resolve the species distribution with high accuracy and precision. Fixed embedding was also employed near the walls of the RCM chamber and sleeves to resolve the boundary layer and accurately solve the heat transfer at the RCM wall.

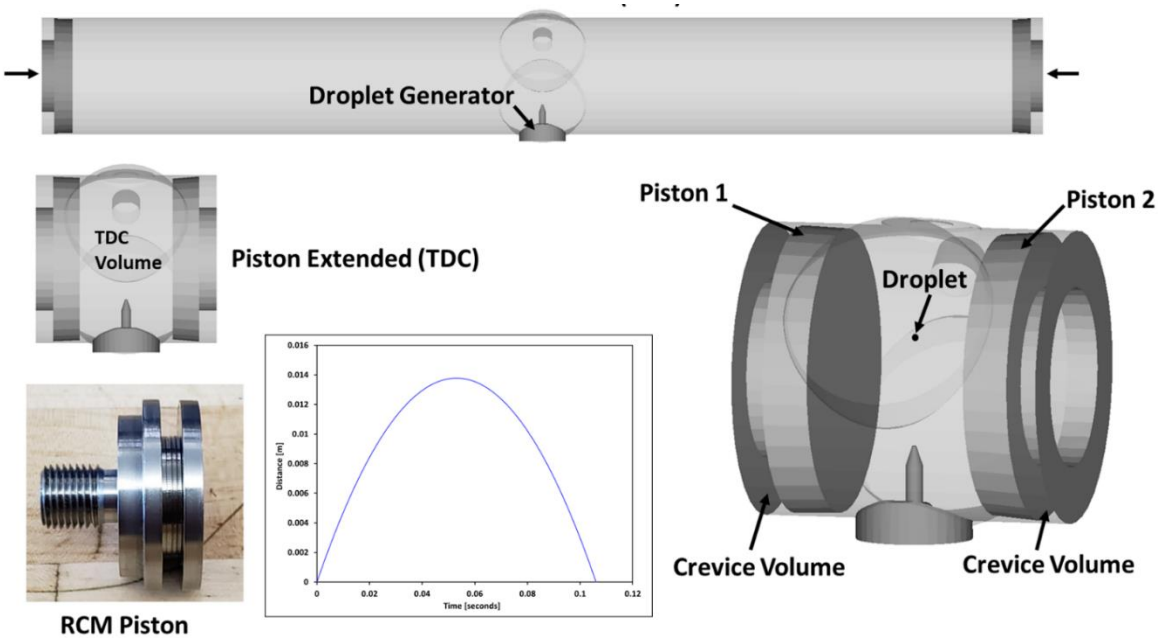

Figure 4.1. The RCM geometry used for the simulations in this work. RCM crevice piston picture is also shown to show the crevice volume

The RCM geometry used for the CFD simulations is shown in Figure 4.1. The crevice pistons are used in the RCM experiments and simulations to arrest the roll-up vortices in the crevice volume and obtain a turbulent free adiabatic core at the center of the RCM combustion chamber. The RCM simulations captured these details of restraining the roll-up vortices in the crevice volume, and a turbulent free adiabatic core was achieved in the RCM chamber domain. The droplet was modeled as a solid spherical boundary which acted as a source term of species for which the motion was specified using the user-defined function, and the evaporation rate was imposed on the boundary using the evaporation profile obtained from the transient analytical droplet evaporation model.

4.3. Turbulence Model

Diffusion rates of mass, momentum, energy, and species are primarily influenced by the presence of turbulence in the domain. The diffusion rate increases with increased turbulence;

hence, it is crucial to resolve the turbulence systematically and efficiently. In this study, there is an interaction between high and low-reactivity fuels. The chemical reaction rates associated with this interaction strongly depend on how the turbulence is resolved in the domain. For this study, the RANS turbulence model is used to carry out all the simulations. RANS stands for Reynolds Averaged Navier-Strokes. In a RANS model, the actual velocity, u_i, is decomposed into a mean velocity component, $\bar{u}_i$, and a fluctuating velocity component, u'_i,

$$u_i = \bar{u}_i + u'_i \tag{4.14}$$

Substituting the fluctuating velocity and mean velocity component into the Navier-Stokes equations results in analogous ensemble-averaged quantities for the solution variables and gives an additional term to describe the effects of turbulence. In the momentum equation, this additional turbulence term is called the Reynolds stress tensor and is defined as,

$$\tau_{ij} = -\overline{\rho u'_\iota u'_\jmath}, \tag{4.15}$$

The Reynold stress tensor term introduces a few more variables to be solved in the Navier Stroke equations. To solve these additional equations, an additional turbulent viscosity term is used in the momentum equation, and the thermal conductivity term is used for the energy equation. A new variable called turbulent mass diffusivity is used for the species equation. The RANS model calculates turbulent viscosity and turbulent conductivity by solving two additional transport equations for turbulent kinetic energy, *k*, and turbulent dissipation rate, ε. The turbulent kinetic energy is defined as,

$$k = \frac{1}{2}\widetilde{u'_i u'_j}. \tag{4.16}$$

The turbulent dissipation rate is defined as the rate at which the turbulent kinetic energy of the smallest eddies is transformed into molecular thermal energy. The turbulent viscosity is then found using the values for k and ε as follows,

$$\mu_t = C_\mu \rho \frac{k^2}{\varepsilon} \tag{4.17}$$

where C_μ is a model constant. This turbulent viscosity is then added to the molecular viscosity in the momentum equation. Turbulent thermal conductivity then can be defined using the turbulent viscosity as follows,

$$K_t = \left(\frac{1}{\mathrm{Pr}_t}\right)\mu_t c_p, \tag{4.18}$$

and a turbulent mass diffusivity,

$$D_t = \left(\frac{1}{\mathrm{Sc}_t}\right)\mu_t. \tag{4.19}$$

The RANS model uses user-specified turbulent Prandtl number (Prt) and Schmidt (Sct) numbers. In this study for all the simulations, $\mathrm{Pr_t} = 0.9$ and $\mathrm{Sc_t} = 0.78$ is used. Reynold stress term in the momentum equation is modeled using the turbulent viscosity as follows,

$$\tau_{ij} = 2\mu_t S_{ij} - \frac{2}{3}\delta_{ij}\left(\rho k + \mu_t \frac{\partial \tilde{u}_i}{\partial x_i}\right), \tag{4.20}$$

where,

$$S_{ij} = \frac{1}{2}\left(\frac{\partial \tilde{u}_i}{\partial x_j} + \frac{\partial \tilde{u}_j}{\partial x_i}\right). \tag{4.21}$$

S_{ij} is the strain tensor. RANS models represent the effect of turbulent eddies, which increases the diffusion rate by increasing the values of viscosity and thermal conductivity. In this study, the main focus is to understand the interaction of the fuels with disparate reactivities and study the interaction in a negligible turbulent environment, as observed in the RCM. RANS solver predicts the flow's ensembled average behavior, not the domain's instantaneous flow field, but is sufficient to yield a helpful simulation result.

The renormalization group (RNG) k-ε from Han and Reitz [57] was used as the turbulence model in this study. The transport equation for *k* is given as,

$$\frac{\partial \rho k}{\partial t} + \frac{\partial \rho u_i k}{\partial x_i} = \sigma_{ij}\frac{\partial u_i}{\partial x_j} + \frac{\partial}{\partial x_i}\frac{\mu}{\mathrm{Pr}_k}\frac{\partial k}{\partial x_j} - \rho\varepsilon + S_s, \tag{4.22}$$

where Pr_k is a Prandtl number describing the ratio of viscous diffusion to the diffusion of *k,* and S_s is a source term used by the spray model to represent turbulent kinetic energy transferred from the gas phase to the liquid parcels. The transport equation for ε is,

$$\frac{\partial \rho\varepsilon}{\partial t} + \frac{\partial (\rho u_i \varepsilon)}{\partial x_i} = \frac{\partial}{\partial x_j}\left(\frac{\mu}{\mathrm{Pr}_\varepsilon}\frac{\partial \varepsilon}{\partial x_j}\right) + c_{\varepsilon 3}\rho\varepsilon\frac{\partial u_i}{\partial x_i} + \left(c_{\varepsilon 1}\frac{\partial u_i}{\partial x_j}\tau_{ij} - c_{\varepsilon 2}\rho\varepsilon + c_s S_s\right)\frac{\varepsilon}{k} - \rho R, \tag{4.23}$$

where for the RNG model, the R term is,

$$R = \frac{C_\mu \eta^3 (1 - \eta/\eta_0)}{(1 + \beta\eta^3)} \frac{\varepsilon^2}{k}. \tag{4.24}$$

The η term in equation (4.24) is,

$$\eta = \frac{k}{\varepsilon} |S_{ij}| = \frac{k}{\varepsilon} \sqrt{2 S_{ij} S_{ij}}. \tag{4.25}$$

In equation 4.25, Prε describes the ratio of viscous diffusion to the diffusion of ε and $c_{\varepsilon 1}$, $c_{\varepsilon 3}$, and $c_{\varepsilon 1}$ are model constants. In the RANS turbulence model, a turbulent length scale is defined to correctly resolve the grid for representing turbulent diffusion rates. The length scale is given as,

$$le = {C_\mu}^{3/4} \frac{k^{3/2}}{\varepsilon}, \tag{4.26}$$

where C_μ is a model constant. The cell width should be less than *le* in areas where combustion occurs to ensure accuracy in combustion rate.

More details about turbulence modeling can be found in the Converge User Manual [56]. The flow field observed in the RCM experiments was modeled using the RANS turbulence modeling. The averaged flow field observed in the simulations was very similar to that observed in the RCM combustion domain.

4.4. Boundary Conditions

For the RCM simulations, the RCM walls and sleeves were modeled as stationary walls. RCM pistons were modeled as translating walls with the motion specified from the data obtained using the linear transducers of RCM. The RCM walls were provided with homogeneous Neumann conditions for pressure, species, passives, and turbulent kinetic energy. The wall model was used for the turbulent dissipation rate. All the surfaces were set to have zero surface roughness. The turbulent law of the wall functions was used for the velocity and temperature boundary conditions. Law of the wall functions are logarithmic fits of a turbulent boundary layer and are necessary at high Reynolds number flows because resolving the viscous sub-layer would require very small cells that would be computationally expensive. When using a RANS k-ϵ turbulence model, CONVERGE uses the velocity law of the wall from Launder and Spalding [58], which uses a Von Karmen constant of 0.42. The turbulent heat transfer model of Amsden [59] was used for temperature. These wall functions are described in further detail within the CONVERGE™ theory manual [56].

4.5. Chemistry Model

A reduced dual-fuel natural gas/diesel chemical kinetic mechanism developed by Hockett and coworkers [6] was used for all the simulations involving dual-fuel combustion of diesel droplets injected in natural gas air mixtures. The mechanism consists of 141 species and 709 reactions. This reduced mechanism was obtained by separately reducing a detailed n-heptane mechanism [7][8] and a detailed C_5 mechanism [9] using the direct relation graph method [10]. The reduced natural gas/diesel mechanism was tested and validated against ignition delay computations with detailed chemical kinetic mechanisms and CH_4/O_2/He experimental premixed laminar flame speeds at 40

and 60 atm. In the dual fuel study, diesel was modeled as n-heptane due to similar ignition delay properties as diesel [60] and similar heating value. Natural gas was modeled as methane as a significant percentage of natural gas comprised of methane gas.

In developing the model for understanding the abnormal combustion triggered by lubricant oil droplets in natural gas engines, another reduced chemical kinetic mechanism developed by Hockett and coworkers [61] was used. This reduced mechanism was developed for primary reference fuel study. The mechanism consists of 186 species and 1014 reactions. This study modeled different lubricant oils as a surrogate of n-dodecane and xylene. Four different lubricant oils are tested in this study and based on their reactivity, a different percentage of n-dodecane and xylene was used to represent these lubricant oil's ignition characteristics. Natural gas is modeled as methane in this study as well.

4.6. Computational Hardware

Most simulations were performed on the CSU's ASHA High-Performance Computing System. This system model contains 21 nodes, two processors per node, and 40 cores per processor. Each node contains 192 GB of memory. Complete Rapid Compression Machine simulations typically use 40 to 80 cores. CONVERGE was run using MPICH to handle the parallel processing.

CHAPTER 5: DUAL FUEL IGNITION AND COMBUSTION STUDY OF DIESEL DROPLETS INJECTED IN CH4/O2/INERT MIXTURES

5.1. Introduction

There is an economic incentive to utilize natural gas in dual fuel applications and to maximize the substitution percentage of natural gas since natural gas is historically less expensive than diesel fuel per unit of energy. However, since natural gas substitution schemes often utilize high compression ratio engines, the natural gas substitution percentage is often limited by engine knock and uncontrolled fast combustion [5][6]. Maximization of the natural gas substitution percentage requires a greater understanding of the processes that lead to uncontrolled combustion rates in dual-fuel engines. The high expense of developing, fabricating, and testing new engines has motivated engine manufacturers to develop computational fluid dynamic (CFD) models for predicting engine behavior. These CFD models utilize various sub-models that simulate combustion chemistry, liquid fuel injection processes, gaseous intake and exhaust processes, heat transfer to cylinder walls, and in-cylinder fluid mechanics to understand the behavior of a full engine [5]. The accuracy of these engine CFD models can be maximized by independently validating each sub-models under engine-like operating conditions (i.e., elevated temperature and pressure).

To accurately simulate the dual fuel combustion process in engines, chemical kinetic mechanisms must accurately capture both the ignition kinetics of the diesel/natural gas blend in the vicinity of the diesel spray and the premixed flame propagation of the natural gas flame that is initiated after ignition. Hockett and coworkers [6] developed a dual-fuel natural gas/diesel reduced chemical kinetic mechanism consisting of 141 species and 709 reactions by separately reducing a detailed n-heptane mechanism [7][8] and a detailed C_5 mechanism [9] using the direct relation

graph method [10]. The reduced natural gas/diesel mechanism was tested and validated against ignition delay computations with the full detailed chemical kinetic mechanisms and $CH_4/O_2/He$ experimental premixed laminar flame speeds at 40 and 60 atm. However, no experimental data were available to independently test the ability of the mechanism to accurately reproduce the ignition delay of the diesel/natural gas blend in the vicinity of the spray and the transition of that ignition event into a propagating flame. In this work, we examine the experimental system of ignition of a single liquid fuel droplet in a gaseous fuel/air mixture at elevated temperature and pressure as a means to study the fundamental combustion processes of ignition and flame propagation in dual fuel engines and to generate experimental data that can be used to independently test dual fuel chemical kinetic mechanisms.

5.2. RCM Experiments

RCM experiments were conducted in which single isolated diesel droplets of sizes 50 μm to 500 μm were injected vertically in $O_2/N_2/Ar$ mixtures and in $CH_4/ O_2/N_2/Ar$ mixtures at various equivalence ratios ranging from $0 < \phi < 1.2$. The TDC temperature was swept from 700 K to 950 K with constant TDC pressure of 24 bar. Droplet sizes and velocity was controlled by controlling the pulse width and amplitude of the square wave supplied to the piezoelectric element and by using a nozzle of different sizes. Experimental results show droplet ignition's different combustion regimes at various thermodynamic and mixture conditions. Ignition delay dataset is also obtained, which can further be used to validate the chemical kinetic mechanism associated with dual fuel combustion (e.g., CSU 141 mechanism developed by Hockett et al.) and also for developing future dual fuel chemical kinetic mechanisms.

5.3. RCM Experiments

5.3.1. Diesel Droplet Combustion in $O_2/N_2/Ar$

To demonstrate the ability to inject and ignite liquid hydrocarbon droplets using the system described in Chapter 2, diesel droplet combustion experiments were performed for a range of droplet diameters (50 μm < d_o < 380 μm) and compressed temperatures (700K < T_c < 935K) and at a compressed pressure of 24 bar. Experiments were conducted with initial liquid droplet temperatures of 299 K and 343 K, respectively. Certification 2007 Ultra Low Sulfur Diesel (ULSD) was used for these, and subsequent experiments are reported below.

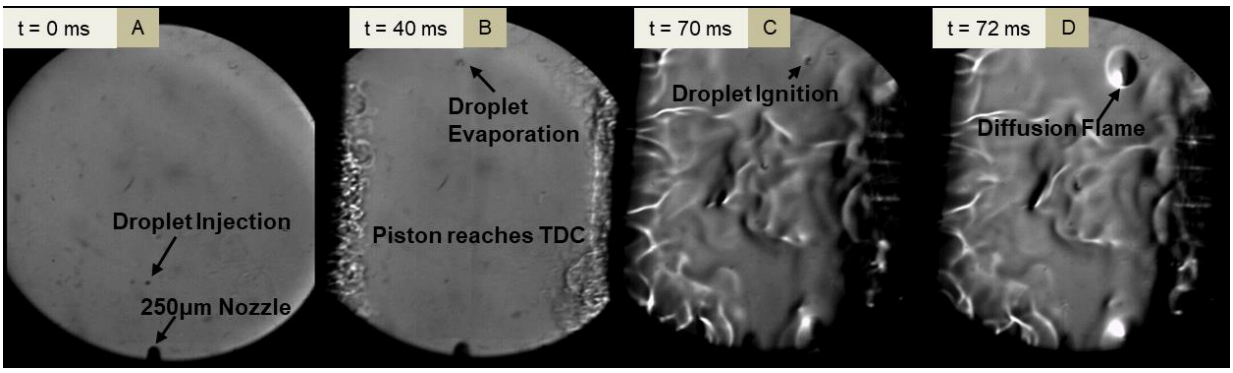

Figure 5.1. The sequence of Schlieren images from a High-Speed Camera at 50,000 fps showing diesel droplet combustion in 21%O2, 79% Inert at 935K

As shown in Figure 5.1(A), just before the pistons begin to displace, a 250 μm diesel droplet is injected into the $O_2/N_2/Ar$ mixture inside the RCM combustion chamber at an initial pressure of 900 millibars and an initial temperature of 300 K. The droplet follows an upward trajectory along the stagnation plane of the chamber and reaches an apex just before the piston reaches the TDC as shown in Figure 5.1(B). With pistons approaching the TDC at compressed temperature and pressure of 935 K and 24 bar, respectively, the droplet has begun to vaporize, as evidenced by the vapor cloud surrounding the liquid droplet. After a brief period of further droplet vaporization, mixing, and chemical kinetic induction period, the diesel/oxygen mixture surrounding the liquid

droplet ignites, as shown in Fig. 5.1(C), forming a non-premixed flame that envelope the droplet as shown in Figure 5.1(D).

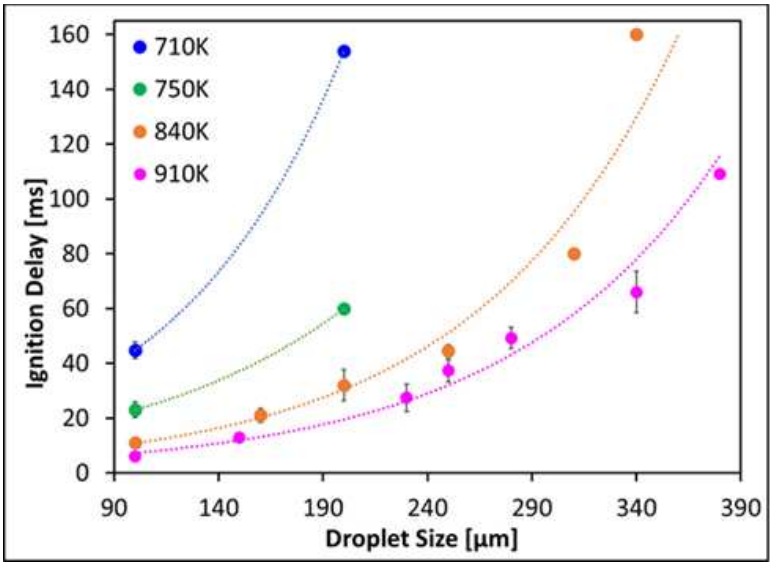

Figure 5.2. Ignition delay for different diesel droplet sizes at three elevated TDC temperatures of 710K, 750K, 840K, and 935K

Figure 5.2 is a plot of the ignition delay period for liquid diesel droplets with an initial liquid temperature of 299 K when subjected to compressed temperatures of 710 K < T_c < 910 K at compressed pressure of 24 bar. An increase in the ignition delay period was observed with increasing initial droplet diameter and decreasing compressed temperature. At 710 K, the increase in the ignition delay as the droplet size increased from 100 µm to 200 µm was substantial, increasing from 45 ms to 154 ms, and for droplet diameters larger than 200 µm, no droplet ignition was observed during the time of flight of the droplet (≈ 180 ms). Conversely, at higher temperatures of 840K and 935K, the increase in ignition delay with droplet diameter was moderate at smaller droplet sizes up to 250 µm and then increased more dramatically beyond droplet sizes greater than 250 µm.

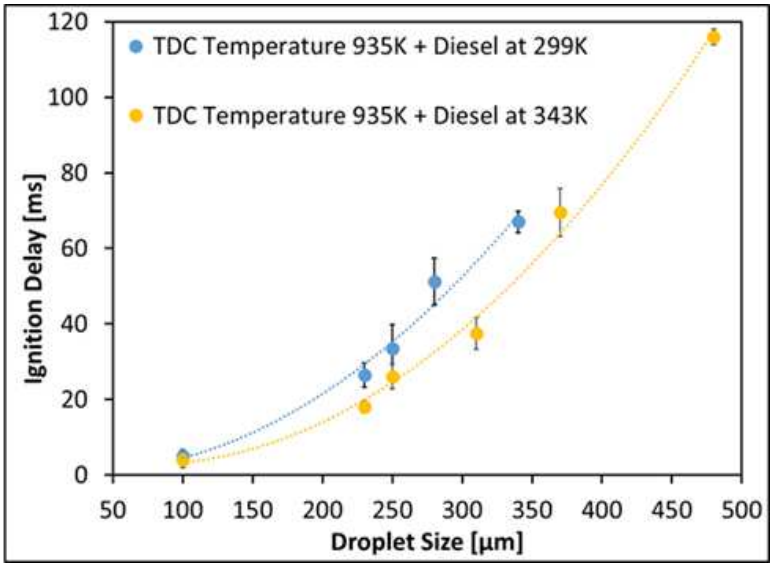

Figure 5.3. Ignition delay for various diesel droplet sizes at elevated TDC temperature of 935K with and without liquid droplet heating.

Figure 5.3 is a comparison of the ignition delay period of heated diesel droplets at 343 K and unheated diesel droplets at 299 K as a function of initial droplet diameter at a compressed temperature of 935 K. Shorter ignition delay periods were observed for the heated droplets for all droplet diameter ranges (150 µm < d_o < 380 µm), as compared to the unheated diesel droplets. By heating the liquid droplets, ignition was observed in initial droplet diameters of up to 500 µm, compared to the unheated liquid droplets for which ignition was not observed for droplet diameters greater than 380 µm during the time of flight of the droplets.

5.3.2. Diesel Droplet Combustion in Lean CH_4/O_2/Inert Mixtures

Dual fuel droplet combustion experiments were performed using 2007 ULSD certification diesel droplets in gaseous CH_4/O_2/Inert mixtures. A sequence of Schlieren images are shown in Figure 5.5 for a representative experiment of diesel droplet combustion in a lean CH_4/O_2/Inert mixture at an equivalence ratio $\phi = 0.6$. The nozzle used for this experiment had a 250 µm orifice diameter and produced a 350 µm droplet. The initial temperature and pressure for the CH_4/O_2/Inert

mixture in the combustion chamber were 300 K and 900 millibar, respectively, before RCM firing, and the initial droplet temperature was maintained at 299 K. The corresponding pressure and temperature at TDC were 24 bar and 910 K, respectively. In the experimental results shown in Figure 5.5, both pistons arrived at TDC simultaneously with zero offset, which resulted in a near vertical droplet trajectory along the stagnation plane of the RCM, as evidenced by the droplet remaining in the field of view during the entire sequence shown in Figure 5.5.

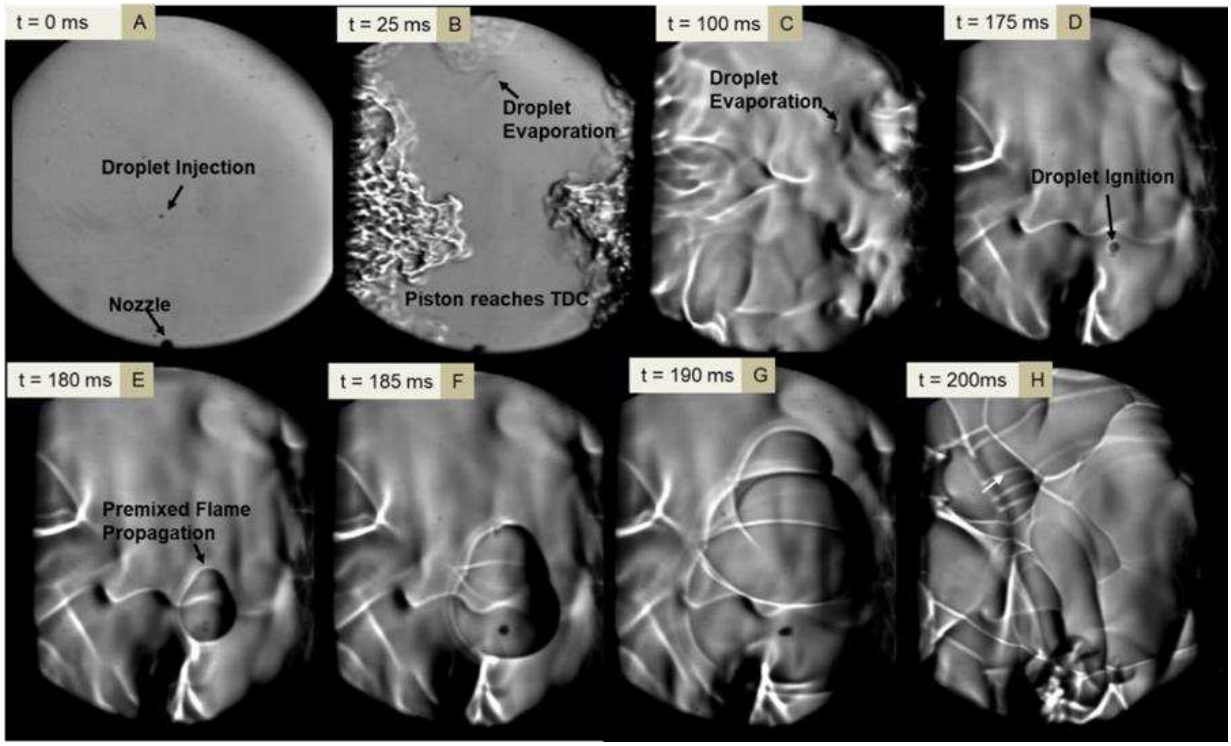

Figure 5.4. A sequence of Schlieren images from a high-speed camera at 50,000 fps for combustion of a 350 μm diesel droplet in CH_4/O_2/Inert mixture of $\phi = 0.6$. The compressed pressure and temperature (at point B) are 24 bar and 910 K, respectively.

As shown in Figure 5.5, the droplet was injected at time t = 0 ms, and the droplet injection process created a single isolated droplet of 350 μm. The droplet remained in the field of view, and its trajectory reached the apex as the pistons reached TDC (t = 25 ms). Since both pistons reached TDC simultaneously (piston timing offset ≈ 0 ms), a perfect adiabatic core was established with

negligible observed turbulence in the field of view. After the piston reached TDC, the droplet began to vaporize due to elevated temperature and pressure, as evidenced by the vapor trail observed in the Schlieren image. As the vaporizing droplet began its downward trajectory, a diesel vapor trail was created in the wake of the droplet. The diesel vapor trail mixed with the surrounding CH_4/O_2/Inert mixture and locally increased the equivalence ratio greater than $\phi = 0.6$, and since diesel fuel is more reactive than CH_4, it also increased the local chemical reactivity. At t = 175 ms, there was sufficient vapor concentration at favorable conditions to result in the ignition in the wake of the falling droplet - just above the droplet in Figure 5.5(d). The initial ignition kernel then created an outwardly propagating premixed CH_4/O_2/Inert flame as observed at t = 180 ms and onwards. This premixed flame initially develops as a spherical flame as observed at t = 175 ms and then becomes asymmetrical because the local flame speed is faster in the vicinity of the diesel vapor trail, which is locally closer to stoichiometric than the balance of the flow field.

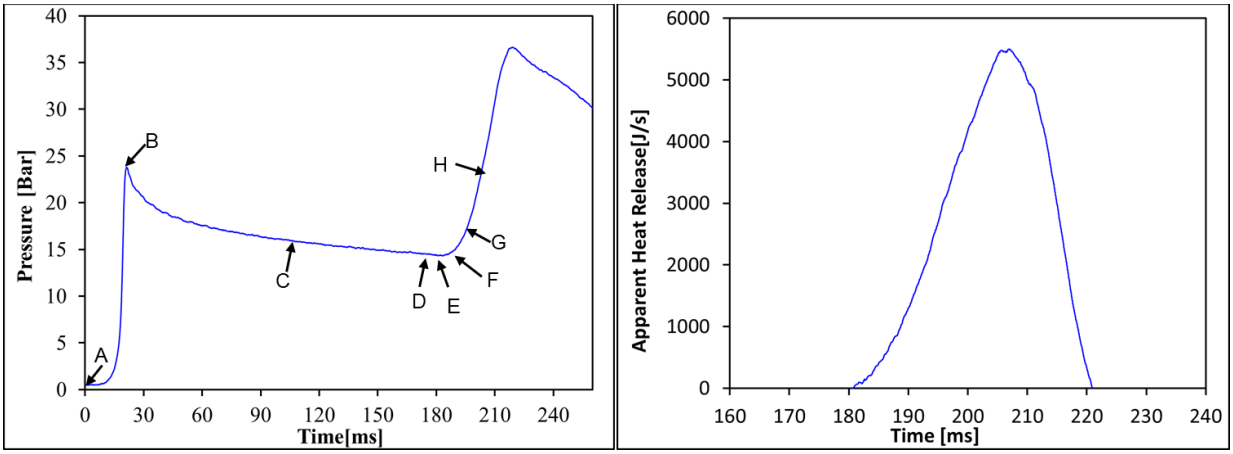

Figure 5.5. (a) Measured pressure in the rapid compression machine and (b) calculated apparent heat release rate for combustion of a 350 μm diesel droplet in CH_4/O_2/Inert mixture of $\phi = 0.6$. The compressed pressure and temperature (at point B) are 24 bar and 910 K, respectively.

Figure 5.6 contains plots of measured pressure and apparent heat release rate during the combustion phenomena observed in Figure 5.5. The pressure data in Figure 5.6, as well as the Schlieren images in Figure 5.5, are notated with the letters A through H for comparison between the visual images of droplet combustion followed by premixed flame propagation and their effects on the measured combustion chamber pressure and apparent heat release rate. Point D on the pressure curve coincides with the ignition of the droplet, followed by ignition and propagation of the premixed flame (points E, F, G, and H on the pressure curve). During the early stage of flame propagation, the increase in pressure observed from the propagating flame is balanced by the decrease in pressure due to heat loss to the combustion chamber walls. As the premixed flame continues to propagate after point E, the apparent heat release rate from combustion overcomes the heat loss to the combustion chamber walls, and the pressure rises until a peak pressure of 36 bar was observed at 220 ms after droplet injection. Based on the shape of the pressure curve and the associated apparent heat release rate plot, it appears that the premixed flame propagated to the wall where flame quenching occurred without end-gas autoignition [62].

5.3.3. Diesel Droplet Combustion in Stoichiometric and Rich CH_4/O_2/Inert Mixtures

Dual fuel diesel droplet combustion tests were also performed by injecting diesel droplets into stoichiometric and rich CH_4/O_2/Inert mixtures. A sequence of Schlieren images are shown in Figure 5.7 for a representative experiment of diesel droplet combustion in a stoichiometric CH_4/O_2/Inert mixture. The initial temperature and pressure were 300K and 900 millibar, respectively, before RCM firing, and the initial diesel droplet temperature was 299 K. The nozzle used for this experiment had an 80 μm orifice diameter and produced a 140 μm diesel droplet. The corresponding pressure and temperature at TDC were 24 bar and 910 K, respectively. Also, in this

experiment, both pistons arrived at TDC simultaneously with zero offset, which resulted in a near vertical droplet trajectory along the stagnation plane of the RCM, as evidenced by the droplet remaining in the field of view during the entire sequence shown in Figure 5.7.

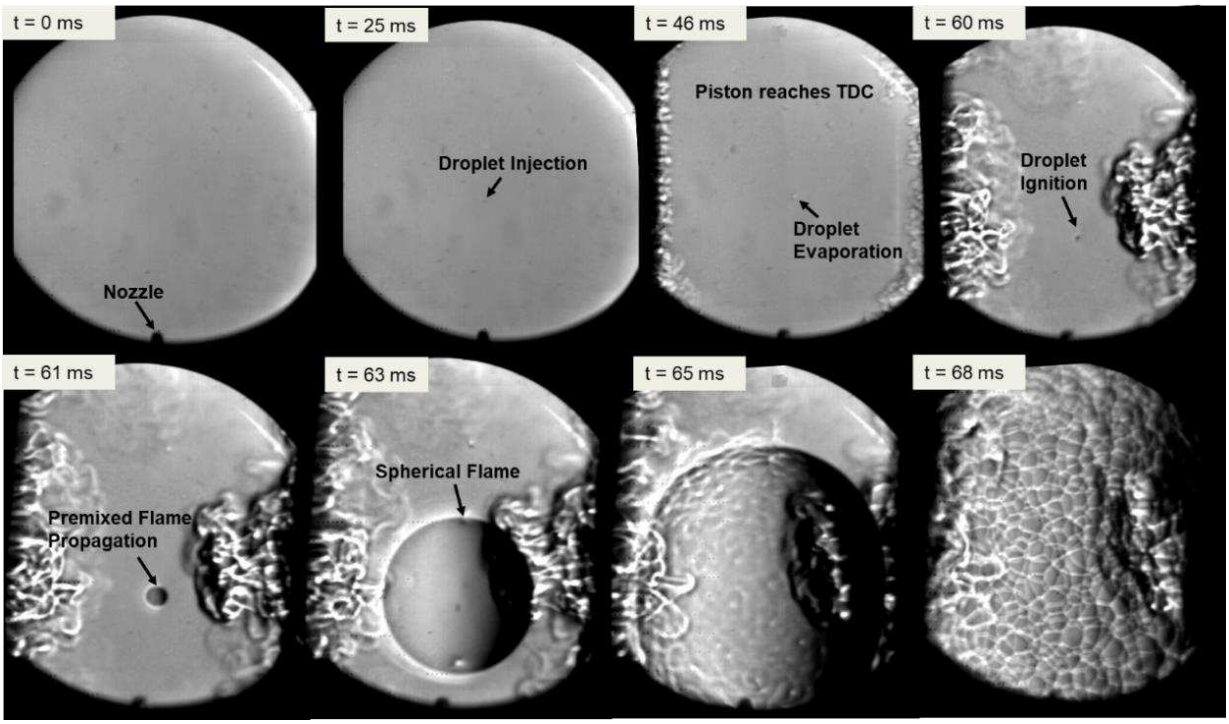

Figure 5.6. Sequence of Schlieren images from high-speed camera at 50,000 fps for combustion of a 140 μm diesel droplet in CH4/O2/Inert mixture of ϕ= 1.0. The compressed pressure and temperature (at t = 46 ms) are 24 bar and 910 K, respectively.

As shown in Figure 5.7, the droplet was injected at time t = 0 ms, and the injection process created a single isolated droplet of 140 μm. The droplet remained in the field of view, and its trajectory reached the apex as the pistons reached TDC (t = 46 ms). Since both pistons reached TDC simultaneously (piston timing offset ≈ 0 ms), a stagnant adiabatic core was established with negligible observed turbulence in the field of view. After the piston reaches TDC, due to elevated temperature, droplet vaporization is visible. As the droplet began its downward trajectory, a diesel vapor trail is visible behind the droplet, which mixed with the surrounding CH_4/O_2/Inert mixture

and locally increased the equivalence ratio to $\phi > 1.0$ within the vapor trail. At t = 60 ms, the droplet ignited, which created a spherical outwardly propagating premixed CH_4/O_2/Inert flame as observed at t = 61 ms and onwards. This spherical nature of flame propagation is a consequence of the local flame speed remaining nearly constant along the flame front in the vicinity of the slightly rich mixtures of CH_4/vaporized diesel fuel/O_2/Inert ($\phi \approx 1.2$).

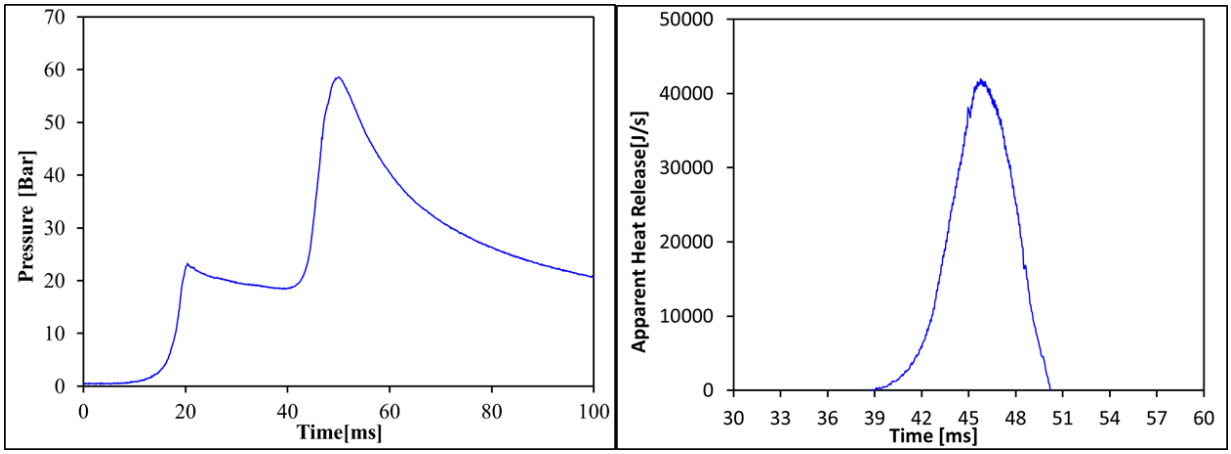

Figure 5.7. Measured pressure in the rapid compression machine and (b) calculated apparent heat release rate for combustion of a 140 μm diesel droplet in CH_4/O_2/Inert mixture of $\phi = 1.0$. The compressed pressure and temperature are 24 bar and 910 K, respectively.

As shown in Figure 5.8, the droplet ignition results in a rapid pressure rise in the RCM combustion chamber due to the formation of a propagating premixed flame. During the early stage of flame propagation, the increase in pressure observed from the propagating flame is balanced by the decrease in pressure due to heat loss to the combustion chamber walls. In the later stage, an increase in the pressure by propagating premixed flame overcomes the pressure fall by heat loss, and a net rise in the pressure and heat release is observed. Based on the shape of the pressure curve and the associated apparent heat release rate plot, it appears that the premixed flame propagated to the wall where flame quenching occurred without end-gas autoignition.

5.3.4. Diesel Droplet Combustion in Lean CH_4/O_2/Inert Mixtures moving with Higher Velocities

A lean CH_4/O_2/Inert mixture was used as the gaseous fuel and oxidizer medium with an equivalence ratio $\phi = 0.6$. A nozzle size of 80 μm was chosen for these experiments to produce droplets that would evaporate and autoignite during its trajectory and ignite a premixed CH_4/O_2/Inert flame. The initial temperature and pressure for the gaseous CH_4/O_2/Inert medium was 303K and 1 bar before RCM firing, and the initial liquid diesel droplet temperature was 343 K. The corresponding pressure and temperature at TDC were 24 bar and 910 K, respectively. A sequence of Schlieren images for this experiment are shown in Figure 5.9. The 80 μm nozzle injected a single diesel droplet of 100 μm (t= 5 ms). The piston offset for this test was 6 ms, which caused the droplet to move out of the viewing area (t = 25 ms). As the second piston approached near the TDC, the droplet reversed its direction and moved back into the viewing area (t=29 s).

The heated diesel droplet created a vapor trail in the wake of the droplet, which increased the local reactivity and equivalence ratio of the fuel/air mixture resulting in the ignition at t = 31 ms to the left of the liquid droplet. The ignition event transitioned into a premixed flame that propagates outward into the CH_4/O_2/Inert mixture from the wake of the liquid droplet. Since diesel is more reactive than natural gas and the local equivalence ratio is closer to stoichiometric, the flame moves much faster along the diesel vapor trail left by the moving droplet. At t = 45 ms, the premixed flame moved out of the viewing area but continued to propagate into the CH_4/O_2/Inert mixture. This result is similar to the results obtained from a similar study conducted by Ohtomo et al. [33].

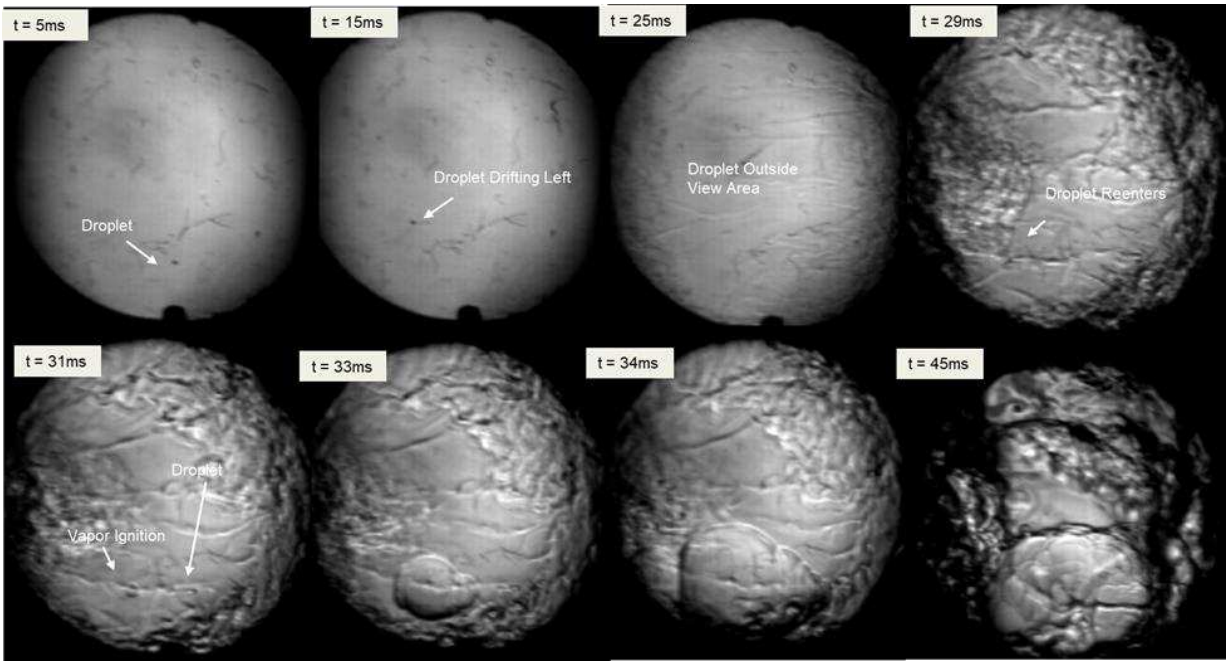

Figure 5.8. Sequence of Schlieren Images from High-Speed Camera at 50,000 fps showing dual fuel diesel droplet combustion in methane/air mixture of $\phi = 0.6$

Comparing the results from heated moving diesel droplets and non-heated stationary diesel droplet combustion in CH_4/O_2/Inert mixtures, several significant differences are observed. Diesel droplets at room temperature and having low to negligible velocities evaporate slowly, resulting in autoignition occurring near the droplet surface, resulting in a spherical nonpremixed flame that engulfs the liquid droplet, which subsequently ignites a spherical premixed CH_4/O_2/Inert flame. Conversely, a diesel droplet heated to high temperature and moving at high velocities enhances the evaporation rate, producing a sufficient vapor trail to raise the reactivity and equivalence ratio locally, resulting in an autoignition location behind the liquid droplet. The autoignition event transitions into a premixed flame that propagates toward the diesel droplet, as shown in Figure 5.9.

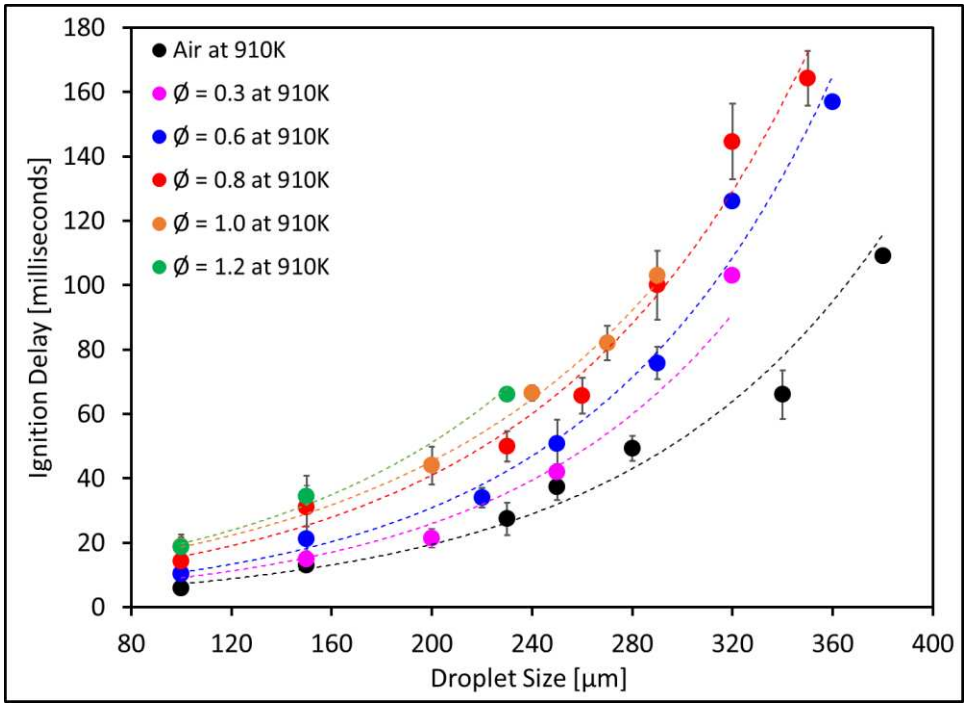

Figure 5.9. Ignition delay period as a function of initial droplet diameter for the compressed temperature of 910 K, respectively, for diesel droplets injected into $CH_4/O_2/N_2/Ar$ mixtures at an equivalence ratio of $0 < \phi < 1.2$.

Diesel droplet ignition experiments were also performed in gaseous $CH_4/O_2/N_2/Ar$ mixtures at compressed temperatures ranging from $710\ K < T_c < 935\ K$ over a range of equivalence ratios ($0 < \phi < 1.2$). For these experiments, the initial liquid droplet temperature was maintained at 299 K. Figure 5.10 is a plot of the ignition delay period as a function of droplet diameter for the compressed temperature of 910 K for diesel droplets injected into $CH_4/O_2/N_2/Ar$ mixtures of various equivalence ratios ($0 < \phi < 1.2$). As shown, the ignition delay of droplets increases with increasing droplet diameter for a given equivalence ratio. The results also indicate that the ignition delay increases with increasing CH4/O2/N2/Ar mixture equivalence ratio for a given droplet diameter. A similar phenomenon is observed in dual-fuel diesel/natural gas engines in which the start of combustion is retarded for dual-fuel engines in comparison to diesel engines [5][6].

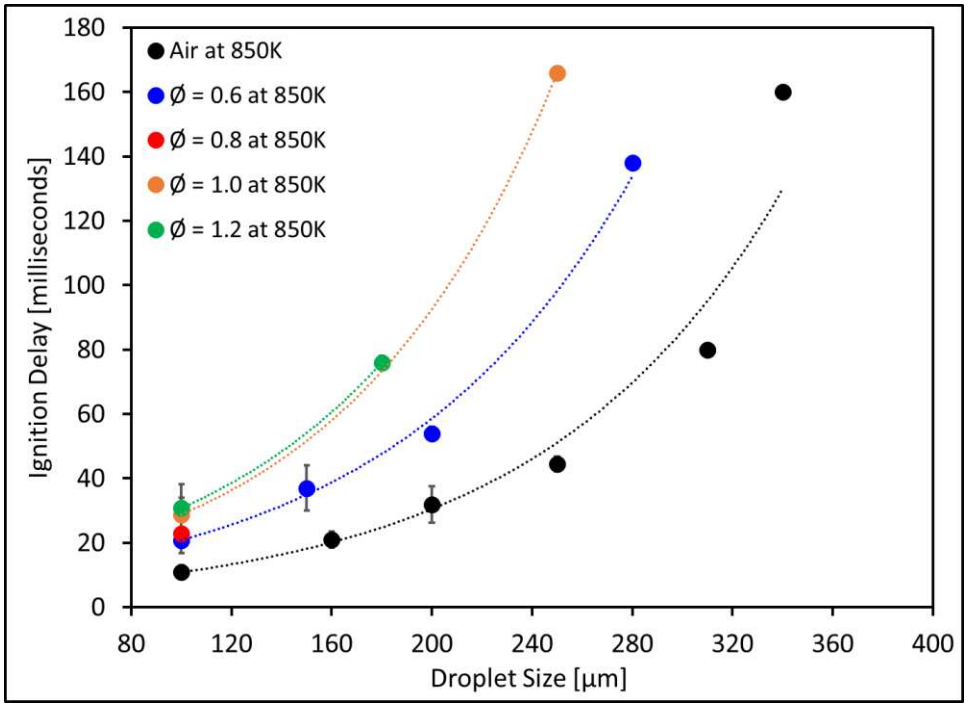

Figure 5.10. Ignition delay period as a function of initial droplet diameter for the compressed temperature of 850 K, respectively, for diesel droplets injected into $CH_4/O_2/N_2/Ar$ mixtures at an equivalence ratio of $0 < \phi < 1.2$.

For these experiments, the initial liquid droplet temperature was maintained at 299 K. Figure 5.11 is a plot of the ignition delay period as a function of droplet diameter for the compressed temperature of 850 K for diesel droplets injected into $CH_4/O_2/N_2/Ar$ mixtures of various equivalence ratio ($0 < \phi < 1.2$). As shown, for a given equivalence ratio, the ignition delay of droplets increases with increasing droplet diameter. The results also indicate that, for a given droplet diameter, the ignition delay increases with increasing $CH_4/O_2/N_2/Ar$ mixture equivalence ratio. Comparing Figure 5.10 and Figure 5.11, the ignition delay of the diesel droplets increases with a decrease in the far-field temperature at all equivalence ratios ($0 < \phi < 1.2$) and all droplet sizes.

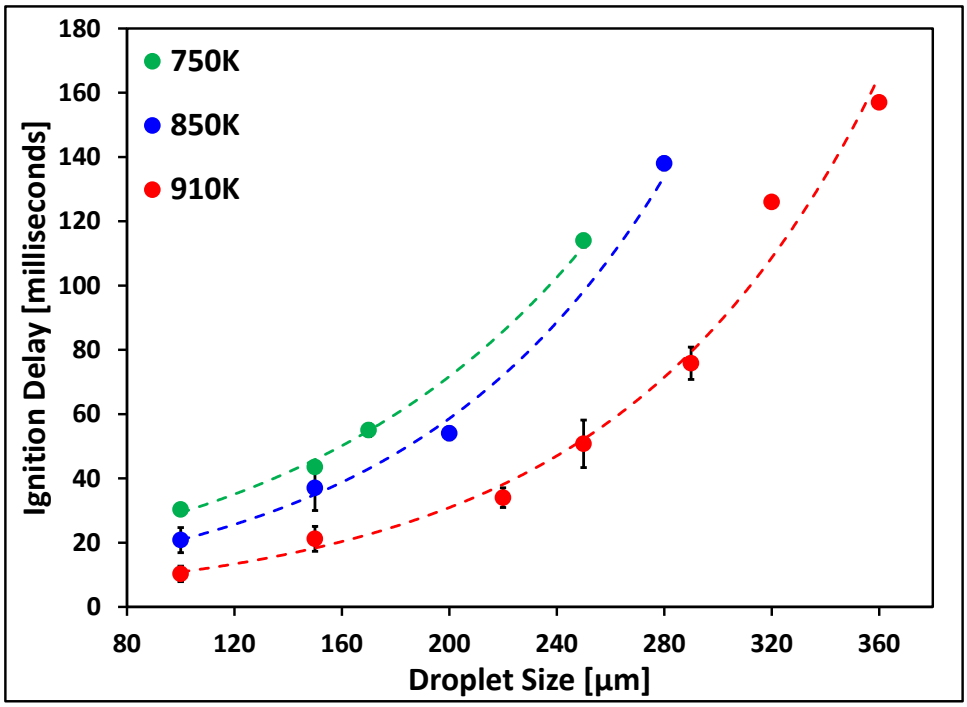

Figure 5.11. Ignition delay period as a function of initial droplet diameter for diesel droplets injected into lean $CH_4/O_2/N_2/Ar$ mixtures at $\phi = 0.6$ at compressed temperatures of 750 K, 850 K, and 910 K.

Figure 5.12 is a plot of the ignition delay period as a function of initial droplet diameter for diesel droplets injected into lean $CH_4/O_2/N_2/Ar$ mixtures at $\phi = 0.6$ at compressed temperatures of 750 K, 850 K, and 910 K. As shown, the ignition delay period increases with decreasing compressed temperature and droplet diameter. Experiments were also conducted at a compressed temperature of 700 K, and no droplet ignition was observed for any droplet diameter. At 700 K, the smaller droplets completely evaporate, and the residual diesel fuel diffuses into the mixture before ignition can occur. The larger droplets impact the RCM combustion chamber walls before ignition occurs. Carrying out this study, an ignition limit or threshold was observed. No diesel droplets auto-ignited at $\phi = 0.6$ and surrounding temperature of 700 K. This result is significant and indicates the parameters at which the dual-fuel engine can misfire. This study was extended to find the limit of droplet ignition at various thermodynamic conditions.

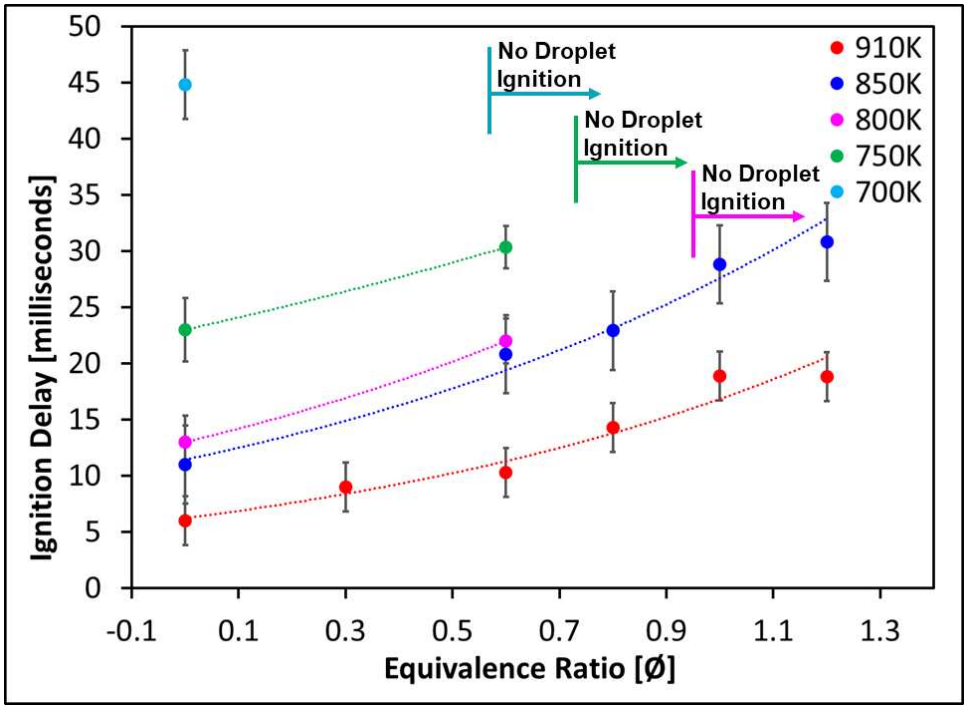

Figure 5.12. Ignition delay period for 100 µm diesel droplets in methane/air mixtures ($0 < \phi < 1.2$) and compressed temperatures from 700 K to 910 K.

These experiments were performed with 100 µm droplets over a range of $CH_4/O_2/N_2/Ar$ equivalence ratios ($0 < \phi < 1.2$) and compressed temperatures from 700 K to 910 K. As shown in Figure 5.13, the ignition delay of 100 µm diesel droplets increases with decreasing compressed temperature from 910 K to 700 K and increasing $CH_4/O_2/N_2/Ar$ equivalence ratio. Figure 5.13 also shows the temperature threshold below which the droplets completely evaporate and do not ignite. From 850 K to 910 K, ignition was observed for all equivalence ratios. At 800 K, droplet ignition was not observed for $\phi \geq 1$, at 750 K droplet ignition was not observed for $\phi \geq 0.8$, and at 700 K droplet ignition was not observed for $\phi \geq 0.6$. While similar results were found for larger droplets, droplets with diameters around 100 microns are more common to real engineering devices and thus of greater interest. The ability to generate representative droplet sizes at engine-like conditions without the use and associated inference of a droplet hanger allows for a holistic study of engineering devices.

When diesel droplets ignite in $CH_4/O_2/N_2/Ar$ mixtures, the non-premixed flame surrounding the diesel droplet can ignite a premixed propagating flame in the $CH_4/O_2/N_2/Ar$ mixture depending on the equivalence ratio of the mixture. In these experiments, premixed flame propagation in $CH_4/O_2/N_2/Ar$ mixtures was observed for equivalence ratios of $0.6 < \phi < 1.2$. At equivalence ratios of $0 < \phi < 0.3$, the droplets ignited but the $CH_4/O_2/N_2/Ar$ mixtures were too lean to support a propagating premixed flame.

5.4. Computational Modeling Results

5.4.1. Dual Fuel Droplet Ignition Simulation

The dual fuel droplet experiments were simulated with a combined analytical droplet evaporation model and a CFD model. The moving liquid droplet was modeled as a spherical fuel vapor source with surface vaporization rate and temperature determined using the transient analytical droplet evaporation model. Figure 5.14 shows the results of the three-dimensional CFD simulation of a single 150 μm liquid diesel droplet in high pressure and temperature $CH_4/O_2/N_2/Ar$ mixture at $\phi = 0.6$. The entire compression process of the RCM is simulated, along with the moving spherical droplet. A series of temperature contours at various times starting from BDC wherein the ambient temperature and pressure of the mixture are 303K and 1bar, respectively, are presented. TDC's compressed temperature and pressure are 812 K and 24 bar, respectively. Diesel was modeled as n-heptane as their chemical properties are similar with similar heating values. CSU 141 chemical kinetic mechanism was used in all the simulations.

Each frame of the computation shown in Figure 5.14 is marked with a letter from A through L, which is used for comparing the temperature contours to the pressure rise and heat release rates in the RCM in Figure 5.15 as predicted by the model. In frame A (t = 0 ms), the liquid droplet is

injected vertically from the bottom of the RCM at the centerline between the two pistons. The pistons reach TDC in frame C (t = 23ms) as the droplet continues in its vertical trajectory along the stagnation plane of the combustion chamber. It should be noted that the model results shown here are for symmetrical compression (piston time offset = 0 ms). At time t = 35 ms, as shown in frame D, the first evidence of heat release is observed near the droplet surface. At t = 44 ms, as indicated in frame E, the droplet vapor autoignites around the droplet and quickly results in a premixed flame propagating outward in the combustion domain consuming the $CH_4/O_2/N_2/Ar$ mixture, as shown in frame F. The droplet continues to move upward, leaving a vapor trail. At t = 100 ms, the droplet's downward trajectory begins. By this time, the premixed flame consumed all the $CH_4/O_2/N_2/Ar$ mixture in the domain, but, given the initial equivalence ratio $\phi = 0.6$, there is sufficient oxygen remaining to support a non-premixed flame near the droplet surface. Based on the analytical droplet vaporization model's predictions, the droplet was entirely evaporated by t = 110 ms and diesel evaporation rate at the droplet surface was set to zero for the rest of the computation.

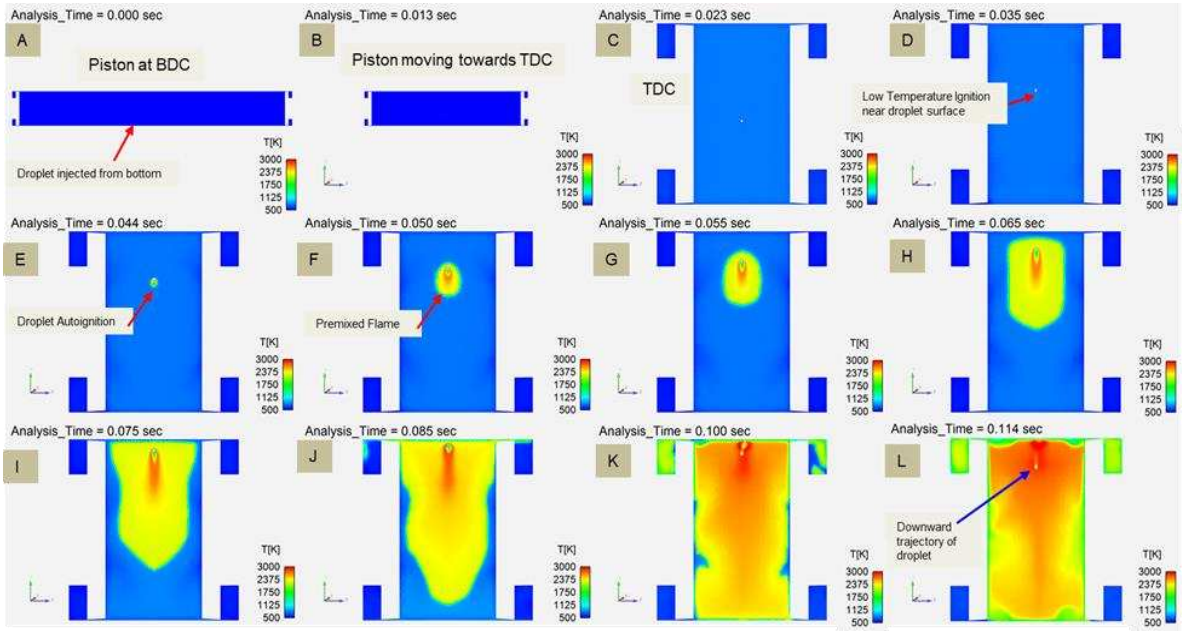

Figure 5.13. Temperature contours in the gas phase surrounding of a 450 μm n-heptane droplet in a $\phi = 0.6$ $CH_4/O_2/N_2/Ar$ mixture. The simulation includes compression of the RCM to compressed pressure and temperature of 24 bar and 812 K, injection of the droplet, ignition, and combustion.

Figure 5.15 contains plots of calculated pressure history and heat release rate from model results shown in Figure 5.14. Point A indicates the initial condition before RCM firing, with initial pressure and temperature of 1 bar and 300 K, respectively. Point C indicates the TDC position when RCM pistons are fully compressed, resulting in pressure and temperature of 27 bar and 812 K, respectively. Point E is where the droplet autoignites and produces a premixed flame. Consistent with experiments, the pressure curve stays relatively constant until point G, as the heat released by the premixed flame is counterbalanced by the heat loss from RCM walls. As flame continues to propagate after point G, the heat release from combustion dominates, and the pressure increases (t = 55 ms). The heat release plot shown in Figure 1.15 confirms the position of the positive pressure slope as the heat release rate becomes positive at this time. After point G, the pressure increases as the premixed flame propagates until a peak pressure of 72 bar is reached at approximately 114 ms. Consistent with experiments, no end-gas autoignition was observed upstream of the propagating $CH_4/O_2/N_2/Ar$ flames.

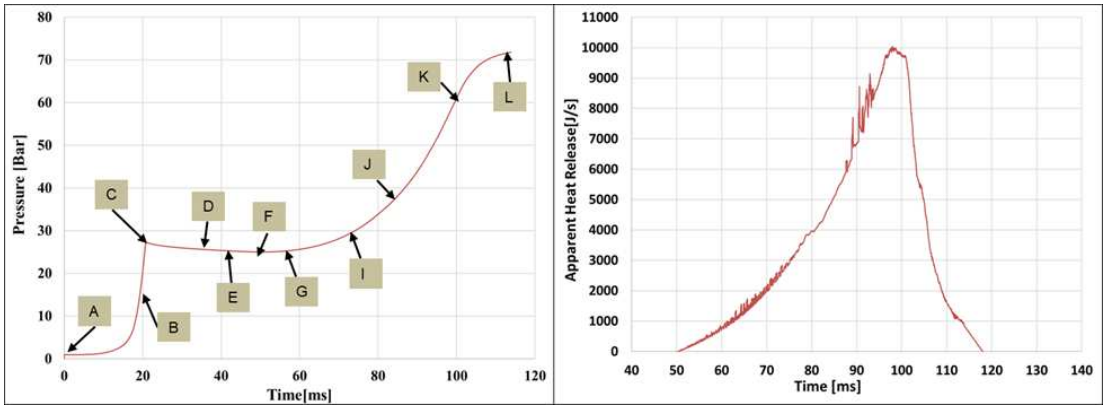

Figure 5.14. Calculated pressure and heat release rate from simulation results for a 150 μm diesel droplet in $CH_4/O_2/N_2/Ar$ mixture of $\phi = 0.6$ for the conditions shown in Fig. 5.14.

5.4.2. *Effect of Farfield Temperature on Ignition Delay*

CFD modeling of diesel droplets was conducted for replicating the experimental ignition delay results observed at various conditions of far-field temperatures $700K < T_c < 950K$ at various equivalence ratios of $0 < \phi < 1.2$ for various droplet sizes range ($100\mu m < d_o < 300\mu m$) at a constant TDC pressure of 24 bar.

Figure 5.16 is a plot of the ignition delay period of 250 μm diesel droplet at various conditions of far-field temperature ranging from 800 K to 930 K. The liquid temperature of the diesel droplet used is 299 K. O_2/N_2/Ar mixture was used as the gaseous medium. As shown, for a given droplet size, the ignition delay period of diesel droplets increases with a decrease in the far-field temperature. Simulation results agree with the experimental dataset and predict the ignition delay period very close to the experimental observation.

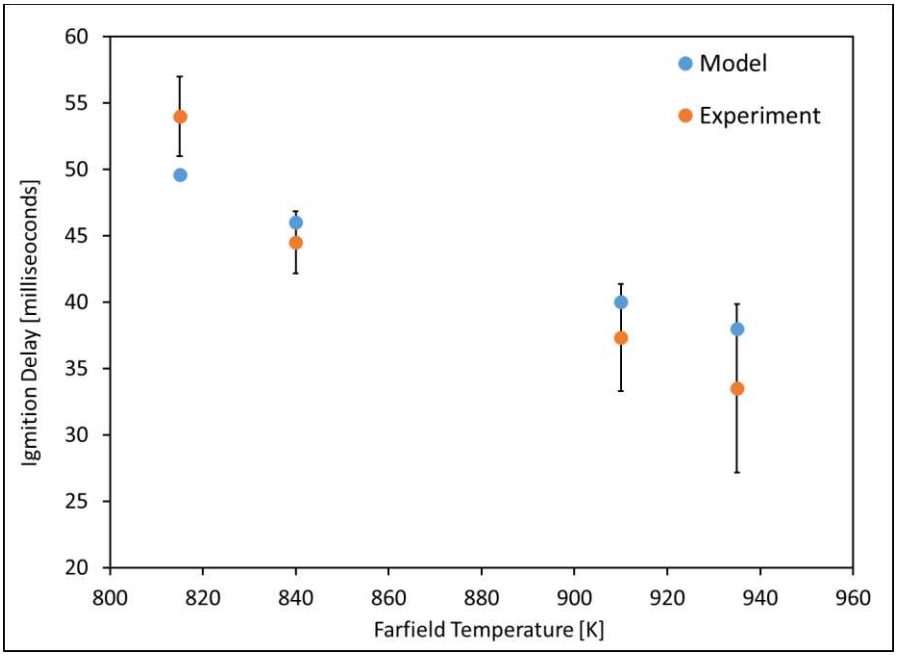

Figure 5.15. Ignition delay period as a function of far-field temperature for 250 μm diesel droplet in O_2/N_2/Ar mixture at a constant pressure of 24 bar.

5.4.3. *Effect of Droplet Temperature on Ignition Delay Period*

Figure 5.17 is a plot of the ignition delay period of 250 µm diesel droplet for various liquid droplet temperatures ranging from 800 K to 930 K. The far-field temperature for the gaseous medium is 910 K. O_2/N_2/Ar mixture was used as the gaseous medium. As shown, for given droplet size, the ignition delay period of diesel droplets increases with a decrease in the initial liquid droplet temperature. Simulation results agree with the experimental dataset and predict the ignition delay period fairly close to the experimental observation. Simulations were also conducted at higher temperatures which shows that the ignition delay period starts decreasing with a higher slope after 180°C droplet temperature, which indicates that the droplet ignition enters a regime where the droplet evaporation rate goes adequately higher, creating adequate vapor around the droplet in a shorter time interval resulting in a shorter ignition delay periods for the heated diesel droplets above 180°C.

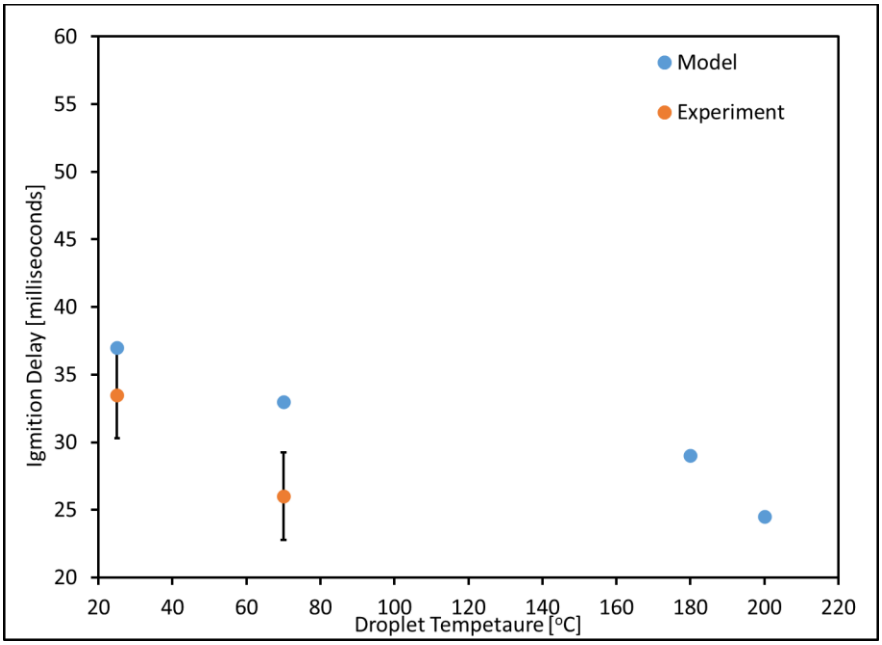

Figure 5.16. Simulated and Experimental ignition delay period as a function of initial liquid droplet temperature for 250 µm diesel droplet in O2/N2/Ar mixture at a constant pressure of 24 bar and constant far-field temperature of 910 K.

5.4.4. Effect of Droplet Size on Ignition Delay Period

Figure 5.18 is a plot of the ignition delay period for varied droplet sizes of 100µm < d_o < 300µm subjected to a compressed pressure of 24 bar and a compressed temperature of 910 K. The liquid droplet temperature was 299 K. O2/N2/Ar mixture as the gaseous medium. As shown, the diesel droplet's ignition delay period increases with the droplet diameter increase. The simulation results show a consistent trend of ignition delay period as compared to the experiments. Simulations predict the ignition delay period very closely for all the droplet sizes compared to the experiments.

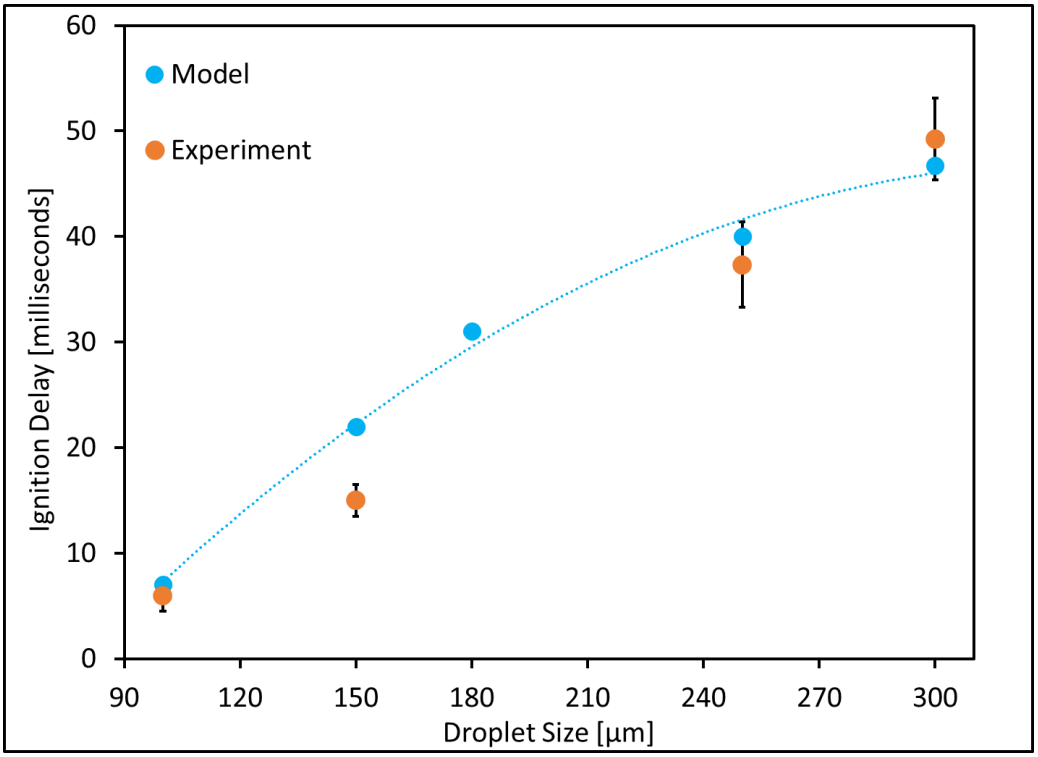

Figure 5.17. Simulated and Experimental ignition delay period as a function of diesel droplet size at an initial temperature of 299K in O2/N2/Ar mixture at a constant pressure of 24 bar and constant far-field temperature of 910 K.

5.4.5. Effect of Far-field Equivalence Ratio on Ignition Delay Period

Figure 5.19 plots the ignition delay period for varied droplet sizes ranging from 100 µm to 300 µm subjected to a compressed pressure of 24 bar and a compressed temperature of 910 K. The droplet sizes were also subjected to different far-field equivalence ratios ranging from $0 < \phi < 1$. The liquid droplet temperature for these simulations and experiments was 299 K. As shown, the diesel droplet's ignition delay period increases with the droplet diameter increase for all the equivalence ratios. Also, the diesel droplet's ignition delay period increases with the far-field equivalence ratios for all droplet sizes. The CFD simulations capture the observed trend of increased ignition delay with increasing droplet diameter and equivalence ratio. Moreover, the CFD simulations accurately reproduce the measured ignition delay at smaller droplet diameters ($do \leq 200$ µm) for all ϕ. For droplet diameters > 250 µm, the predicted ignition delay period of the CFD model deviates from experimental observations, which could be associated with the CFD modeling limitation that underpredicts the heat loss to the RCM walls resulting in higher gaseous temperature causing the droplet to ignite earlier.

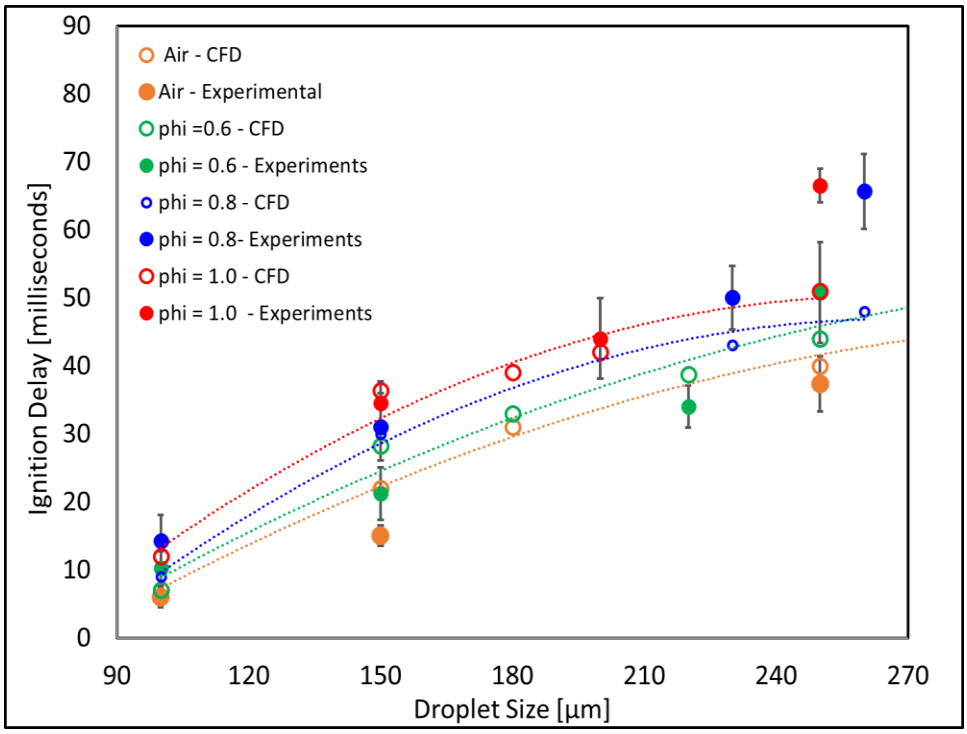

Figure 5.18. Measured and simulated ignition delay period for diesel droplets (100 µm < d_o < 250 µm) injected into $CH_4/O_2/N_2/Ar$ mixtures (0 < ϕ < 1.2) at compressed temperature and pressure of 910 K and 24 bar, respectively.

5.4.6. Multiple modes of Dual Fuel Droplet Ignition/Combustion

Multiple dual-fuel droplet ignition/combustion modes were identified in this study. These modes, which are shown in Figure 5.20, are dependent on droplet size, droplet velocity, droplet temperature (i.e., volatility), equivalence ratio of the gas mixture, and compressed temperature. For smaller diesel droplet diameters (100 µm to 150 µm), the droplet heating period is minimal, resulting in a high droplet vaporization rate and a high vapor concentration in the vicinity of the droplet as it reaches its apex position. In addition, the Stephan flow velocity near the droplet surface is higher for smaller droplets producing a spherically symmetric vapor distribution in the vicinity of the droplet, which results in a spherical ignition event that ignites a spherical, outwardly propagating premixed $CH_4/O_2/N_2/Ar$ flame as shown in Figure 5.20(A). For droplets of larger diameter (> 150 µm), the vaporization rate is initially lower due to a longer droplet heating period,

which in combination with the lower Stephan flow velocity, results in the droplet leaving a vapor trail in the wake of the droplet as shown in Figure 5.20(B). In this mode, ignition first occurs in the vapor trail behind the droplet, which produces a non-premixed flame that envelopes the droplet and an asymmetric premixed flame that propagates toward the vapor trail. A third combustion/ignition mode was observed for heated diesel droplets ($T_{droplet}$ = 343 K) traveling at higher velocities. In this mode, the increased evaporation rate due to higher vapor concentrations at the droplet surface and higher convective mass transfer due to higher droplet velocity create a long, high concentration vapor trail behind the droplet. The vapor left by the moving droplet ignites far from the droplet surface within the vapor tail and produces a premixed flame that propagates back toward the moving droplet, as seen in Figure 5.20(C).

The different combustion modes observed generally depend on the velocity, initial droplet temperature, and droplet diameter. A spherical ignition followed by spherical flame propagation, as shown in Figure 5.20(A), is observed with smaller droplet sizes of 100 to 150 µm falling under gravity. Ignition in the trailing edge of the droplet with asymmetric flame propagation, as shown in Figure 5.20(B), is observed with larger droplets (> 150 µm) falling under gravity. The third mode is the ignition along the droplet trail, as shown in Figure 5.20(C), which is observed for heated diesel droplets (343 K) moving with a velocity > 1.5 m/s. CFD model also qualitatively captures the variety of ignition/combustion modes observed experimentally for diesel droplet combustion in $CH_4/O_2/N_2$/Ar mixtures as a function of droplet diameter and initial liquid temperature.

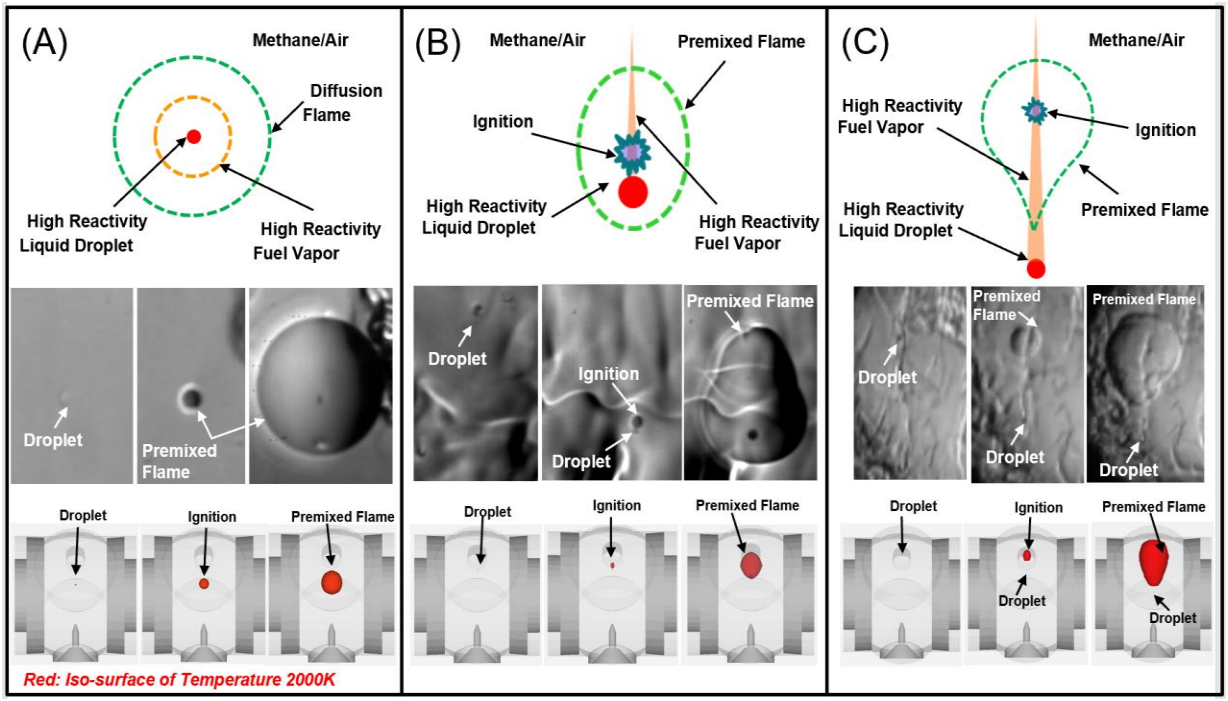

Figure 5.19. Multiple modes of dual fuel droplet ignition/combustion observed for diesel droplet combustion in $CH_4/O_2/N_2/Ar$ mixtures as a function of droplet diameter, temperature, and velocity. (A) spherical ignition followed by spherical outwardly propagating flame for 100 µm droplet at a liquid temperature of 299 K, (B) ignition in the trailing edge of the droplet with asymmetric flame propagation for 360 µm droplet at a liquid temperature of 299 K, and (C) ignition far behind the droplet with flame propagation back toward the droplet for 100 µm droplet at a liquid temperature of 343 K.

Figure 5.21 illustrates the influence of the equivalence ratio of the $CH_4/O_2/N_2/Ar$ gas mixture on the premixed flame propagation behavior. As shown in Fig. 5.21(A), for a lean mixture with a $CH_4/O_2/N_2/Ar$ equivalence ratio of 0.6, the premixed flame initially develops as a spherical flame and then becomes asymmetrical because the local flame speed is faster in the vicinity of the diesel vapor trail, which is locally closer to stoichiometric than the balance of the flow field. However, for stoichiometric $CH_4/O_2/N_2/Ar$ mixtures, as shown in Fig. 5.21(B), the spherically symmetric droplet ignition event produces a spherically symmetric outwardly propagating flame. The spherical nature of the flame at stoichiometric far-field conditions is a consequence of the local flame speed remaining nearly constant along the flame front in the vicinity of the slightly rich

mixtures of methane/vaporized diesel fuel/O_2/N_2/Ar ($\phi \approx 1.2$). CFD model also qualitatively captures the variety of ignition/combustion modes observed experimentally for diesel droplet combustion in CH_4/O_2/N_2/Ar mixtures as a function of the stoichiometry of the CH_4/O_2/N_2/Ar mixture.

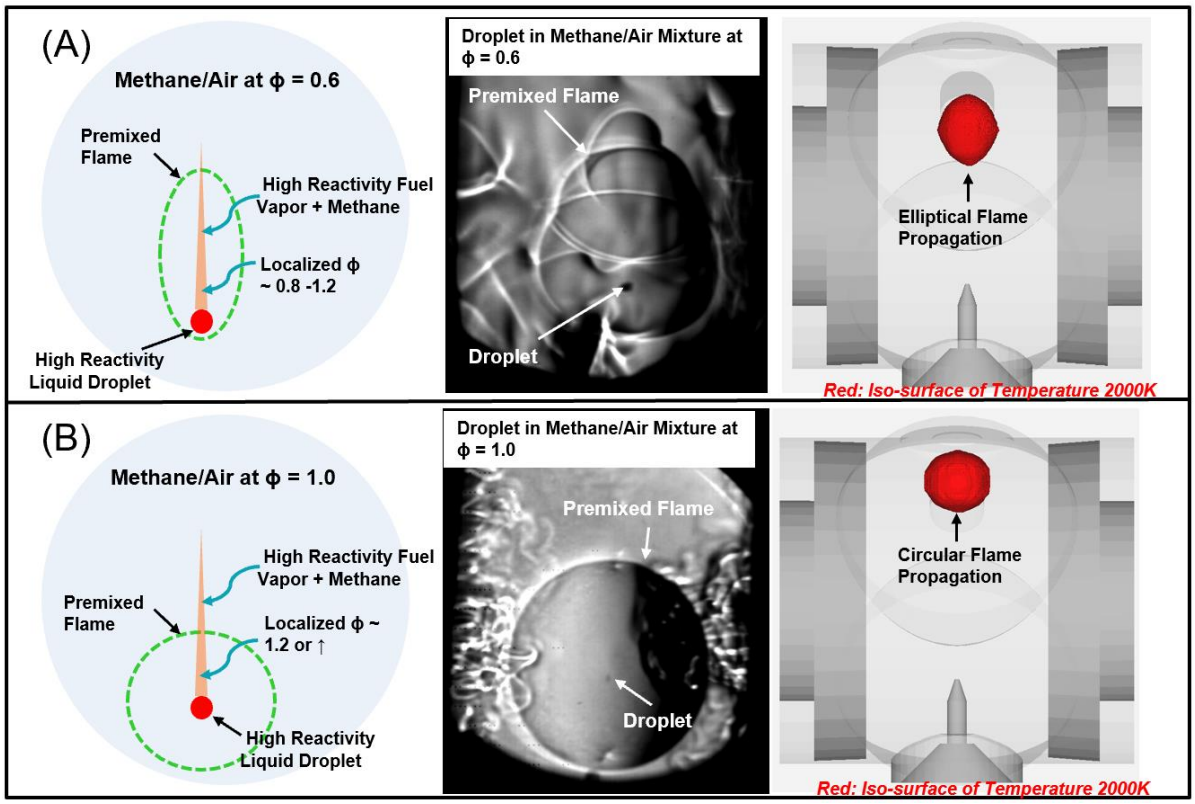

Figure 5.20. Different modes of premixed flame propagation with schematics (left), experimental observations (center) and CFD simulation results (right) in (A) lean methane/air mixture of $\phi = 0.6$ and (B) stoichiometric CH_4/O_2/N_2/Ar mixture of $\phi = 1.0$.

CFD simulations were also performed at lower compressed temperatures of 750 K and for CH_4/O_2/N_2/Ar mixture equivalence ratios of $0.6 < \phi < 1.2$. At these conditions, the simulations did not predict any autoignition or flame propagation, which is consistent with the experimental observations shown in Figure 5.13.

5.5. Conclusion

The results of this study demonstrate the capability of the opposed-piston RCM configuration integrated with a piezoelectric droplet generator to inject single isolated hydrocarbon fuel droplets into fuel/air mixtures at elevated pressure and temperature conditions. Experiments conducted with this system demonstrate how droplet vaporization, ignition, and dual fuel flame propagation vary with droplet diameter, initial droplet temperature, droplet volatility, gas temperature, and chemical reactivity of the liquid and gaseous fuels.

Experiments were conducted with diesel droplets of varying sizes at various temperatures injected into $CH_4/O_2/N_2/Ar$ mixtures at temperatures of 700 K to 910 K and equivalence ratios of $0 < \phi < 1.2$. These experiments revealed multiple modes of droplet ignition, droplet combustion, and premixed flame propagation, which depend on the initial droplet temperature, droplet diameter, droplet velocity, and stoichiometry of the $CH_4/O_2/N_2/Ar$ mixture. For small droplets, spherical ignition events were observed that transition into spherical non-premixed flames that envelope the droplet. These spherical non-premixed flames produce outwardly propagating spherical premixed flames. For larger droplet diameters moving at moderate velocity, the ignition event occurs near the droplet surface on the leeward side of the droplet and subsequently creates a non-premixed flame that envelopes the droplet and a non-spherical premixed flame. For droplets moving with high velocities, the ignition event occurs in the wake of the droplet, multiple diameters from the droplet surface, and creates a flame that propagates toward the droplet. Spherical, outwardly propagating premixed flames were observed for diesel droplet ignition in stoichiometric $CH_4/O_2/N_2/Ar$ mixtures, whereas elongated premixed flames were observed in lean $CH_4/O_2/N_2/Ar$ mixtures.

The results of this combined experimental and modeling approach strongly suggest that ignition and combustion of liquid droplets of high chemical reactivity (e.g., diesel) in gaseous fuel/air mixtures of lower reactivity (e.g., $CH_4/O_2/N_2/Ar$) represents a robust system for elucidating the underlying combustion phenomena of dual fuel combustion. Moreover, the experiments have also produced a valuable data set that can be used to validate chemical kinetic mechanisms for dual fuel combustion under engine-relevant conditions.

CHAPTER 6: DUAL EXPERIMENAL STUDY OF UNDERSTANDING ABNORMAL COMBUSTION TRIGGERED BY LUBRICANT OIL DROPLETS

6.1. Introduction

This work is motivated by abnormal combustion observed in spark-ignited, highly boosted natural gas engines, which damages engine components due to rapid pressure rise in the engine cylinder. The mechanism leading to abnormal combustion in natural gas engines is not entirely understood despite several studies performed by engine manufacturers and research institutions [12][13][14]. Studies have previously focused on the influence of spark plug configuration, lubricant oil entering the combustion chamber, and engine hot spots. Inoue et al. [15] studied the effect of spark plug characteristics on abnormal combustion phenomena. They concluded that the spark plug ground electrode length, center electrode diameter, spark plug heat range, the orientation of the ground electrode, and spark gap had a minimum influence on abnormal combustion. Studies have also been conducted to understand the effect of lubricant oil composition on the occurrence of abnormal combustion events [16][17][18][19][20] and concluded that the presence of zinc, calcium, and molybdenum in lubricant oil increase the propensity of abnormal combustion events. Willand et al. [18] performed an experimental and numerical investigation on these abnormal combustion events and concluded that residual gas, lubricant oil droplets, hot spots, deposits, and the fuel-air autoignition mixture are all potential causes of pre-ignition.

The previous studies show the potential causes for abnormal combustion events caused by lubricant oil droplets, but the exact mechanism of these events is still unclear and requires additional work in a controlled environment under engine-relevant conditions. For example, if oil droplet ignition triggers the combustion of the fuel/air mixture, there is a need to quantify the thermodynamic conditions (pressure, temperature, equivalence ratio) under which such droplet

ignition occurs. In engine studies, it is challenging to determine the local conditions under which such events occur, given the complex fluid mechanics, temperature and composition stratification, and cycle-to-cycle pressure variation.

In parallel to experimental studies, CFD models of engines have been developed to investigate the abnormal combustion events caused by lubricant oil droplets [30][31] in natural gas engines. These CFD studies revealed the complex interaction between the turbulent flow field, the evaporation of the lubricant oil droplet, and combustion characteristics of the evaporated lubricant oil droplet in a stratified natural gas/air mixture on the occurrence of the abnormal combustion event. These studies emphasized the need to perform fundamental studies of isolated droplet combustion in natural gas/air mixtures to better understand the abnormal combustion phenomenon.

6.2. Lubricant Oils Properties

Four different lubricant oils were considered for testing their evaporation and ignition characteristics. One of the oils was petroleum-based oil, and the other four oils were ester-based oils. The base stock for all the oils is similar and are giving different additives which change the ignition and combustion behavior of the four lubricant oils. The lubricant oils are the confidential property of Caterpillar Inc., and hence the composition of these oils are not mentioned in detail in this dissertation. Lubricant oils are named as PBO1 oil (Petroleum Based), EBO1, EBO2, EBO3 and EBO4 oils (Ester Based).

The physical properties of these oils are tabulated in Table 6.1. The properties of EBO2 oils are not mentioned. It is assumed that its properties are similar to other ester-based oils with similar boiling points and vapor densities.

Table 6.1. Physical Properties of the petroleum-based lubricant oil and three ester-based lubricant oils, namely (a) PBO1, (b) EBO2, (c) EBO3, and (d) EBO4 oils.

Flash Point, °C	220
Boiling Point, °C	> 288
Vapor Density, kPa	> 2 at 101 kPa
Vapor Pressure, kPa	< 0.013 kPa at 20 °C
Porpoint, °C	-12
Solubility in Water	Negligible

(a)

Flash Point, °C	250
Boiling Point, °C	> 300
Vapor Density, kPa	> 2 at 101 kPa
Vapor Pressure, kPa	< 0.013 kPa at 20 °C
Porpoint, °C	-30
Solubility in Water	Negligible

(b)

Flash Point, °C	240
Boiling Point, °C	> 316
Vapor Density, kPa	> 2 at 101 kPa
Vapor Pressure, kPa	< 0.013 kPa at 20 °C
Porpoint, °C	-1
Solubility in Water	Negligible

(c)

Flash Point, °C	250
Boiling Point, °C	> 300
Vapor Density, kPa	> 2 at 101 kPa
Vapor Pressure, kPa	< 0.013 kPa at 20 °C
Porpoint, °C	-30
Solubility in Water	Negligible

(d)

As shown in Table 6.1, all the oils have similar physical properties with some distinction in the boiling point of the oils. The boiling point of PBO1 oil is the lowest and highest for EBO3 oil. The lower boiling point observed with PBO1 oil indicates that PBO1 oil droplets will exhibit a faster evaporation rate when subjected to high-temperature conditions and can result in a lower ignition delay period compared to the ester-based oils, which have a comparatively higher boiling point.

6.3. Experimental Conditions

Four lubricant oils were tested in the RCM to quantify the ignition delay periods of the lubricant oil droplets for various sizes ranging from 50 μm < d_0 < 500 μm at different compressed temperatures of 700 K < T_c < 1000 K and at a constant pressure of 24 bar. The far-field methane/air equivalence ratio was also varied from 0 < ϕ < 1.2 to see the effect of the equivalence ratio on the ignition properties of the lubricant oils. The lubricant oils are highly viscous with viscosity > 200 cSt at room temperature. Due to high viscosity, droplet formation at room temperature using the current setup was not possible. To address this, the lubricant oils were heated to 90 ^{0}C in the droplet generator using cartridge heaters provided in the fuel passage sleeve. The heating of the lubricant oil results in a viscosity reduction by a significant amount but still higher than certification diesel's viscosity. This allows the lubricant oil to flow readily in the droplet generator and to create various size droplets. A square wave of 95V and pulse width of 2 ms created multiple isolated lubricant oil droplets in the RCM chamber.

Experiments with the lubricant oil droplets at various thermodynamic and mixture conditions will provide a valuable dataset of ignition delay periods which will be used in developing a

chemical kinetic mechanism scheme. This mechanism will then be used in developing CFD models of different lubricant oils to enhance our understanding of lubricant oil-triggered abnormal combustion observed in natural gas engines. These experiments will also provide details of various thermodynamic and fluid dynamic thresholds at which the lubricant oils combustion will not result in a premixed flame in the methane/air mixture. The effect of the methane/air equivalence ratio on the flammability limit of lubricant oil droplets can also be investigated using the experimental setup.

6.4. Experimental Results

6.4.1. Ignition Characteristics of Petroleum-Based Oil (PBO1)

An experimental investigation of abnormal combustion triggered by lubricant oil droplets was initiated with petroleum-based PBO1 oil. Due to its lower boiling point, the rate of evaporation of the PBO1 oil was found to be higher and resulted in comparatively lower ignition delay periods. Experiments were conducted for PBO1 oil droplets of sizes $50\mu m < d_0 < 500\mu m$ at different compressed temperatures of $700K < T_c < 1000K$ at a constant pressure of 24 bar. The far-field methane/air equivalence ratio was also varied from $0 < \phi < 1.2$ to see the effect of the equivalence ratio on the ignition properties of PBO1 oils.

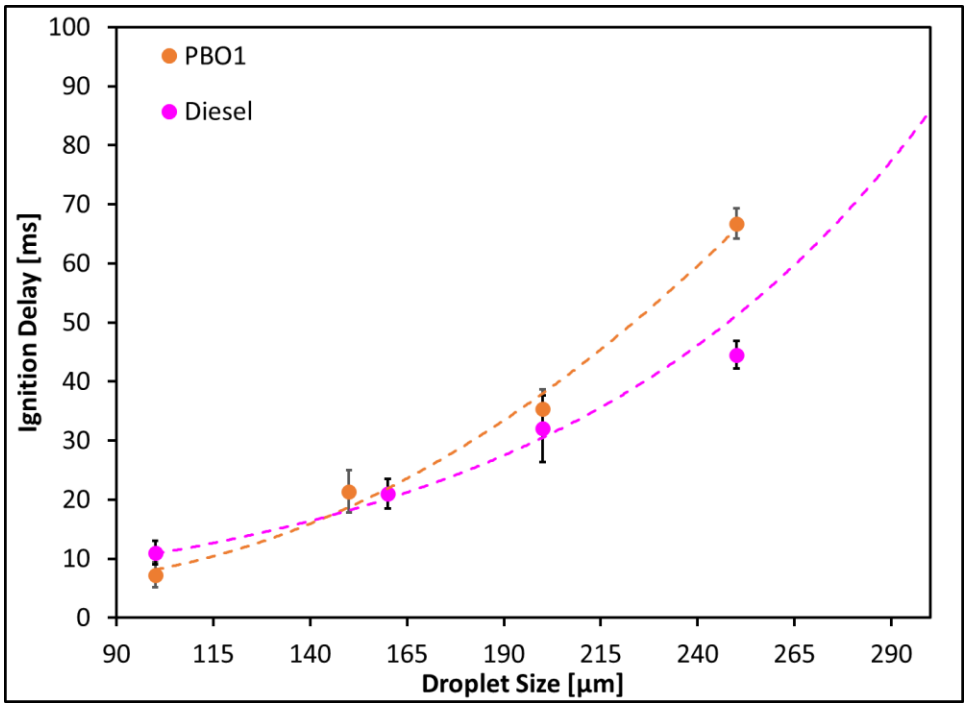

Figure 6.1. Comparison of ignition delay of PBO1 lubricant oil droplets at a liquid temperature of 363 K and diesel droplets at a liquid temperature of 300 K in O_2/inert mixtures at compressed temperature and pressure of 900 K and 24 bar, respectively.

Figure 6.1 is a plot of the ignition delay period of petroleum-based lubricant oil droplets of sizes 100µm < d_o < 250µm in comparison to the diesel droplets injected in O_2/inert mixtures at a compressed pressure of 24 bar and a compressed temperature of 900 K. An increase in the ignition delay period was observed as the droplet size increases. The ignition delay period of PBO1 oil was comparable to diesel droplets at smaller sizes up to 150 µm, but then for the bigger droplet sizes, the ignition delay period was found to be marginally higher compared to the diesel droplets.

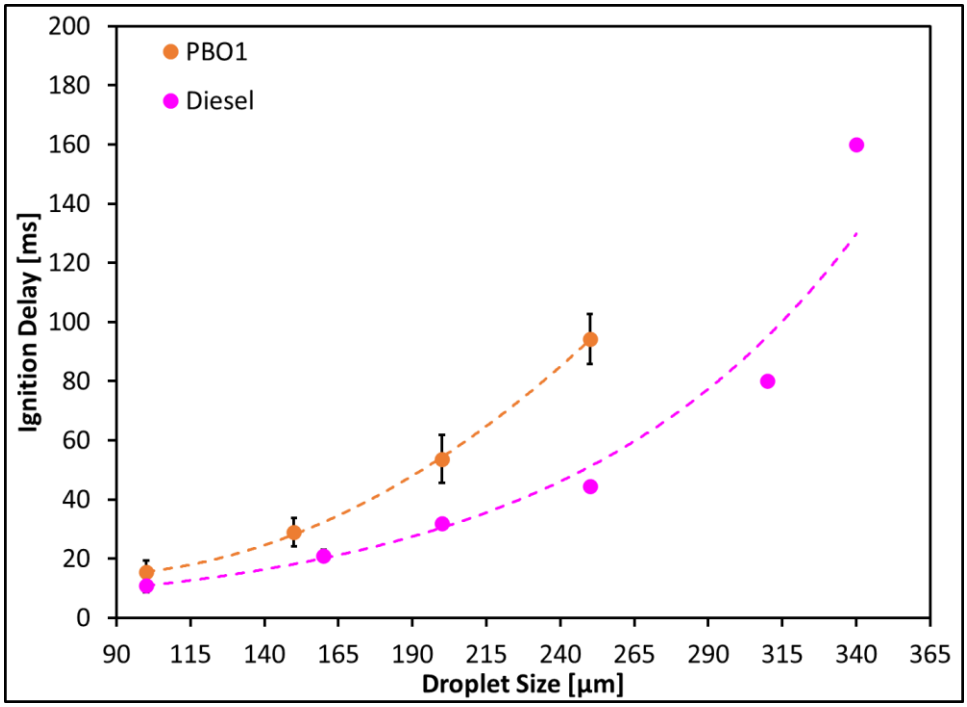

Figure 6.2. Comparison of ignition delay of PBO1 lubricant oil droplets at a liquid temperature of 363 K and diesel droplets at a liquid temperature of 300 K in O_2/inert mixtures at compressed temperature and pressure of 850 K and 24 bar, respectively.

Figure 6.2 is a plot of the ignition delay period of petroleum-based lubricant oil droplets of sizes 100 µm < d_o < 350 µm in comparison to the diesel droplets injected in O_2/inert mixtures at a compressed pressure of 24 bar and a compressed temperature of 850 K. An increase in the ignition delay period was observed as the droplet size increases. The ignition delay period of PBO1 oil was found to be higher as compared to the diesel droplets at all the droplet sizes ranging from 100 µm to 350 µm.

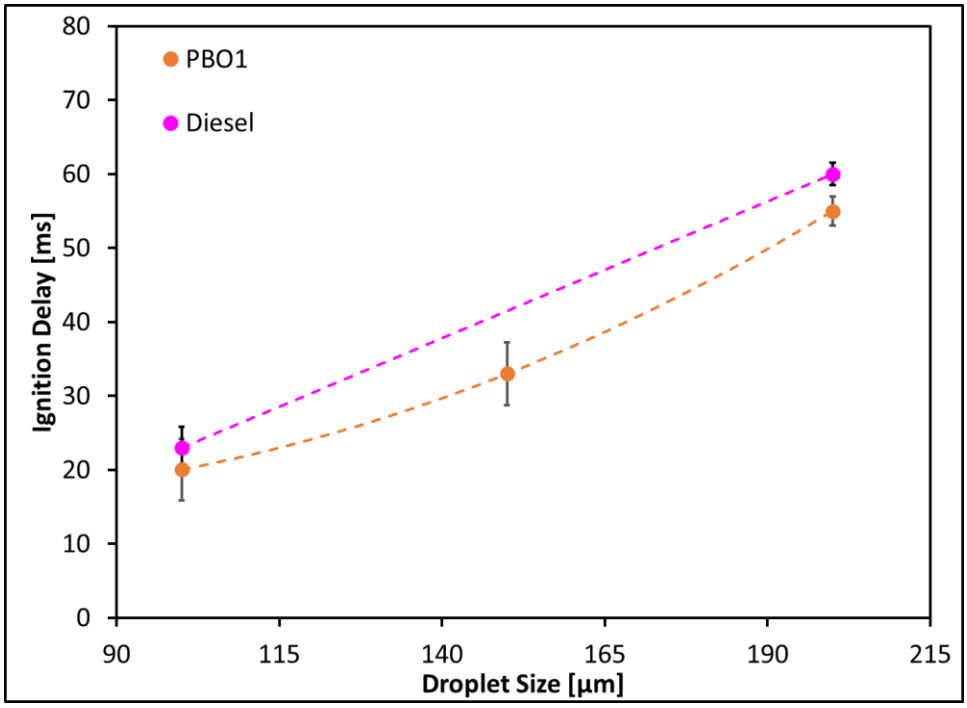

Figure 6.3. Comparison of ignition delay of PBO1 lubricant oil droplets at a liquid temperature of 363 K and diesel droplets at a liquid temperature of 300 K in O_2/inert mixtures at compressed temperature and pressure of 750 K and 24 bar, respectively.

Figure 6.3 is a plot of the ignition delay period of PBO1 oil droplets of sizes 100 µm < d_o < 200 µm in comparison to the diesel droplets injected in O_2/inert mixtures at a compressed pressure of 24 bar and a compressed temperature of 750 K. An increase in the ignition delay period was observed as the droplet size increases. The ignition delay period of PBO1 oil was found to be marginally lower as compared to the diesel droplets at all the droplet sizes ranging from 100 µm to 200 µm at a compressed temperature of 750 K. Comparing Figure 6.1, Figure 6.2 and Figure 6.3, an observed increase in ignition delay period is seen with a decrease in the compressed temperature for all the droplet sizes.

After investigating the ignition delay period of PBO1 oil in an O_2/inert mixture, experiments were conducted to study the ignition characteristics of the PBO1 droplets in lean methane/air mixtures of equivalence ratio $\phi = 0.6$.

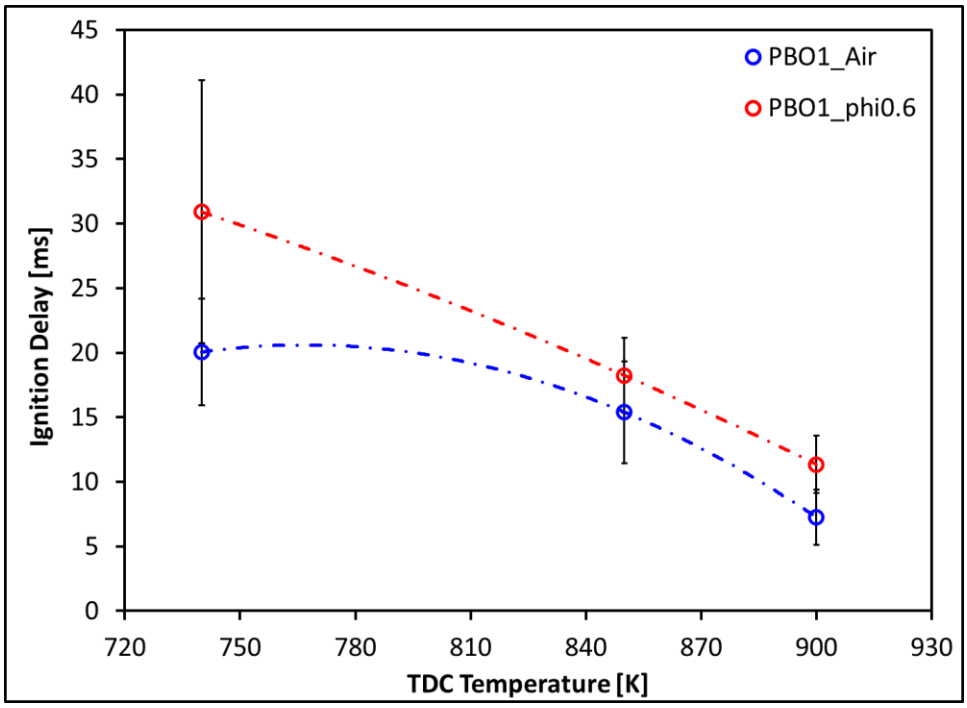

Figure 6.4. Comparison of ignition delay of PBO1 lubricant oil droplets of size 100 µm at a liquid temperature of 363 K in CH_4/O_2/inert mixture at an equivalence ratio of $\phi = 0.6$ and in O_2/inert mixtures at compressed temperatures of 750 K < T_c < 900 K and pressure of 24 bar.

Figure 6.4 is a plot of the ignition delay period of a PBO1 oil droplet of size 100 µm in CH_4/O_2/inert mixture at an equivalence ratio of $\phi = 0.6$ and in O_2/inert mixtures at compressed temperatures of 750 K < T_c < 900 K and compressed pressure of 24 bar. As shown, an increase in the ignition delay period was observed with a decrease in the compressed temperature. An increase in the ignition delay period was also observed with the addition of CH_4 in O_2/Inert mixtures, i.e., at $\phi = 0.6$. At a lower compressed temperature of 750 K, an increased uncertainty was observed in quantifying the ignition delay period of the droplet in a lean CH_4/O_2/inert mixture of $\phi = 0.6$. However, for all the experiments of injecting the PBO1 droplets in CH_4/O_2/inert mixtures at an equivalence ratio of $\phi = 0.6$, the ignition of the droplets resulted in a stationary diffusion flame around the droplet, which ignited the propagating premixed flame in CH_4/O_2/inert mixture.

To further understand the effect of CH_4 addition to O_2/inert mixture on the ignition delay period of PBO1 oil, a set of experiments was conducted at a constant compressed temperature of 750 K and compressed pressure of 24 bar with 100 μm PBO1 droplets. The farfield CH_4/O_2/inert mixture's equivalence ratio varied from $0 < \phi < 1.2$.

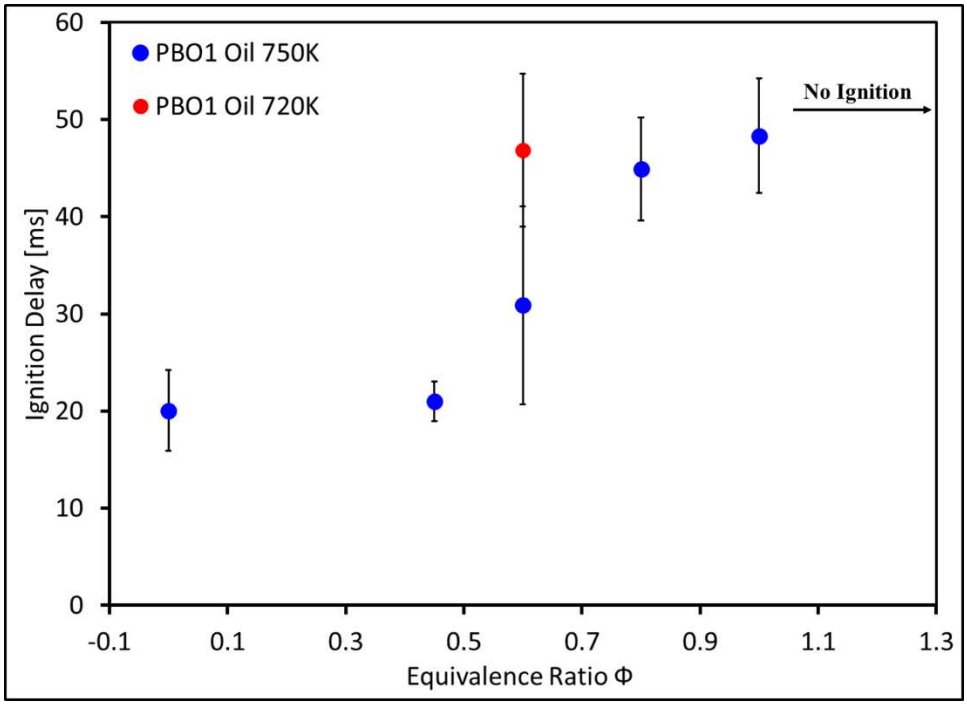

Figure 6.5. Comparison of ignition delay of PBO1 lubricant oil droplets of size 100 μm at a liquid temperature of 363 K in CH_4/O_2/inert mixture at a varied equivalence ratio of $0 < \phi < 1.2$ at compressed temperatures of 750 K and pressure of 24 bar.

Figure 6.5 is a plot of the ignition delay period of petroleum-based lubricant oil droplets of size 100 μm in CH_4/O_2/inert mixture at a varied equivalence ratio of $0 < \phi < 1.2$ at compressed temperatures of 750 K and pressure of 24 bar. As shown, the ignition delay period for PBO1 oil remained similar at a lower equivalence ratio ranging from $0 < \phi < 0.3$. With a further increase in the CH_4/O_2/inert mixture equivalence ratio, the ignition delay period of PBO1 oil increases dramatically, as observed around $0.45 < \phi < 1.0$. Various regime of combustion was observed for this set of experiments. At a lower equivalence ratio of $0 < \phi < 0.3$, the droplet ignition results in

a diffusion flame around the droplet but was not able to propagate the premixed flame in the CH_4/O_2/inert mixture, indicating that the lower flammability limit of the mixture at which a droplet ignition as a source cannot propagate a premixed flame in methane/air mixture. At an equivalence ratio of $0.6 < \phi < 0.8$, the diffusion flame which establishes around the droplet after droplet ignition results in a premixed flame that propagates in a CH_4/O_2/inert mixture. At an equivalence ratio of $\phi = 1.0$, the ignition of the droplets resulted in a premixed flame in CH_4/O_2/inert mixture but not for all cases. Nearly 40 % of the experimental cases showed that the PBO1 droplets only evaporated and did not ignite. This result indicates that the PBO1 oil droplets could not propagate premixed flame in CH_4/O_2/inert mixture, resulting in an inconsistent ignition event of PBO1 oil droplets. This threshold was confirmed by performing additional experiments at an equivalence ratio of $\phi = 1.2$, which showed no ignition of PBO1 oil droplets. These experiments provided a valuable dataset of the ignition delay period of PBO1 oil and provided details about various regimes of droplet ignition and premixed flame propagation in CH_4/O_2/inert mixtures. Studying the behavior of PBO1 oil droplets at various thermodynamic and mixture conditions, it can be concluded that for an abnormal combustion event to be triggered by lubricant oil droplets, various thermodynamic and mixture conditions are required to be satisfied. It was observed from the experiments that a quiescent domain with CH_4/O_2/inert mixture equivalence ratio of $0.6 < \phi < 0.8$ in the far-field at a high temperature of $750\ K < T_c < 900\ K$ are suitable conditions for causing abnormal combustion by PBO1 droplets in CH_4/O_2/inert mixtures.

6.4.2. Ignition Characteristics of Ester-Based Oil, EBO2

An experimental investigation of abnormal combustion triggered by ester-based lubricant oil droplets was initiated with EBO2 lubricant oil. Experiments were conducted for oil droplets

ranging from 50 μm < d_0 < 500 μm at different compressed temperatures of 700 K < T_c < 1000 K at a constant compressed pressure of 24 bar. Two far-field CH_4/O_2/inert equivalence ratios of ϕ = 0 and ϕ = 0.6 were used for the experiments.

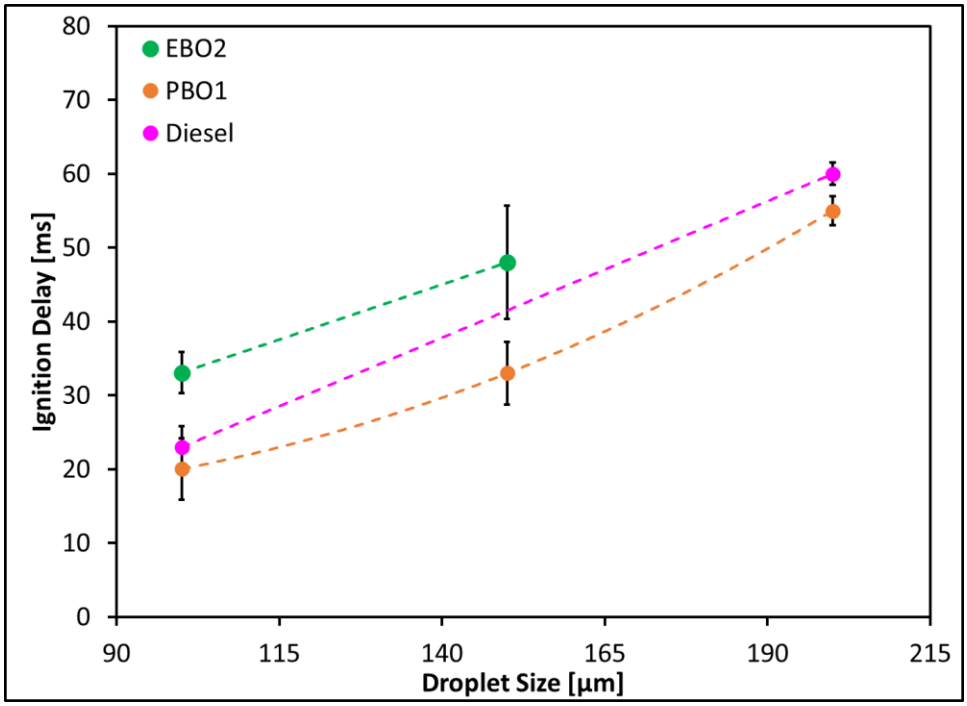

Figure 6.6. Comparison of ignition delay of EBO2 lubricant oil droplets and PBO1 lubricant oil droplets at a liquid temperature of 363 K in O_2/inert mixtures at compressed temperature and pressure of 750 K and 24 bar, respectively.

Figure 6.6 is a plot of the ignition delay period of ester-based lubricant oil (EBO2) droplets of sizes 100 μm < d_o < 200 μm in comparison to the petroleum-based lubricant oil (PBO1) droplets injected in O_2/inert mixtures at a compressed pressure of 24 bar and a compressed temperature of 750 K. As shown, an increase in the ignition delay period was observed as the droplet size increased. The ignition delay period of EBO2 oil was higher than the PBO1 lubricant oil droplets at all the droplet sizes ranging from 100 μm to 200 μm. Compared to the diesel droplets, the ignition delay of the EBO2 droplets were still higher, indicating that the ester-based oils have either or both a slow evaporation rate and a slower chemical kinetics scheme for ignition.

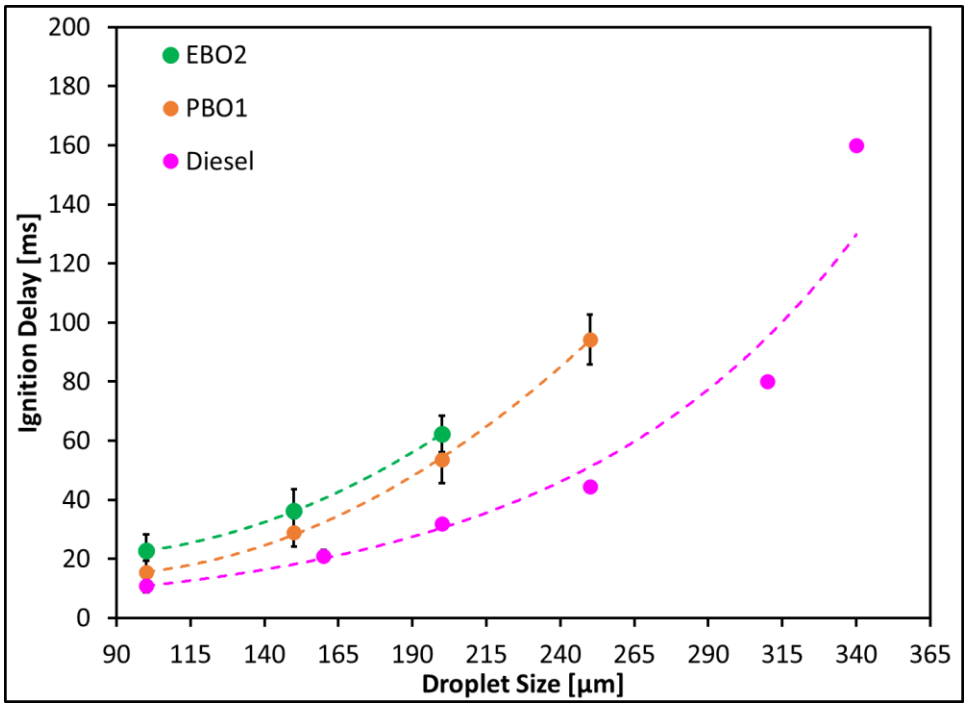

Figure 6.7. Comparison of ignition delay of EBO2 lubricant oil droplets and PBO1 lubricant oil droplets at a liquid temperature of 363 K in O_2/inert mixtures at compressed temperature and pressure of 850 K and 24 bar, respectively.

Figure 6.7 is a plot of the ignition delay period of ester-based lubricant oil (EBO2) droplets of sizes 100 µm < d_o < 365 µm in comparison to the petroleum-based lubricant oil (PBO1) droplets injected in O_2/inert mixtures at a compressed pressure of 24 bar and a compressed temperature of 850 K. As shown, the ignition delay period was observed as the droplet size increased. The ignition delay period of EBO2 oil was higher than the PBO1 oil and diesel droplets at all the droplet sizes ranging from 100 µm to 350 µm.

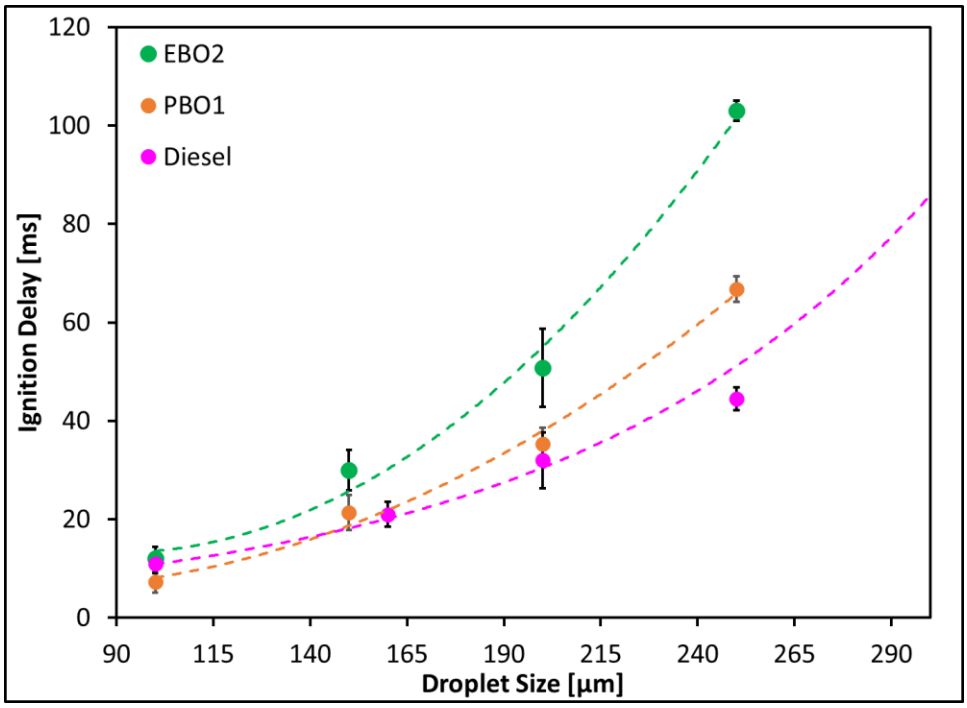

Figure 6.8. Comparison of ignition delay of EBO2 lubricant oil droplets and PBO1 lubricant oil droplets at a liquid temperature of 363 K in O_2/inert mixtures at compressed temperature and pressure of 900 K and 24 bar, respectively.

Figure 6.8 is a plot of the ignition delay period of ester-based lubricant oil (EBO2) droplets of sizes 100 µm < d_o < 250 µm in comparison to the petroleum-based lubricant oil (PBO1) droplets injected in O_2/inert mixtures at a compressed pressure of 24 bar and a compressed temperature of 900 K. As shown, an increase in the ignition delay period was observed as the droplet size increased. The ignition delay period of EBO2 oil was higher than the PBO1 oil and diesel droplets at all the droplet sizes ranging from 100 µm to 250 µm.

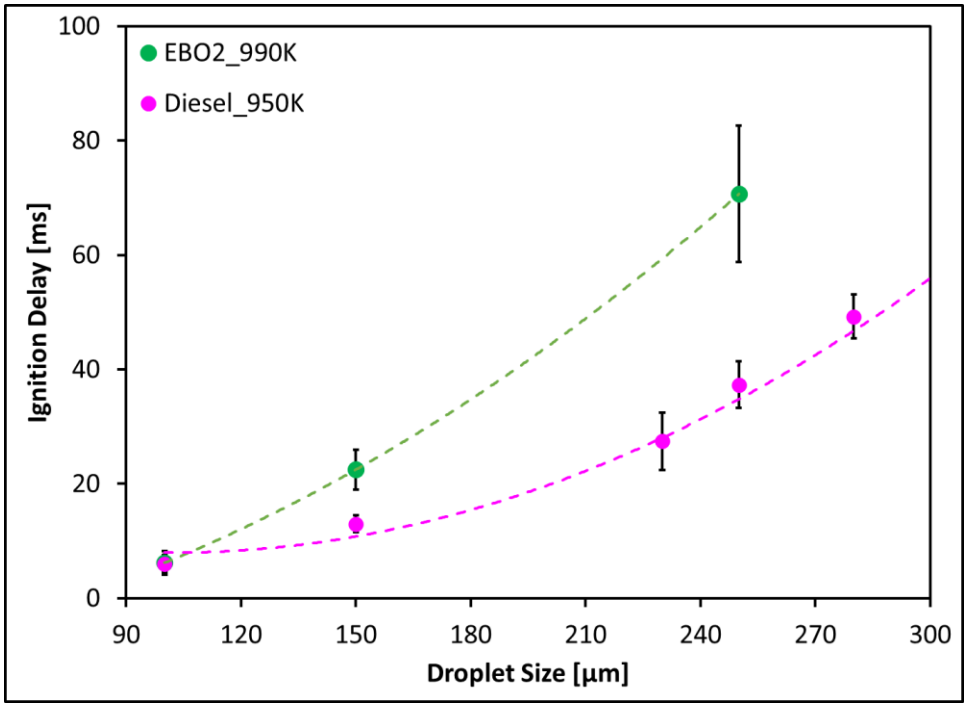

Figure 6.9. Comparison of ignition delay of EBO2 lubricant oil droplets at a liquid temperature of 363 K and diesel droplets at a liquid temperature of 303 K in O_2/inert mixtures.

Figure 6.9 is a plot of the ignition delay period of ester-based lubricant oil (EBO2) droplets of sizes 100 µm < d_o < 250 µm compared to the certification diesel droplets injected in O_2/inert mixtures at a compressed pressure of 24 bar. The compressed temperature for diesel was 950 K and for oils was 990 K. As shown, an increase in the ignition delay period of EBO2 oil droplets was observed as the droplet size was increased. The ignition delay period of EBO2 oil was higher than diesel droplets at all droplet sizes ranging from 100 µm to 250 µm. Comparing Figure 6.6, Figure 6.7, Figure 6.8, and Figure 6.9, the ignition delay period of the EBO2 droplets is higher than the PBO1 for all the droplet sizes at all compressed temperatures.

After investigating the ignition delay period of EBO2 oil in an O_2/inert mixture, experiments were conducted to study the ignition characteristics of the EBO2 droplets in a lean CH_4/O_2/inert mixture of equivalence ratio $\phi = 0.6$.

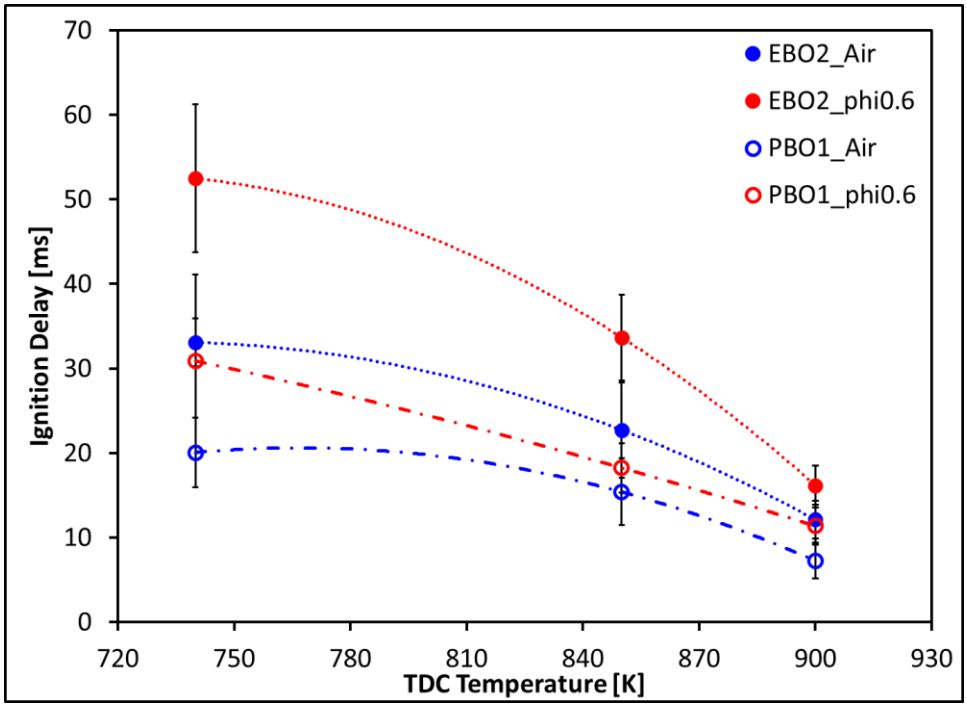

Figure 6.10. Comparison of ignition delay of EBO2 lubricant oil droplets of size 100 μm at a liquid temperature of 363 K in CH_4/O_2/inert mixture at an equivalence ratio of $\phi = 0.6$ and in O_2/inert mixtures at compressed temperatures of 750 K < T_c < 900 K and pressure of 24 bar.

Figure 6.10 is a plot of the ignition delay period of ester-based lubricant oil EBO2 droplets of size 100 μm injected in CH_4/O_2/inert mixture at an equivalence ratio of $\phi = 0.6$ and in O_2/inert mixtures at compressed temperatures of 750 K < T_c < 900 K and constant compressed pressure of 24 bar in comparison to the petroleum-based oil PBO1. As shown, an increase in the ignition delay period was observed with a decrease in compressed temperature. Also, an increase in the ignition delay period was observed with the addition of CH_4 in O_2/Inert mixtures, i.e., at $\phi = 0.6$. For all the experiments conducted in the CH_4/O_2/inert mixture of $\phi = 0.6$, the ignition of the droplets resulted in a stationary diffusion flame around the droplet, which ignited the propagating premixed flame in the CH_4/O_2/inert mixture. Comparing the ignition delay periods of EBO2 and PBO1 oils, the EBO2 ignition delay period in $\phi = 0.6$ is way longer than the PBO1 oil droplet.

6.4.3. Ignition Characteristics of Ester-Based Oil, EBO3

This section presents an experimental investigation study of understanding the abnormal combustion triggered by ester-based lubricant oil EBO3 droplets. Experiments were conducted for oil droplets ranging from 50 μm < d_0 < 500 μm at different compressed temperatures of 700 K < T_c < 1000 K at a constant pressure of 24 bar. Two far-field CH_4/O_2/inert equivalence ratios of ϕ = 0 and ϕ = 0.6 were used for the experiments.

Experiments with EBO3 droplets were conducted initially at a compressed pressure of 24 bar and a compressed temperature of 750K with a farfield methane-air equivalence ratio of 0.6 and in an O_2/inert mixture. No ignition of EBO3 oils was observed at these conditions. All the smaller EBO3 droplets completely evaporated, and bigger droplets, after completing their trajectory in the combustion domain, ended up falling on the RCM walls. Similar results were also obtained during experiments conducted at compressed pressure of 24 bars and a compressed temperature of 850K.

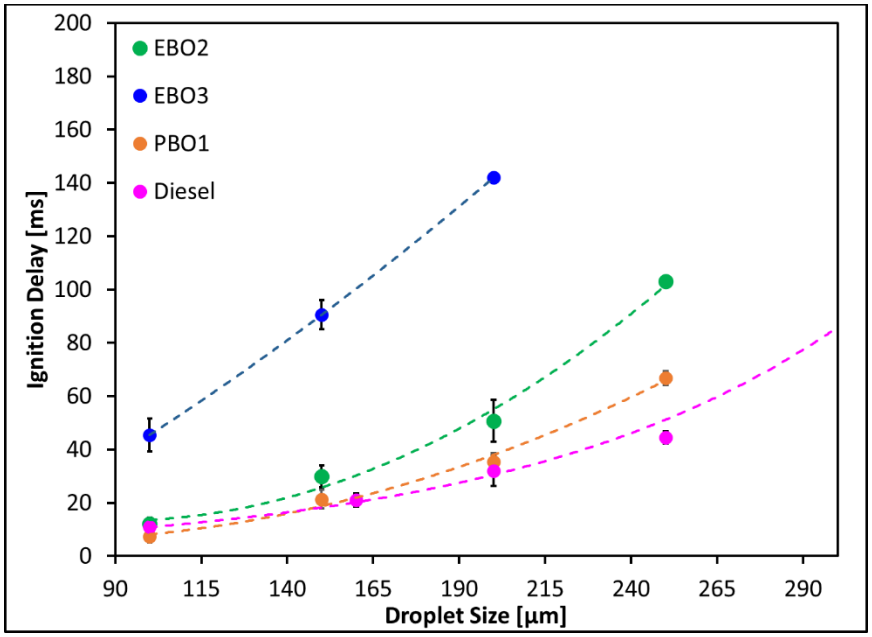

Figure 6.11. Comparison of ignition delay of EBO3 lubricant oil droplets with EBO2 and PBO1 lubricant oil droplets at a liquid temperature of 363 K in O_2/inert mixtures at compressed temperature and pressure of 900 K and 24 bar, respectively.

Figure 6.11 is a plot of the ignition delay period of ester-based lubricant oil (EBO3) droplets of sizes 100 μm < d_o < 200 μm in comparison to the ester-based lubricant oil (EBO2) and petroleum-based oil (PBO1) droplets injected in O_2/inert mixtures at a compressed pressure of 24 bar and a compressed temperature of 900 K. As shown, an increase in the ignition delay period was observed with the droplet size. The ignition delay period of EBO3 oil was found to be significantly higher than the PBO1 oil and diesel droplets at all droplet sizes ranging from 100 μm to 200 μm at a compressed temperature of 900K.

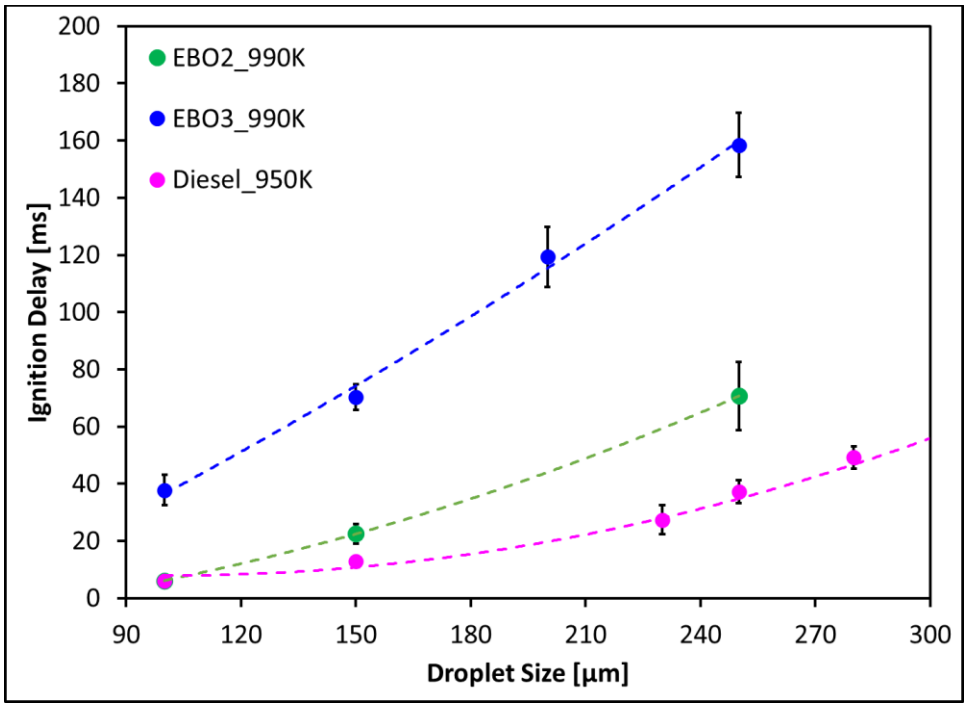

Figure 6.12. Comparison of ignition delay of EBO3 lubricant oil droplets with EBO2 and PBO1 lubricant oil droplets at a liquid temperature of 363 K in O_2/inert mixtures at compressed temperature and pressure of 990 K and 24 bar, respectively.

Figure 6.12 is a plot of the ignition delay period of ester-based lubricant oil (EBO3) droplets of sizes 100 μm < d_o < 250 μm in comparison to the certification diesel droplets and ester-based lubricant oil (EBO2) droplets injected in O_2/inert mixtures at a compressed pressure of 24 bar. The compressed temperature for diesel was 950 K and for all oils was 990 K. As shown, an increase in

the ignition delay period of EBO3 oil droplets was observed as the droplet size was increased. The ignition delay period of EBO3 oil was significantly higher than diesel and EBO2 droplets at all droplet sizes ranging from 100 μm to 250 μm. Comparing Figure 6.11 and Figure 6.12, the ignition delay period of the EBO3 droplets is significantly higher than the PBO1 and EBO2 oil droplets for all the droplet sizes. Also, the ignition delay period decreases with an increase in compressed temperatures.

After investigating the ignition delay period of EBO3 oil in an O_2/inert mixture, experiments were conducted to study the ignition characteristics of EBO3 oil droplets in lean methane/air mixtures of equivalence ratio $\phi = 0.6$. At all the compressed temperatures ranging from 740 K < T_c < 900 K at compressed pressure of 24 bar, the smaller EBO3 droplets evaporated completely, and no droplet ignition was observed. The bigger droplets evaporated partially and fell on the RCM walls after completing its trajectory, and no ignition was observed. Experiments carried out with EBO3 oils at various thermodynamic and mixture conditions reveal that the EBO3 oils have a high resistance to ignition and thus can be considered a good lubricant oil to mitigate any abnormal combustion potentially triggered by lubricant oil droplets in natural gas engines.

6.4.4. Ignition Characteristics of Ester-Based Oil, EBO4

This section presents an experimental investigation study of understanding the abnormal combustion triggered by ester-based lubricant oil, EBO4 droplets. Experiments were conducted for oil droplet sizes ranging from 50 μm < d_0 < 500 μm at different compressed temperatures of 700 K < T_c < 1000 K at a constant pressure of 24 bar. Two far-field CH_4/O_2/inert equivalence ratios of $\phi = 0$ and $\phi = 0.6$ were used for the experiments.

Experiments with EBO4 droplets were conducted initially at a compressed pressure of 24 bar and compressed temperature of 750K with a farfield CH_4/O_2/Inert equivalence ratio of 0.6 and in an O_2/inert mixture. No ignition of EBO3 oils were observed at these conditions. All the smaller EBO4 droplets completely evaporated, and bigger droplets, after completing its trajectory in the combustion domain, ended up falling on the RCM walls.

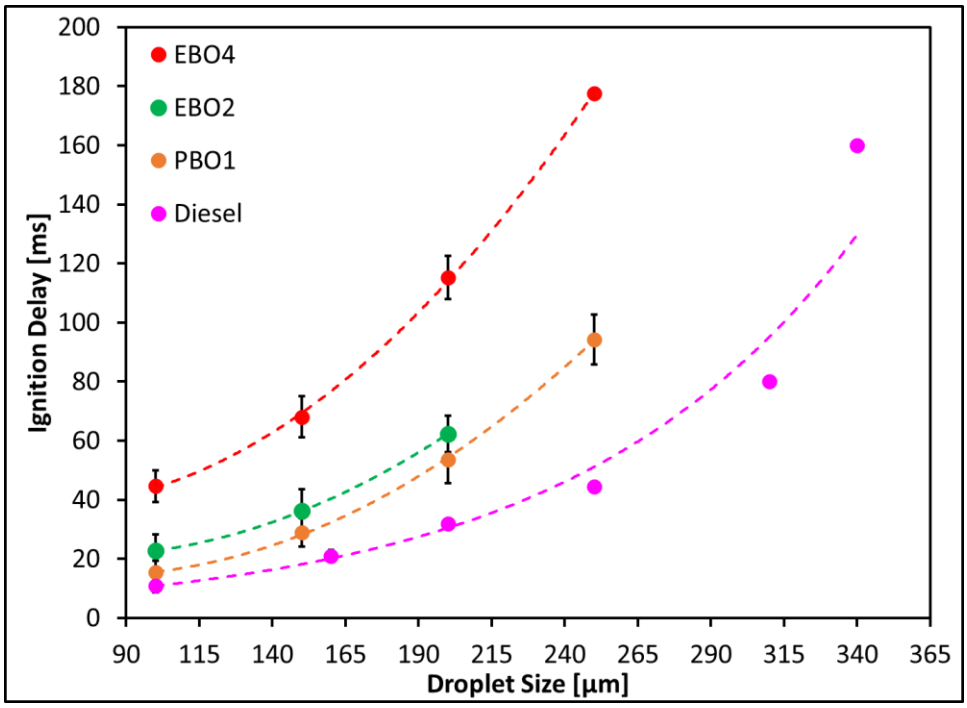

Figure 6.13. Comparison of ignition delay of EBO4 lubricant oil droplets with EBO2 and PBO1 lubricant oil droplets at a liquid temperature of 363 K in O_2/inert mixtures at compressed temperature and pressure of 850 K and 24 bar, respectively.

Figure 6.13 is a plot of the ignition delay period of ester-based lubricant oil (EBO4) droplets of sizes 100 µm < d_o < 200 µm in comparison to the ester-based lubricant oils EBO2, EBO3, and petroleum-based oil PBO1 droplets injected in O_2/inert mixtures at a compressed pressure of 24 bar and compressed temperature of 850 K. As shown, an increase in the ignition delay period was observed with the droplet size. The ignition delay period of EBO4 oil was significantly higher than

the PBO1 oil, EBO2 oil, and diesel droplets at all droplet sizes ranging from 100 µm to 200 µm at a compressed temperature of 850K.

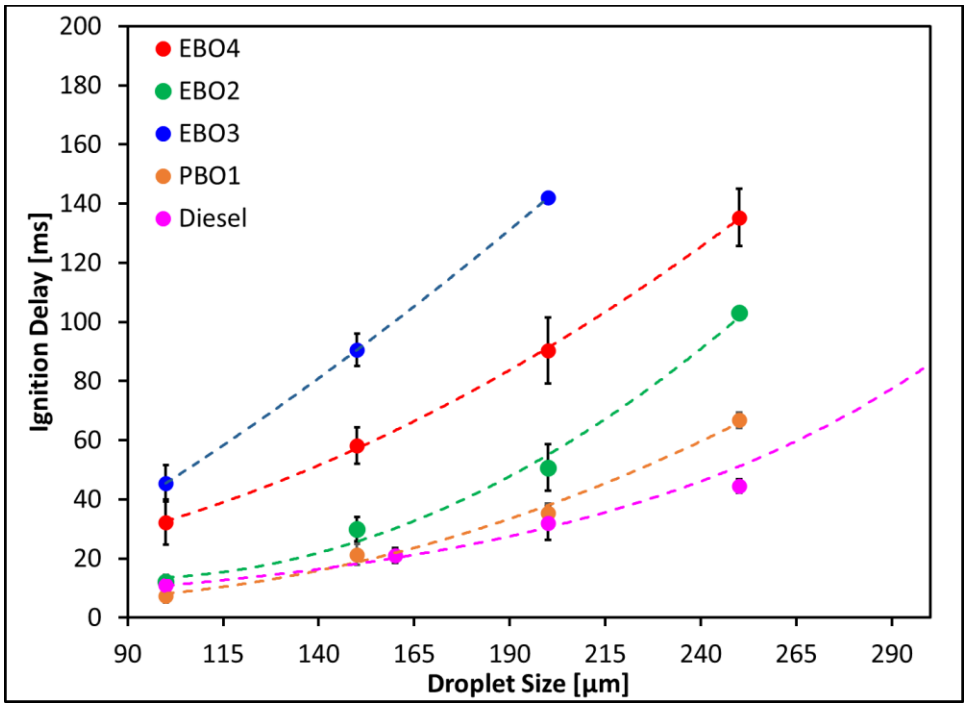

Figure 6.14. Comparison of ignition delay of EBO4 lubricant oil droplets with EBO2, EBO3, and PBO1 lubricant oil droplets at a liquid temperature of 363 K in O_2/inert mixtures at compressed temperature and pressure of 900 K and 24 bar, respectively.

Figure 6.14 is a plot of the ignition delay period of ester-based lubricant oil (EBO4) droplets of sizes 100 µm < d_o < 250 µm in comparison to the ester-based lubricant oils EBO2, EBO3, and petroleum-based oil PBO1 droplets injected in O_2/inert mixtures at a compressed pressure of 24 bar and a compressed temperature of 850 K. As shown, an increase in the ignition delay period was observed with the droplet size. The ignition delay period of EBO4 oil was found to be significantly higher than PBO1 oil, EBO2 oil, and diesel droplets at all droplet sizes ranging from 100 µm to 250 µm at a compressed temperature of 900K. On the other hand, compared to EBO3

oil, the ignition delay period of EBO4 oil droplets was found to be lower for all droplet sizes at a compressed temperature of 900 K.

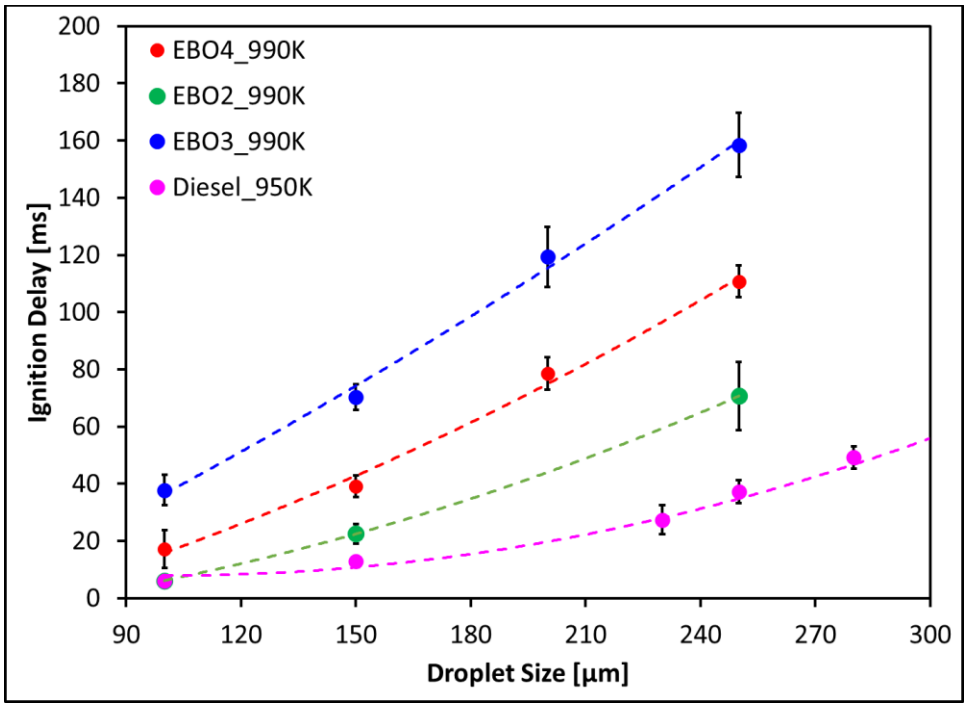

Figure 6.15. Comparison of ignition delay of EBO4 lubricant oil droplets with EBO2, EBO3, and PBO1 lubricant oil droplets at a liquid temperature of 363 K in O_2/inert mixtures at compressed temperature and pressure of 990 K and 24 bar, respectively.

Figure 6.15 is a plot of the ignition delay period of ester-based lubricant oil (EBO4) droplets of sizes 100 µm < d_o < 250 µm in comparison to the ester-based lubricant oils EBO2, EBO3, and petroleum-based oil PBO1 droplets injected in O_2/inert mixtures at a compressed pressure of 24 bar and a compressed temperature of 990 K. As shown, an increase in the ignition delay period was observed with the droplet size. The ignition delay period of EBO4 oil was significantly higher than the PBO1 oil, EBO2 oil, and diesel droplets at all droplet sizes ranging from 100 µm to 250 µm at a compressed temperature of 990K. Compared to EBO3, the ignition delay period of EBO4 oil droplets was found to be comparatively lower for all droplet sizes at a compressed temperature of 990 K.

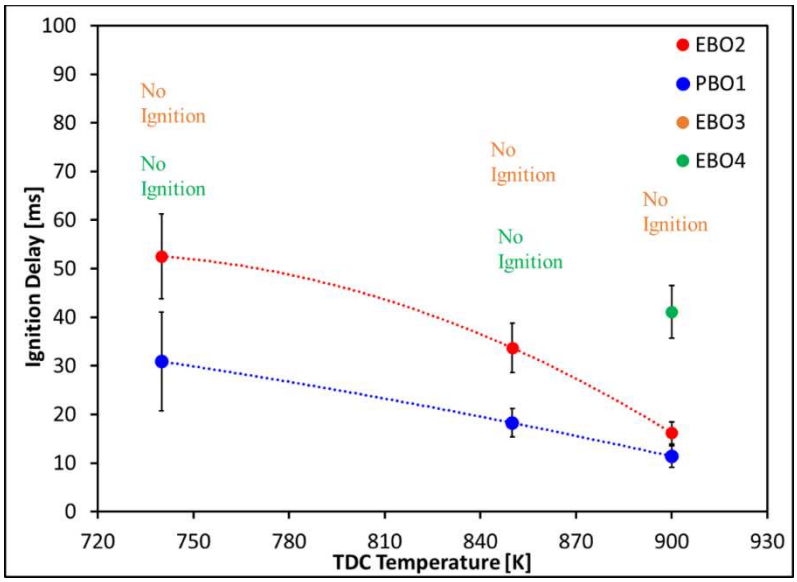

Figure 6.16. Comparison of ignition delay of PBO1, EBO2, EBO3, and EBO4 lubricant oil droplets of size 100 μm at a liquid temperature of 363 K in CH_4/O_2/inert mixture at an equivalence ratio of $\phi = 0.6$ at compressed temperatures of 740 K < T_c < 900 K and pressure of 24 bar.

Figure 6.16 is a plot of the ignition delay period of all the lubricant oils, namely the PBO1, EBO2, EBO3, and EBO4 for droplet size of 100 μm injected in CH_4/O_2/inert mixtures at equivalence ratio $\phi = 0.6$ at compressed pressure of 24 bar and compressed temperature varied from 740 K < T_c < 900 K. As shown, an increase in the ignition delay period was observed with a decrease in the far-field temperature. The ignition delay period of PBO1 oil was found to be the lowest, followed by the ignition delay period of EBO2 lubricant oil and then EBO4 lubricant oil. The EBO4 oil droplet only ignited at a compressed temperature of 900 K. But the ignition of droplets at this condition was inconsistent and in 60% of the experimental cases, the EBO4 droplets did not ignite. At lower temperatures, the EBO4 droplets showed no ignition.

On the other hand, the EBO3 droplets did not ignite in the CH_4/O_2/inert mixture at all compressed temperatures used for the RCM experiments. It can be concluded from this experimental dataset that EBO3 lubricant has the highest potential to mitigate the abnormal combustion caused by lubricant oil droplets in natural gas engines, followed by EBO4 lubricant

oil. Petroleum-based oil, PBO1, showed ignition for all the thermodynamic and mixture conditions used in the experiments and can be considered as the oil with the highest possibility of creating abnormal combustion in natural gas engines.

6.5. Conclusion

The experiments with petroleum and ester-based lubricant oils were successfully conducted for oil droplet sizes ranging from 100 μm < d_0 < 500 μm at different compressed temperatures of 740 K < T_c < 1000 K at a constant pressure of 24 bar at varied far-field $CH_4/O_2/N_2$/Ar mixture equivalence ratios ranging from 0 < ϕ < 1.2. Experiments provided a valuable dataset of ignition delay periods of different petroleum and ester-based lubricant oils at various thermodynamic and mixture conditions, which can be used to develop a chemical kinetic mechanism for the different lubricant oils. The chemical kinetic mechanism can further be used in the CFD models to understand the abnormal combustion triggered by lubricant oil droplets in natural gas engines. Along with providing the ignition delay period dataset for lubricant oils, the experiments also revealed different thermodynamic and mixture conditions at which the lubricant oil droplets did not show ignition. These experimental observations further enhance our understanding of lubricant oil combustion and provide qualitative information of engine operating conditions which can lower the abnormal combustion occurrence in natural gas engines.

The dataset and regimes of ignition behavior of different lubricant oil droplets obtained in the experiments provide a wide and adequate range of data which can be used to develop a good chemical kinetic mechanism for different lubricant oil droplets to study its interaction with natural gas/air mixtures and develop advance CFD engine model. Results from the CFD studies can then

be used to develop strategies for controlling and mitigating the abnormal combustion triggered by lubricant oil droplets.

CHAPTER 7: SURROGATE CHEMICAL KINETIC MECHANISM DEVELOPMENT FOR LUBRICANT OIL IGINITON CHARACTERISTICS

7.1. Introduction

This chapter focuses on developing a surrogate chemical kinetic mechanism for four lubricant oil types: the petroleum-based PBO1 oil and ester-based EBO2, EBO3, and EBO4 oils. The surrogate chemical kinetic mechanism for different lubricant oil types was validated using the RCM ignition delay period dataset and with different ignition regimes observed in the RCM experiments. The validated surrogate chemical kinetic mechanism will then be used in the CFD modeling of single-cylinder Caterpillar Inc. natural gas engines to study the ignition characteristics of lubricant oil droplets in an engine environment. The computational fluid dynamic study of droplets igniting in natural gas/air mixtures in a turbulent engine-like environment will further help in developing a better understanding of the abnormal combustion triggered by lubricant oil droplets. The learning of CFD models will then be used for designing single-cylinder engine experiments to develop strategies to mitigate the abnormal combustion triggered by lubricant oil droplets in natural gas engines for improving engine performance.

7.2. Approach for Surrogate Chemical Kinetic Mechanism Development

The approach for developing the chemical kinetic mechanism for different lubricant oil types is as follows:

1. Use the transient analytical droplet evaporation model for modeling the droplet evaporation rate by using the different physical properties associated with four lubricant oil types.
2. Model the oil droplet ignition RCM experiments in Converge CFD code by providing the droplet's evaporation rate and surface temperature from the analytical droplet evaporation

model to a physical spherical boundary acting as a source term in the CFD model. This source term will release the oil vapor, mimicking the droplet evaporation process. The SAGE combustion model will be turned ON to handle the combustion chemistry to study the ignition characteristics of oil droplets using a two-component surrogate chemical kinetic mechanism.

3. Assign a certain percentage of the two components in the chemical kinetic mechanism to four different oil types, representing the surrogate composition for the particular lubricant oil type under consideration.
4. Validate the surrogate composition assigned to the lubricant oils by conducting RCM CFD modeling of lubricant oil droplets and comparing the results to the ignition delay periods obtained in the RCM experiments.

7.3. Evaporation Model for Lubricant Oils

The transient analytical model discussed in Chapter 3 is used to model the evaporation of the four lubricant oils. The evaporation model is sensitive to the boiling point, the heat of vaporization and the mass diffusivity of the hydrocarbon and can change the evaporation rate significantly. The lubricant oil properties used for the simulations are shown in Table 7.1, along with heptane and diesel properties for comparing their evaporation rates to different lubricant oil types. Table 7.1 shows that boiling points are available for all the lubricant oil types, but the heat of vaporization and mass diffusivity datasets are unavailable for the oils under consideration. In order to ensure that the evaporation rates of different lubricant oils are accurately represented, a literature review or a strategy for predicting the mass diffusivity and heat of vaporization of different lubricant oils was required.

Table 7.1. Properties of heptane, diesel, petroleum-based lubricant oil PBO1, and three ester-based lubricant oils, namely EBO2, EBO3, and EBO4, used in the evaporation modeling

Heptane	
Density [kg/m^3]	684
Boiling Point [K]	373
Specific Heat C_p [J/kgK]	2240
Heat of Vaporization, h_{fg} [J/kgK]	316000
Molecular Weight	100
Thermal Conductivity, k [W/mK]	0.14

(a)

Diesel	
Density [kg/m^3]	830
Boiling Point [K]	530
Specific Heat C_p [J/kgK]	2100
Heat of Vaporization, h_{fg} [J/kgK]	230000
Molecular Weight	167
Thermal Conductivity, k [W/mK]	0.13

(b)

PBO1	
Density [kg/m^3]	824
Boiling Point [K]	561
Specific Heat C_p [J/kgK]	1926
Heat of Vaporization, h_{fg} [J/kgK]	-
Molecular Weight	420 [C35 hydrocarbon]
Thermal Conductivity, k [W/mK]	0.132

(c)

EBO2	
Density [kg/m^3]	891
Boiling Point [K]	573
Specific Heat C_p [J/kgK]	1831
Heat of Vaporization, h_{fg} [J/kgK]	-
Molecular Weight	360 [C30 hydrocarbon]
Thermal Conductivity, k [W/mK]	0.128

(d)

EBO3	
Density [kg/m^3]	899
Boiling Point [K]	589
Specific Heat C_p [J/kgK]	1751
Heat of Vaporization, h_{fg} [J/kgK]	-
Molecular Weight	432
Thermal Conductivity, k [W/mK]	0.118

(e)

A literature study was conducted to find the heat of vaporization and mass diffusivity of higher hydrocarbons, but there was no data available for both heat of vaporization and mass diffusivity for the compounds with carbon number higher than 14 [63]. Since the lubricant oils had more than 30 carbons in the compound, an extrapolation process was conducted to estimate the heat of formation and mass diffusivities of the four different lubricant oil types.

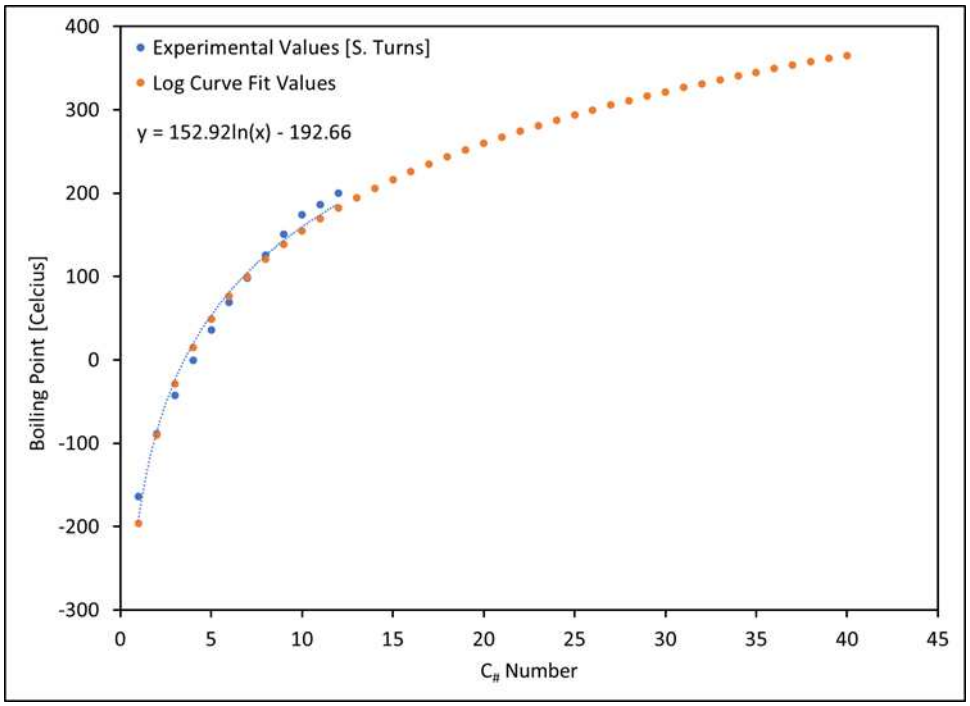

Figure 7.1. The boiling point of different hydrocarbons from C_1- C_{12} and a logarithmic curve fit for the dataset with extrapolation to carbon number C_{40}.

The heat of vaporization is a strong function of the boiling point of the hydrocarbon. Hence, it was essential to establish that the extrapolation of the dataset would closely predict the boiling point (available dataset, as shown in Table 7.1) of lubricant oils. Using the logarithmic curve fit, the extrapolated dataset predicts the boiling point above 300^{o}C after carbon number 30. Since all the lubricant oils have a long chain hydrocarbon above carbon number 30 with a boiling point

around 350°C, the logarithmic curve fit was considered an adequate fit for predicting the boiling point of the lubricant oils and further for predicting the heat of vaporization.

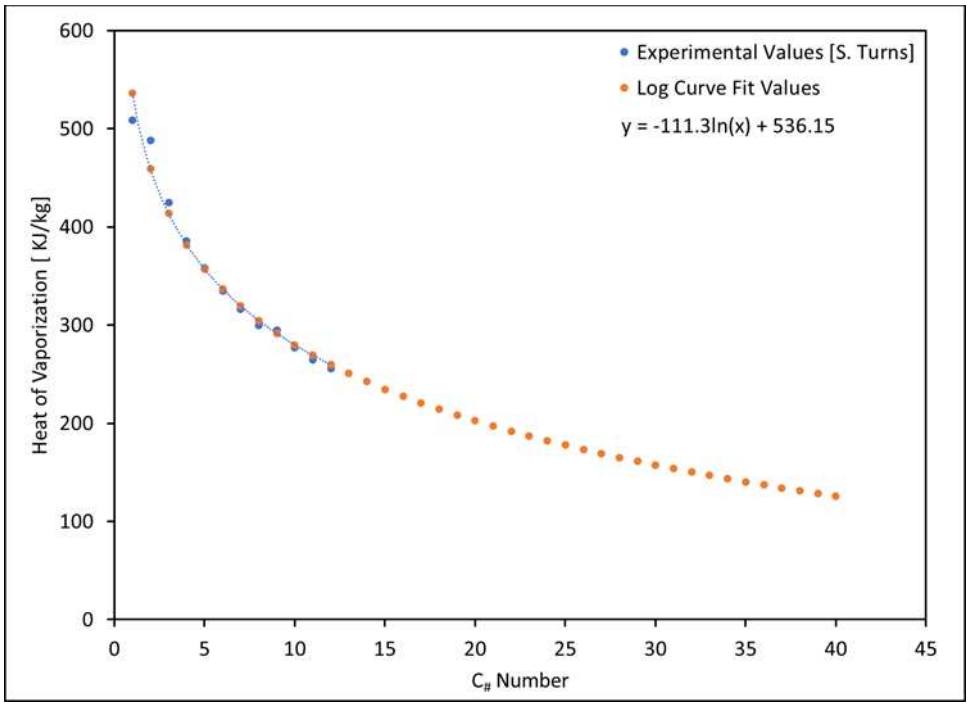

Figure 7.2. The heat of vaporization of different hydrocarbons from C_1- C_{12} and a logarithmic curve fit for the dataset with extrapolation to carbon number C_{40}.

After predicting the boiling point of different lubricant oils using a logarithmic curve fit for extrapolation of the available dataset, similar efforts were carried out to predict the heat of vaporization of different lubricant oil types. As shown, the data available in the literature [63] is only available for hydrocarbons up to carbon number 12. The logarithmic curve fit is used for extrapolating and predicting the heat of vaporization of lubricant oils with a carbon number greater than 30. Using this technique, the heat of formation was obtained for all lubricant oil types, which was further used in the transient analytical droplet evaporation model to predict the evaporation rate of different lubricant oils namely the PBO1, EBO2, EBO3, and EBO4 oils.

The mass diffusivity formulation was also required as it was the other sensitive parameter governing the droplet evaporation rate. For modeling the mass diffusivity of lubricant oils, the following formulation was used,

$$\mathcal{D}_{AB} = \frac{0.0266\, T^{\frac{3}{2}}}{P\, MW^{1/2} \sigma_{AB}{}^{2} \Omega} \tag{7.1}$$

where $\mathcal{D}_{AB}$ is the binary mass diffusivity of the lubricant oil and air, T is the surrounding temperature, and MW is the molecular weight of the mixture (lubricant oil and air) which is given as $\frac{2}{\left[\left(\frac{1}{MW_A}\right)+\left(\frac{1}{MW_B}\right)\right]^{-1}}$, σ_{AB} is the mean of the hard-sphere collision diameter of lubricant oil and air which is given as $\sigma_{AB} = \frac{\sigma_A + \sigma_B}{2}$, P is the surrounding pressure, and Ω is the collision integral and has a typical value of unity. The formulation details can be found in Stephen Turns's Combustion textbook [63].

The mass diffusivity study for lubricant oils was conducted by comparing the influence of all the parameters mentioned in equation 7.1 to heptane and diesel, which act as reference fuels with well-defined physical properties. The influence of surrounding pressure and temperature was the same for all the oils and reference fuels and hence was not considered as a parameter influencing the mass diffusivity while comparing lubricant oils and reference fuels. Molecular weight and hard-sphere collision diameters are, therefore, the two parameters that are considered for modeling the mass diffusivity of different lubricant oils and reference fuels (diesel and heptane).

The data for the hard collision diameter is not available in the literature for compounds with more than 6 carbon atoms [63]. Hence, an extrapolation curve fit was performed on the dataset available to estimate the hard collision diameter of different lubricant oils and reference fuels.

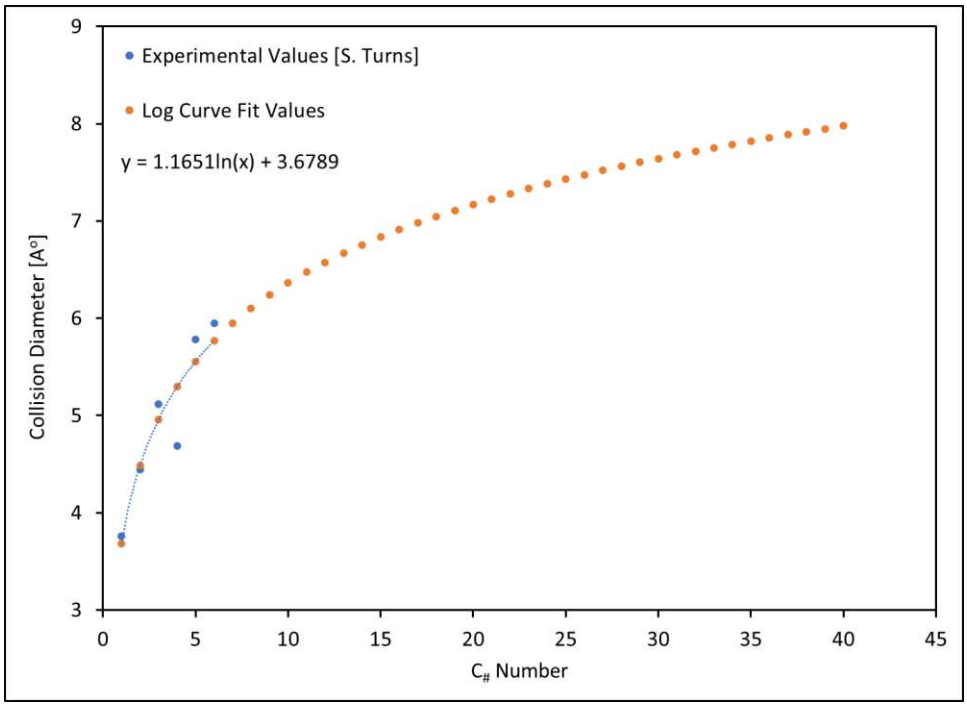

Figure 7.3. Collision Diameter of different hydrocarbons from C_1- C_6 and a logarithmic curve fit for the dataset with extrapolation to carbon number C_{40}.

Figure 7.3 shows the collision diameter dataset for different hydrocarbons from C_1- C_6 and the logarithmic curve fit performed on the dataset for extrapolating the dataset to estimate the collision diameters of the long-chain lubricant oils and reference fuels. As shown in Figure 7.3, the hard collision diameter increases with an increase in the carbon number present in the compound. Considering the molecular weight and mass diffusivity data obtained by performing the extrapolation exercise, Table 7.2 is obtained.

Table 7.2. Relative comparison of mass diffusivity of different lubricant oil types, diesel, and heptane. The mass diffusivity is compared to heptane, which is the reference fuel for the comparison. A calibration factor of 25% was used in the mass diffusivity calculation.

Compound	Molecular Weight [MW]	MW_{AB}	Collision Diameter [σ]	σ_{AB}	Diffusivity Comparison
Air	28.86	-	3.71	-	-
Heptane	100	6.69	5.95	4.83	1
Diesel	167	7.02	6.57	5.14	1.05
PBO1	420	7.35	7.82	5.77	0.8
EBO2	360	7.31	7.65	5.68	0.83
EBO3	432	7.36	7.85	5.78	0.79

As shown in Table 7.2, comparing diesel to heptane, a comparable mass diffusivity was seen, indicating that the mass diffusivity will not significantly influence diesel's evaporation rate. However, the heat of vaporization, which is a strong function of boiling point, still will influence the diesel evaporation rate as compared to heptane. Similarly, for petroleum-based oil (PBO1) and other ester-based oils, the mass diffusivity is estimated to be around ~ 20% less as compared to heptane. This will result in a slower evaporation rate for the lubricant oil types. The following evaporation profiles were obtained using the predicted heat of vaporization and mass diffusivity in the transient analytical droplet evaporation model for oils and reference fuels.

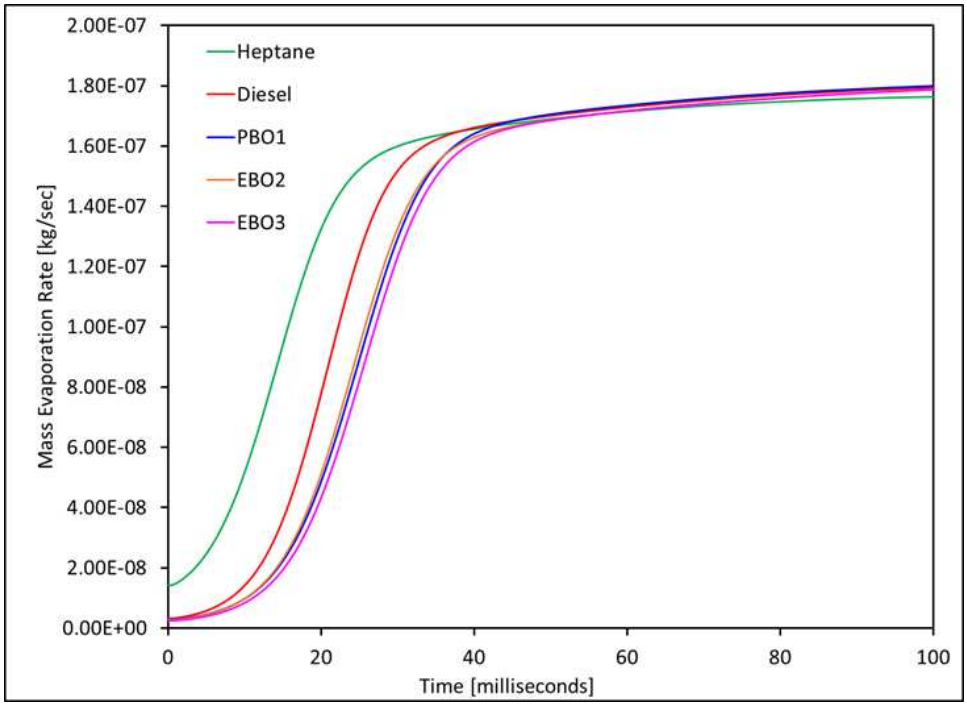

Figure 7.4. Mass evaporation rate comparison of 200 µm droplet of heptane, diesel, petroleum-based oil PBO1, ester-based oils EBO2 and EBO3 at a pressure of 1 bar and a surrounding temperature of 950 K falling under gravity.

As shown in Figure 7.4, the heptane with a lower boiling point has a faster evaporation rate, followed by diesel and the petroleum-based PBO1oil and ester-based EBO2 and EBO3 oils. The physical properties of EBO4 were unavailable, and the evaporation modeling of EBO4 oil was

carried out by assuming the physical properties of EBO3 oil. The evaporation dataset obtained from the model were then used as the input files to the Converge CFD codes for studying the ignition characteristics of different lubricant oil types.

7.4. Combustion Model of Lubricant Oils

As discussed in Chapter 3 and Chapter 4, the dual phase droplet experiments were simulated with a combined analytical droplet evaporation model and CFD model. The moving liquid droplet was modeled as a spherical fuel vapor source with surface vaporization rate and temperature determined using the transient analytical droplet evaporation model. In case of lubricant oils study, a surrogate mechanism of n-dodecane and xylene comprising of 186 species and 1014 reactions made by Hockett et al. [61] was used to replicate the combustion characteristics of different lubricant oil types. The difference in the chemical reactivity of n-dodecane and xylene was used as a knob to model the ignition characteristics of different lubricant oil types, i.e., the oil with a shorter ignition delay period will be given a higher concentration of n-dodecane and the oil with longer ignition delay period will be given the higher concentration of xylene since it has much lower reactivity as compared to n-dodecane.

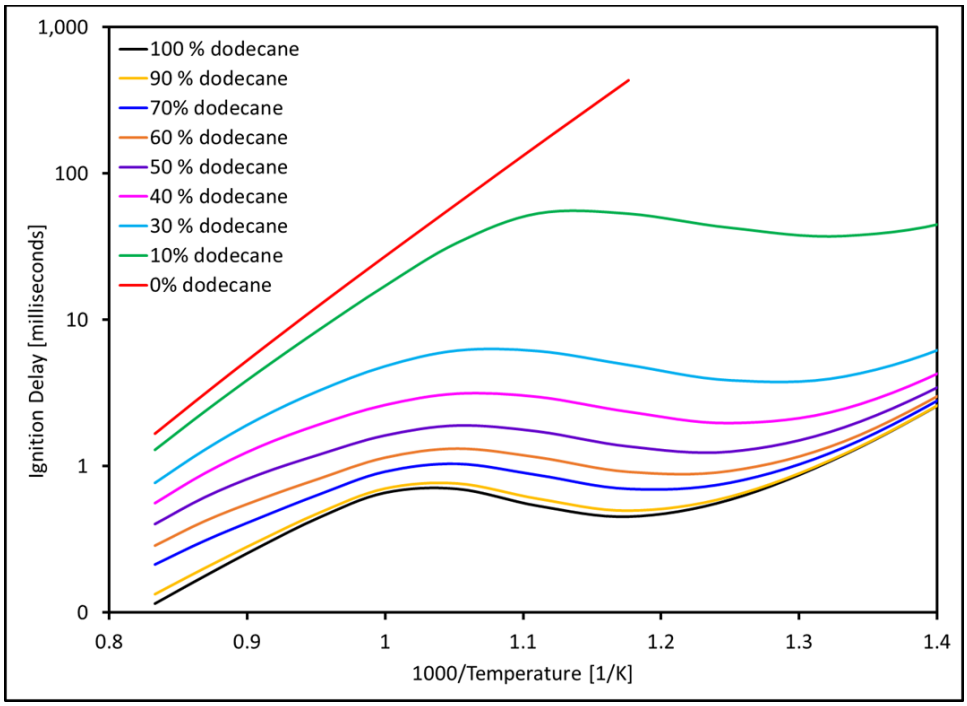

Figure 7.5. A homogenous zero-dimensional autoignition simulation for comparing the ignition delay period of different percentages of xylene and n-dodecane mixtures at pressure of 22 bar and a temperature range of 600 K to 1200 K at an equivalence ratio of 1.0 using 186 species mechanism of n-dodecane and xylene.

As shown in Figure 7.5, the lowest ignition delay period is observed for 100% n-dodecane and the ignition delay period increases significantly with the addition of xylene to the n-dodecane. With 100% xylene, the NTC behavior of the n-dodecane and xylene mixture disappears, and a very long ignition delay period is observed. The different n-dodecane and xylene compositions give a wide bandwidth of ignition delay periods and can be used effectively to model the ignition characteristics of different lubricant oil droplets.

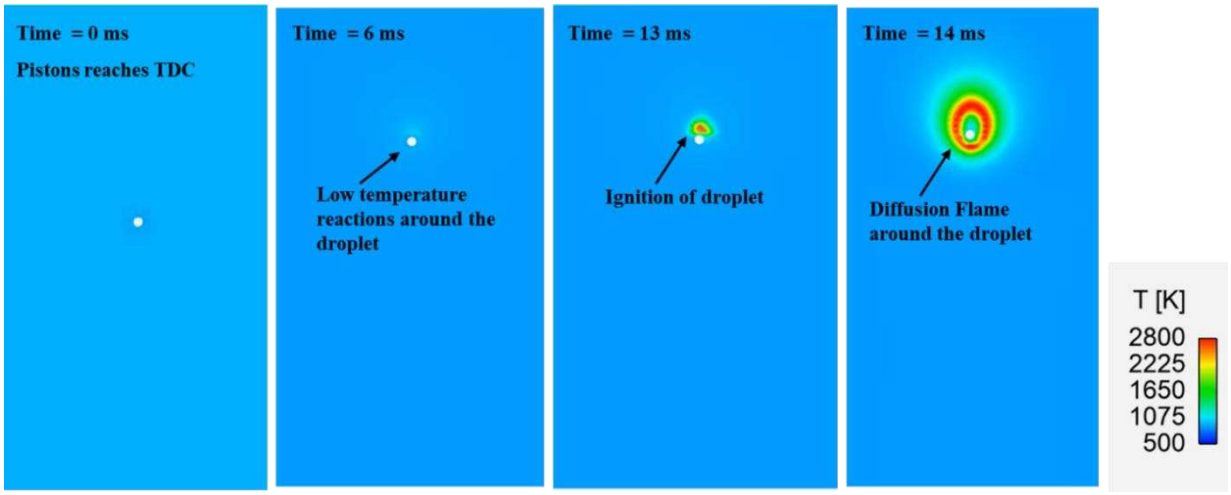

Figure 7.6. The contour of the temperature of a CFD simulation of 150 µm PBO1 lubricant oil modeled as n-dodecane injected in O_2/Inert mixture at 900K TDC temperature and 24 bar pressure in a Rapid Compression Machine

Figure 7.6 shows an example simulation of a PBO1 lubricant oil droplet of size 150 µm injected in an RCM combustion chamber at 900 K TDC temperature and 24 bar TDC pressure in O_2/Inert mixture. At time = 0 ms, the droplet travels upwards and reaches around the center of the RCM domain. Around 6 ms after TDC, low-temperature reactions occur around the droplet surface, resulting in a temperature increase around the droplet to about ~1000K. Around 13 ms, the conditions become favorable for the droplet to ignite, and the first instance of high temperature is observed slightly above the droplet, as shown in Figure 7.6. This ignition results in a formation of a stationary diffusion flame which establishes itself around the droplet at time = 14 ms. The ignition delay period is quantified as the time between the piston reaching the TDC and the first instance of the appearance of diffusion flame around the droplet surface. The CFD simulations were conducted for all lubricant oils, namely PBO1, EBO2, EBO3, and EBO4, for different temperatures ranging from 700K to 1000 K and at a constant pressure of 24 bar. The mixture composition was varied from O_2/Inert mixture to CH_4/O_2/Inert mixture of equivalence ratio ϕ = 0.6. These conditions were similar to those observed in the experiments, and a comparison was

carried out between the simulation ignition delay dataset and the experimentally observed ignition delay dataset to validate the surrogate mechanism and establish the surrogate composition for four different lubricant oil types.

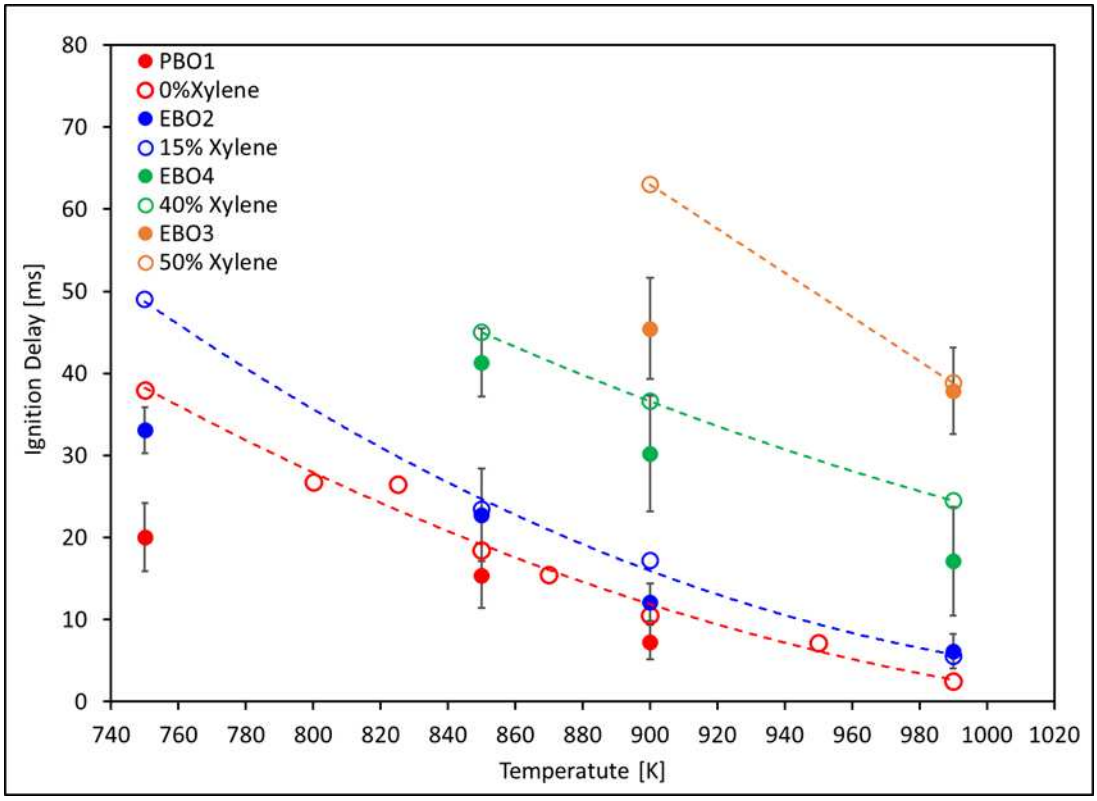

Figure 7.7. Ignition delay period dataset for 100 µm droplets of lubricant oils PBO1, EBO2, EBO3, and EBO4 for a temperature range of 750 K < T_c < 990 K at a constant compressed pressure of 24 bar in O_2/Inert mixture. Simulated ignition delay periods of different lubricant oils modeled as different composition percentages of n-dodecane and xylene are also presented at the same thermodynamic and mixture conditions.

Figure 7.7 compares the ignition delay period of 100 µm droplets of different lubricant oils obtained in the experiments and simulations at different thermodynamic and mixture conditions. As shown, 0% xylene or 100% n-dodecane as a surrogate composition for PBO1 lubricant oil predicts the ignition delay period very close to the experimental observation. The only deviation was observed at a lower temperature of 750 K, for which the CFD model predicts a higher ignition

delay period for PBO1 oil. Similarly, 15% xylene and 85% n-dodecane as a surrogate for EBO2 ester-based lubricant oil predicts the ignition delay period close to the experimental observation with a deviation observed in the ignition delay period at a lower temperature of 750 K. For EBO4 lubricant oil, 40% xylene and 60 % n-dodecane serves as good surrogate composition. For EBO3 lubricant oil, 50% xylene and 50% n- dodecane surrogate composition are good. Both surrogates for EBO3 and EBO4 lubricant oils could predict the ignition delay period closely to those observed during the experiments. The ignition delay period prediction for EBO3 oil at a compressed temperature of 900 K is higher than the experiments shown in Figure 7.7. Even with this discrepancy, the CFD result motivates and captures a borderline threshold below which the droplet ignition will not occur. The experiment results for EBO3 at 900K showed droplet igniting for 6 out of 10 cases, indicating the operating conditions to be at the borderline of droplet ignition. Thus, with CFD model predicting higher ignition delay shows the sensitivity of the model to predict the regime or conditions at which the droplet ignition will not be observed. A CFD simulation of 100 µm EBO3 droplet modeled as 50% xylene and 50% n-dodecane at a compressed temperature of 850K in O2/Inert mixture showed no droplet ignition within the time scale of RCM. The timescale of RCM is defined as the time in which the droplet remains in hot ambient conditions of the RCM chamber domain and away from the cold walls. CFD modeling study of lubricant oil droplets allowed to capture both the droplet ignition conditions and the threshold conditions at which the droplet ignition is not observed.

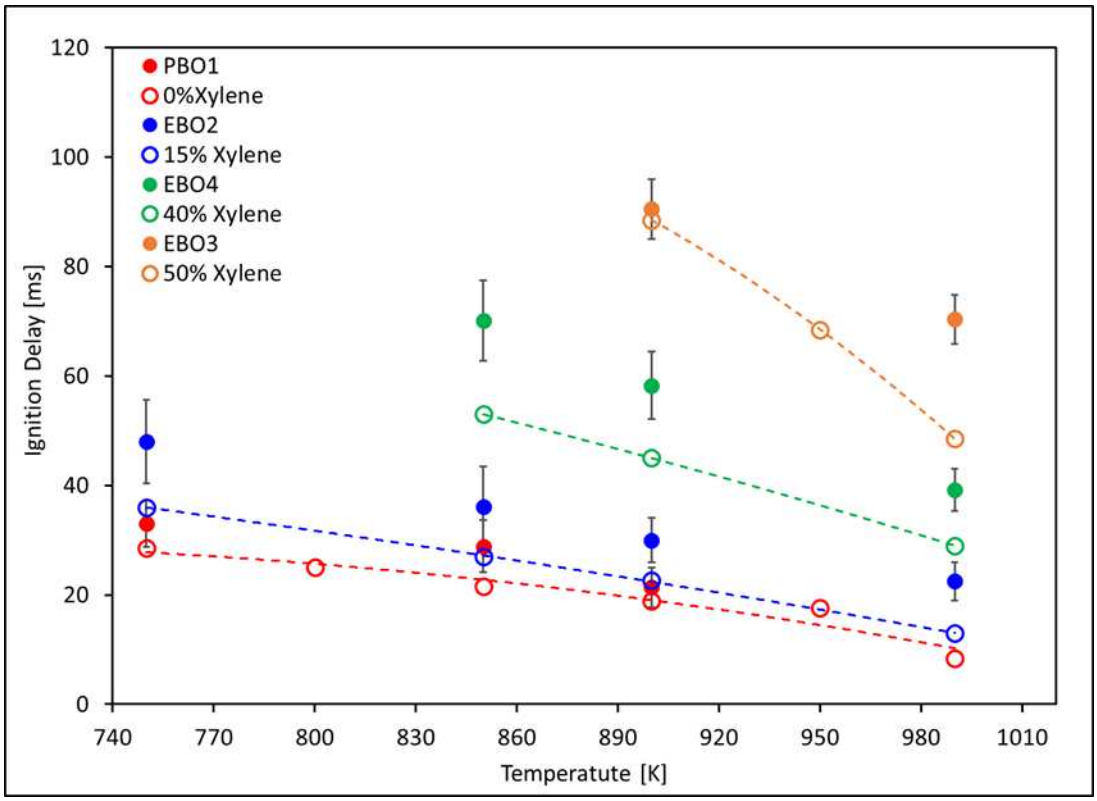

Figure 7.8. Ignition delay period dataset for 150 µm droplets of lubricant oils PBO1, EBO2, EBO3, and EBO4 for a temperature range of 750 K < T_c < 990 K at a constant compressed pressure of 24 bar in O_2/Inert mixture. Simulated ignition delay periods of different lubricant oils modeled as different composition percentages of n-dodecane and xylene are also presented at the same thermodynamic and mixture conditions.

Figure 7.8 compares the ignition delay period of 150µm droplets of different lubricant oils obtained in the experiments and simulations at different thermodynamic and mixture conditions. As shown, 0% xylene and 100% n-dodecane serve as a good surrogate for PBO1 lubricant oil, 15% xylene, and 85% n-dodecane serve as a good surrogate for EBO2 lubricant oil, 40% xylene and 60% n-dodecane serves as a good surrogate for EBO4 lubricant oil, and 50% xylene and 50% n-dodecane serves as a good surrogate for EBO3 lubricant oil. All the surrogates for the different lubricant oil types predict the ignition delay period close to the observed experimental values. The prediction of the ignition delay period for EBO4 oil using 40% xylene and 60% n-dodecane

surrogate is comparatively lower than the observed experimental observation, but the overall trend of the ignition delay period closely matches the observed experimental ignition delay trend.

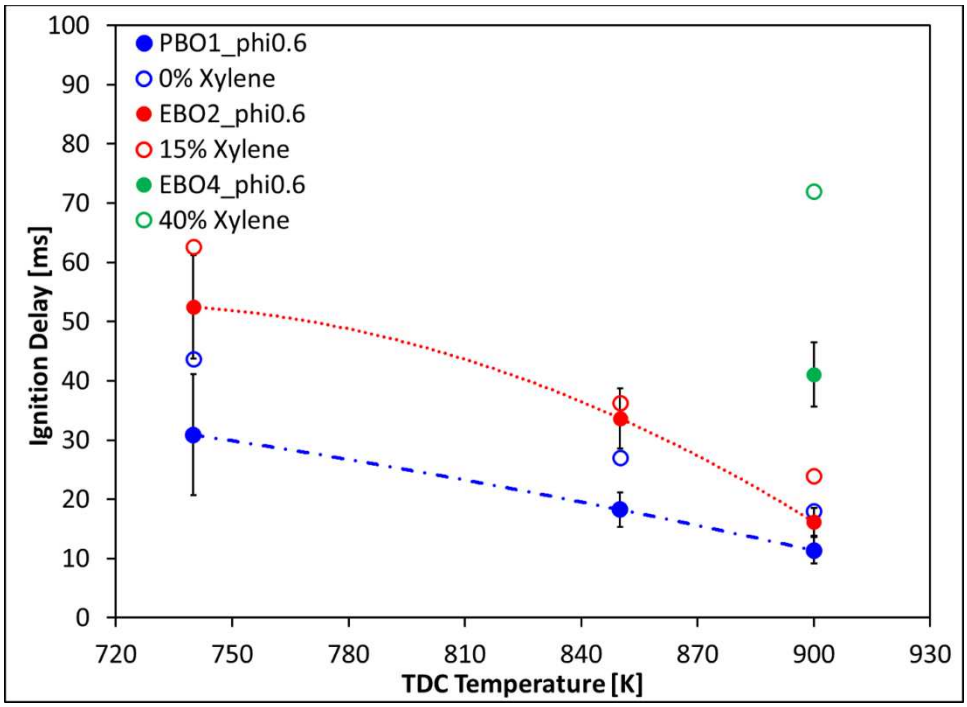

Figure 7.9. Ignition delay period dataset for 100 µm droplets of lubricant oils PBO1, EBO2, EBO3, and EBO4 for a temperature range of 750 K < T_c < 990 K at a constant compressed pressure of 24 bar in CH_4/O_2/Inert mixture at equivalence ratio, $\phi = 0.6$. Simulated ignition delay periods of different lubricant oils modeled as different composition percentages of n-dodecane and xylene are also presented at the same thermodynamic and mixture conditions.

Simulations were also performed with CH_4/O_2/Inert mixture at an equivalence ratio, $\phi = 0.6$, at different thermodynamic conditions to test the prediction of assigned surrogate composition for different lubricant oil types in CH_4/O_2/Inert mixture. As shown in Figure 7.9, the surrogate of 0% xylene and 100% n-dodecane for PBO1 oil and the surrogate of 15% xylene and 85% n-dodecane for EBO2 oil predicts the ignition delay period very close to the observed experimental values. The EBO4 surrogate, 40% xylene, and 60% n-dodecane predict higher ignition delay compared to the experimental observation at 900 K. In RCM experiments, EBO4 oil at 900K showed

inconsistent droplet ignition where only 6 out of 10 experimental cases showed droplet ignition. Therefore, the CFD model indicating the higher ignition delay period for EBO4 lubricant oil shows the borderline threshold of droplet ignition below which the droplet ignition will not be observed. The simulation for 100 µm EBO4 droplet in CH_4/O_2/Inert mixture at equivalence ratio, $\phi = 0.6$ at a compressed temperature of 850 K showed no droplet ignition within the RCM time scale.

The combination of the transient analytical droplet evaporation model and CFD Converge combustion model using the surrogate chemical kinetic mechanism was able to predict the ignition delay period of different lubricant oils at various thermodynamic and mixture conditions and also showed the potential of using the combined model to find various regimes of oil droplet combustions.

7.5. Limitation of Model

The overall model closely predicts the ignition delay periods and ignition characteristic trends with the observed experimental ignition delay periods at various thermodynamic and mixture conditions for four lubricant oils, namely PBO1, EBO2, EBO3, and EBO4. But there are certain limitations associated with the model, which are as follows,

a. The model predicts longer ignition delay periods for different lubricant oils as compared to the experiment dataset at lower compressed temperatures of < 750 K.
b. The model predicts shorter ignition delay periods for different lubricant oils as compared to the experimental dataset at higher droplet sizes > 200 µm.
c. Preferential evaporation of xylene and n-dodecane was not considered in the simulations.

d. The physical properties of ester-based oil EBO4 were not available for this study. The physical properties of EBO3 were used to model the EBO4 oil.

e. The heat of vaporization and mass diffusivity of different lubricant oil types are predicted using extrapolation of the dataset available in the literature.

f. A droplet is modeled as a source boundary releasing fuel vapor in which the boundary size remains constant. For improving the model, the boundary shrinking algorithm can be implemented to mimic droplet regression as it evaporates.

7.6. Conclusion

The CFD model and transient analytical droplet evaporation model were successfully used to demonstrate the evaporation and combustion characteristics of different lubricant oils, namely the petroleum-based oil PBO1 and three ester-based oils EBO2, EBO3, and EBO4 oils. The surrogate mechanism of n-dodecane and xylene comprising 186 species and 1014 reactions, was found to be a suitable chemical kinetic mechanism for modeling the four different oil types. The ignition delay prediction from the model was successfully compared to the observed experimental ignition delay values at various thermodynamics and mixture conditions. A close match of the ignition delay period was observed between the experimental results and the model. The following table summarizes the surrogate percentages suitable for modeling the petroleum-based PBO1 oil and three ester-based lubricant oils, EBO2, EBO3, and EBO4.

Table 7.3. Xylene and n – dodecane compositions for representing the surrogate of different lubricant oils

Lubricant Oils	Xylene, %	n - dodecane, %
PBO1	0	100
EBO2	15	85
EBO3	50	50
EBO4	40	60

CHAPTER 8: CONCLUSION AND FUTURE WORK

8.1. Conclusions

8.1.1. Development of the Piezoelectric Droplet Generator and its Integration to RCM

A piezoelectric droplet generator was successfully designed, fabricated, and integrated with the RCM system to inject single isolated liquid droplets into the RCM combustion chamber. The droplet generator has the following novel features which distinguish it from the previous designs available in the literature:

1. In current work, the piezoelectric droplet generator can create liquid hydrocarbon droplets at higher initial pressures of up to 5 bar, overcoming the limitation of traditional droplet generators, which typically operate at atmospheric pressure.
2. The droplet generator in this work is capable of handling highly viscous fluid.
3. The droplet generator configuration includes an integrated check valve assembly that prevents the backflow of the liquid fuel into the droplet generator under high-pressure conditions in the combustion chamber during RCM compression and combustion events. It also ensures that the liquid fuel reservoir and piezoelectric element are not exposed to high-pressure conditions, a critical safety requirement.
4. The droplet generator includes an integrated and controlled heating system to preheat liquid droplets.
5. The piezoelectric droplet generator can precisely control the injection timing relative to the RCM compression process.

A high-speed Schlieren optical imaging system was also employed in the experimental configuration for analyzing the ignition and evaporation characteristics of liquid hydrocarbon

droplets. With the Schlieren imaging diagnostics and capability of injecting droplets at high pressure and temperature conditions, different multiphase flow behaviors can be studied at various thermodynamic conditions in both reacting and non-reacting environments using the experimental setup described in the dissertation.

8.1.2. Studying the Fundamentals of Dual Fuel Combustion

High-reactivity liquid fuel (i.e., diesel) droplets were injected in a low-reactivity gaseous fuel-air mixture (i.e., natural gas air mixtures) at elevated pressure and temperature conditions in a quasi-steady and turbulent free domain to study the ignition characteristics of two fuels with disparate reactivities. The diesel droplet sizes were varied from 100 μm < d_o < 500 μm. The compressed pressure used for the experiments was 24 bar, with the compressed temperatures ranging from 700K < T_c < 1000K. The equivalence ratio of the gaseous methane-air mixture was varied from 0 < ϕ < 1.2. A detailed study of ignition regimes of diesel droplets was conducted by varying the thermodynamic and mixture conditions in the RCM. The study resulted in providing insights into the dual fuel combustion processes. Also, it provided a valuable dataset of ignition delay periods of different size diesel droplets at various thermodynamic and mixture conditions, which can further be used to develop and validate the existing and future dual fuel chemical kinetic mechanisms. These experiments revealed multiple modes of droplet ignition, droplet combustion, and premixed flame propagation, which depend on the initial droplet temperature, droplet diameter, droplet velocity, and stoichiometry of the $CH_4/O_2/N_2$/Ar mixture. For small droplets, spherical ignition events are observed that transition into spherical non-premixed flames that envelope the droplet. These spherical non-premixed flames produce outwardly propagating spherical premixed flames. For larger droplet diameters moving at moderate velocity, the ignition

event occurs near the droplet surface on the leeward side of the droplet and subsequently creates a non-premixed flame that envelopes the droplet and a non-spherical premixed flame. For droplets moving with high velocities, the ignition event occurs in the wake of the droplet, multiple diameters from the droplet surface, and creates a flame that propagates toward the droplet. Spherically outward propagating premixed flames were observed for diesel droplet ignition in stoichiometric $CH_4/O_2/N_2/Ar$ mixtures, whereas elongated premixed flames were observed in lean $CH_4/O_2/N_2/Ar$ mixtures.

CFD study was also conducted for validating and testing the dual fuel chemical kinetic mechanism called CSU141, consisting of 141 species and 709 reactions. The CFD model comprised an analytical transient droplet evaporation model and Converge CFD code. In Converge CFD code, the droplet was successfully modeled as a boundary that acts as a species source of fuel vapor. The droplet evaporation profile obtained from the transient evaporation model was provided to the droplet boundary in Converge CFD to replicate the droplet evaporation process. The CFD model successfully predicted the ignition delay periods closely to the observed experimental dataset for different diesel droplet sizes at various thermodynamic and mixture conditions. CFD model also accurately replicated various combustion and ignition regimes of dual fuel combustion observed during experiments.

The results of this combined experimental and modeling approach strongly suggest that ignition and combustion of liquid droplets of high chemical reactivity (e.g., diesel) in gaseous fuel/air mixtures of lower reactivity (e.g., methane/air) represent a robust system for elucidating the underlying combustion phenomena of dual fuel combustion.

8.1.3. Understanding the Abnormal Combustion caused by Lubricant Oil Droplets

The last topic discussed in the dissertation is the experimental and computational study of understanding the abnormal combustion caused by lubricant oil droplets in natural gas engines. Petroleum-based oil, PBO1, and three ester-based oils, EBO2, EBO3, and EBO4, were tested in RCM at different compressed temperatures of 700 K < T_c < 1000 K at a constant pressure of 24 bar with varying far-field methane/air equivalence ratio of 0 < ϕ < 1.2 for various sizes of lubricant oil droplets ranging from 100 µm < d_o < 500 µm. Experiments provided a valuable dataset of ignition delay periods of different lubricant oil types, which was successfully used to develop and validate a surrogate chemical kinetic mechanism. A surrogate chemical kinetic mechanism of n-dodecane and xylene comprising 186 species and 1014 reactions was successfully used to quantify the ignition behavior of different lubricant oils. A different composition % of xylene and n-dodecane was used to replicate the ignition behavior of different oils. 100% n-dodecane and 0% xylene was used as a surrogate for PBO1 oil, 85% n-dodecane and 15% xylene was used as a surrogate for EBO2 oil, 50% n-dodecane and 50% xylene was used as a surrogate for EBO3 oil, and 60% n-dodecane and 40% xylene was used as a surrogate for EBO4 oil. The experiments with different lubricant oils also provided various thermodynamic and mixture conditions at which lubricant oil droplets only evaporate, with no observed droplet ignition. The study thus provided an overall understanding of different thermodynamic and mixture conditions at which control of the abnormal combustion can be achieved. The surrogate chemical kinetic mechanism developed and validated in this study predicted the ignition delay periods of different lubricant oils and showed sensitivity in predicting the borderline combustion/ignition events observed experimentally.

8.2. Future Work

One of the droplet generator's limitations was the piezoelectric element's operational temperature (100°C) which limited the study to a liquid fuel temperature of ~ 100°C. In the future, the design can be enhanced by improving cooling around the piezoelectric element, allowing experiments at higher initial liquid fuel and lubricant oil temperatures. The second limitation is the heating provided by cartridge heaters. The cartridge heaters increase the temperature near the nozzle of the droplet generator and can result in igniting the gaseous fuel/air mixture due to surface ignition even before the droplet ignites. Cooling strategies should be developed and implemented near the nozzle of the droplet generator to conduct experiments at even higher compressed temperature and pressure conditions and limit the surface ignition events near the nozzle.

For the dual-fuel combustion study with diesel droplets in methane/air mixtures, an additional dataset of ignition delay periods can be collected at various droplet sizes at higher compressed temperatures ~ 1100 K and pressure conditions ~35 bar. This dataset can then be used for testing the performance of dual-fuel chemical kinetic mechanisms at aggressive thermodynamic conditions. Experiments conducted at higher temperature and pressure conditions can also be used to study the end gas autoignition events caused by droplet ignition. This future study can thus provide a holistic understanding of both ignition limits (end gas autoignition events and misfire events) associated with dual fuel combustion. Dual fuel experiments can also be conducted with future carbon neutral fuels such as ammonia, methanol, and hydrogen with different pilot injection fuels such as dimethyl ether. These experiments can provide the necessary ignition delay dataset and flame speed measurements which can be used for developing the chemical kinetic mechanisms for the future carbon neutral fuels.

Future work for understanding abnormal combustion caused by lubricant oil droplets will be to use the CFD model and the validated surrogate chemical kinetic mechanism developed in this study for doing engine CFD modeling work on Caterpillar Inc.'s single-cylinder engines. The CFD modeling study of engines will further enhance the understanding of abnormal combustion events in an engine environment and, most importantly, will reveal the influence of high turbulent flow fields on ignition characteristics of the lubricant oil droplets. Later, the information coming from the engine CFD model will be used for developing strategies to control and mitigate the abnormal combustion caused by the lubricant oil droplets in natural gas engines.

The work in this dissertation, can help in improving engine efficiency and meeting the high-power density demands of stationary natural gas engines along with aiding in the net zero carbon emission targets.

BIBLIOGRAPHY

[1] U.S. Energy Information Administration, "Annual Energy Outlook 2014 with Projections to 2040," DOE/EIA-0383(2014), 2014.

[2] U.S. Environmental Protection Agency, "EPA and NHTSA Adopt First-Ever Program to Reduce Greenhouse Gas Emissions and Improve Fuel Efficiency of Medium- and Heavy-Duty Vehicles," EPA-420-F-11-031, 2011.

[3] U.S. Environmental Protection Agency, "EPA and NHTSA Set Standards to Reduce Greenhouse Gases and Improve Fuel Economy for Model Years 2017-2025 Cars and Light Trucks," EPA-420-F-12-051, 2012.

[4] D. Serrano and L. Bertrand, "Exploring the Potential of Dual Fuel Diesel-CNG Combustion for Passenger Car Engine," in Proc. FISITA 2012 World Automotive Congress, 2012.

[5] Hockett, A., “A Computational and Experimental Study on Combustion Processes in Natural Gas/Diesel Dual Fuel Engines,” (Colorado State University, 2015).

[6] Hockett, A., Hampson, G. & Marchese, “A. Development and Validation of a Reduced Chemical Kinetic Mechanism for CFD Simulations of Natural Gas/Diesel Dual Fuel Engines,” Energy Fuels 30, (2016).

[7] Curran, H. J., Gaffuri, P., Pitz, W. J. & Westbrook, C. K., “A Comprehensive Modeling Study of n-Heptane Oxidation,” Combust. Flame 114, 149–177 (1998).

[8] Curran, H. J., Gaffuri, P., Pitz, W. J. & Westbrook, C. K, “A comprehensive modeling study of iso-octane oxidation,” Combust. Flame 129, 253–280 (2002).

[9] Healy, D. et al. “Oxidation of C1−C5 Alkane Quinternary Natural Gas Mixtures at High Pressures,” Energy Fuels 24, 1521–1528 (2010).

[10] Niemeyer, K. E., Sung, C.-J. & Raju, M. P, “Skeletal mechanism generation for surrogate fuels using directed relation graph with error propagation and sensitivity analysis,” Combust. Flame 157, 1760–1770 (2010).

[11] Palaveev, S., Magar, M., Kubach, H., Schiessl, R. et al., "Premature Flame Initiation in a Turbocharged DISI Engine - Numerical and Experimental Investigations," SAE Int. J. Engines 6(1):54-66, 2013.

[12] Günther, M., Tröger, R., Kratzsch, M. et al., “Enthalpy-based Approach to Quantifying and Preventing Pre-ignition,” MTZ Worldw 72, 42–47 (2011).

[13] Sasaki, N., Nakata, K., Kawatake, K., Sagawa, S. et al., "The Effect of Fuel Compounds on Pre-ignition under High Temperature and High Pressure Condition," SAE Technical Paper 2011-01-1984, 2011.

[14] Zahdeh, A., Rothenberger, P., Nguyen, W., Anbarasu, M. et al., "Fundamental Approach to Investigate Pre-Ignition in Boosted SI Engines," SAE Int. J. Engines 4(1):246-273, 2011.

[15] Inoue, T., Inoue, Y., and Ishikawa, M., "Abnormal Combustion in a Highly Boosted SI Engine - The Occurrence of Super Knock," SAE Technical Paper 2012-01-1141, 2012.

[16] Zaccardi, J.-M. et al., “Investigations on the Effects of In-Cylinder Charge Motion and Injection Mode on Pre-Ignition in Highly Boosted Spark Ignition Engines”, Aachener Kolloquium Fahrzeug- und Motorentechnik, 2010.

[17] Amann, M., Mehta, D., and Alger, T., "Engine Operating Condition and Gasoline Fuel Composition Effects on Low-Speed Pre-Ignition in High-Performance Spark Ignited Gasoline Engines," SAE Int. J. Engines 4(1):274-285, 2011.

[18] Willand, J., Daniel, M., Montefrancesco, E. et al, “Grenzen des Downsizing bei Ottomotoren durch Vorentflammungen,” MTZ Motortech Z 70, 422–428 (2009). https://doi.org/10.1007/BF03225495.

[19] Zahdeh, A., Rothenberger, P., Schäfer, J., “Diagnosing engine combustion using high speed photography in conjunction with CFD”, 8th International Symposium on Combustion Diagnostics, 2008

[20] Kalghatgi, Gautam & Bradley, Derek & Andrae, J. & Harrison, A.J.. (2009), “The nature of "superknock" and its origins in SI engines,” Institution of Mechanical Engineers - Internal Combustion Engines: Performance, Fuel Economy and Emissions. 259-269.

[21] Park, Sangki, et al. "Effects of various lubricants and fuels on pre-ignition in a turbocharged direct-injection spark-ignition engine." Energy & Fuels 31.11 (2017): 12701-12711.

[22] Dahnz, Christoph, et al. “Investigations on Pre-Ignition in Highly Supercharged SI Engines.” SAE International Journal of Engines, vol. 3, no. 1, 2010, pp. 214–24. JSTOR, http://www.jstor.org/stable/26275479. Accessed 15 Sep. 2022.

[23] Okada, Y., Miyashita, S., Izumi, Y., and Hayakawa, Y., "Study of Low-Speed Pre-Ignition in Boosted Spark Ignition Engine," SAE Int. J. Engines 7(2):584-594, 2014.

[24] Hirano, S., Yamashita, M., Fujimoto, K., and Kato, K., "Investigation of Engine Oil Effect on Abnormal Combustion in Turbocharged Direct Injection - Spark Ignition Engines (Part 2)," SAE Technical Paper 2013-01-2569, 2013.

[25] Takeuchi, K., Fujimoto, K., Hirano, S., and Yamashita, M., "Investigation of Engine Oil Effect on Abnormal Combustion in Turbocharged Direct Injection - Spark Ignition Engines," SAE Int. J. Fuels Lubr. 5(3):1017-1024, 2012.

[26] Onodera, K., Kato, T., Ogano, S., Fujimoto, K. et al., "Engine Oil Formulation Technology to Prevent Pre-ignition in Turbocharged Direct Injection Spark Ignition Engines," SAE Technical Paper 2015-01-2027, 2015.

[27] Ritchie, A., Boese, D., and Young, A., "Controlling Low-Speed Pre-Ignition in Modern Automotive Equipment Part 3: Identification of Key Additive Component Types and Other Lubricant Composition Effects on Low-Speed Pre-Ignition," SAE Int. J. Engines 9(2):832-840, 2016.

[28] Fletcher, K., Dingwell, L., Yang, K., Lam, W. et al., "Engine Oil Additive Impacts on Low Speed Pre-Ignition," SAE Int. J. Fuels Lubr. 9(3):612-620, 2016.

[29] Kocsis, M., Briggs, T., and Anderson, G., "The Impact of Lubricant Volatility, Viscosity and Detergent Chemistry on Low Speed Pre-Ignition Behavior," SAE Int. J. Engines 10(3):1019-1035, 2017.

[30] Zhu, S., Sotiropoulou, E., Tozzi, L. & Yasueda, S, "A Method for Developing Countermeasures to Lube-oil Pre-ignition in Gas Engines." MTZ Ind. 5, 54–61 (2015).

[31] Zhu, D. S., Sotiropoulou, E., Harral, J. K. A. & Zhao, L. "Overcoming Lubricating Oil Preignition in Natural Gas Engines with a Novel Lean-Burn Precombustion Chamber (2017)".

[32] Sullivan, M. P., "Study of lubrication oil ignition in a rapid compression machine under sporadic pre-ignition conditions," Massachusetts Institute of Technology, 2015.

[33] Ohtomo, M. et al., "Fundamental analysis on auto-ignition condition of a lubricant oil droplet for understanding a mechanism of low-speed pre-ignition in highly charged spark-ignition engines"., Int. J. Engine Res. 20, 292–303 (2019).

[34] Fei, S., Wang, Z., Qi, Y. & Wang, Y, "Investigation on Ignition of a Single Lubricating Oil Droplet in Premixed Combustible Mixture at Engine-Relevant Conditions," SAE Tech. Pap. (2019) doi:10.4271/2019-01-0298.

[35] Takayuki Hirose, Yutaka Masuda, Takeshi Yamada, Yoshiyuki Umemoto, "Development of 2-Stroke Gas Engine with Low Pressure Gas Injection," Marine Engineering, 2014, Volume 49, Issue 1, Pages 7-12, Released on J-STAGE July 07, 2015, Online ISSN 1884-3778, Print ISSN 1346-1427, https://doi.org/10.5988/jime.49.7.

[36] Yi, P. et al, "Investigation of evaporation and auto-ignition of isolated lubricating oil droplets in natural gas engine in-cylinder conditions," Fuel 235, 1172–1183 (2019).

[37] Kim, H., Baek, S. W. & Chang, D, "A single n-heptane droplet behavior in rapid compression machine," Int. J. Heat Mass Transf. 69, 247–255 (2014).

[38] Kim, H., Baek, S. W. & Chang, D, "Auto-Ignition Characteristics of Single n -Heptane Droplet in a Rapid Compression Machine," Combust Sci Technol 2014186912–27 Doi10108000102202201489059 8.

[39] Kim, H. & Baek, S. W, "Combustion of a single emulsion fuel droplet in a rapid compression machine," Energy 106, 422–430 (2016).

[40] Kim, T., Baek & Han, S, "Ignition of a Binary Component Fuel Droplet in a Rapid Compression Machine: Comparative Analysis," Combust. Sci. Technol. 187, (2015).

[41] Colin, G, "Dual-fuel combustion of hydrocarbon fuel droplets in lean, premixed methane/oxidizer mixtures in a rapid compression machine," Colroado State University, 2018.

[42] Niegemann, P., Herzler, J., Fikri, M. & Schulz, C, "Studying the influence of single droplets on fuel/air ignition in a high-pressure shock tube," Rev. Sci. Instrum. 91, 105107 (2020).

[43] Godsave, G. A. E, “Studies of the combustion of drops in a fuel spray—the burning of single drops of fuel,” Symp. Int. Combust. 4, 818–830 (1953).

[44] Faeth, G. M. & Olson, D. R. The Ignition of Hydrocarbon Fuel Droplets in Air. SAE Trans. 77, 1793–1802 (1968).

[45] Marchese, A., Vaughn, T., Kroenlein, K. & Dryer, F. Ignition delay of fatty acid methyl ester fuel droplets: Microgravity experiments and detailed numerical modeling. Proc. Combust. Inst. 33, 2021–2030 (2011).

[46] Yang, J. C., Chien, W., King, M. & Grosshandler, “W. L. A simple piezoelectric droplet generator,” Exp. Fluids 23, 445–447 (1997).

[47] Vaughn, T., Wessel, M. & Marchese, A, “Combustion and ignition of bio-ester fuel droplets in microgravity,” 5, 2606–2616 (2007).

[48] Brett, L., Macnamara, J., Musch, P. & Simmie, J. M, “Simulation of methane autoignition in a rapid compression machine with creviced pistons,” Combust. Flame 124, 326–329 (2001).

[49] Healy, D. et al., “Methane/ethane/propane mixture oxidation at high pressures and at high, intermediate and low temperatures,” Combust. Flame 155, 441–448 (2008).

[50] Jeffrey Mohr, “Effect of fuel reactivity and exhaust gas recirculation on knock propensity of natural gas,” Colorado State University, 2020.

[51] Dumitrache, C. et al, “A study of laser induced ignition of methane–air mixtures inside a Rapid Compression Machine,” Proc. Combust. Inst. 36, 3431–3439 (2017).

[52] Law, C.K., “Combustion Physics,” Cambridge University Press (2010).

[53] V. Deprédurand, G. Castanet, F. Lemoine, “Heat and mass transfer in evaporating droplets in interaction: Influence of the fuel,” International Journal of Heat and Mass Transfer, Volume 53, Issues 17–18 (2010)

[54] T. L. Bergman, A. S. Lavine, and F. P. Incropera, “Fundamentals of Heat and Mass Transfer, 7th Edition,” John Wiley & Sons, Incorporated, 2011.

[55] Pinheiro, A.P.,Vedovoto,J.M, “Evaluation of Droplet Evaporation Models and Incorporation of Natural Convection Effects,” Flow Turbulence Combust 102, 537–558 (2019).

[56] Convergent Science Inc., CONVERGE 3.2.0 Theory Manual, 2019.

[57] Z. Han and R. D. Reitz, "Turbulence Modeling of Internal Combustion Engines Using RNG k-e models," Combustion Science and Technology, vol. 106, pp. 267-295, 1995.

[58] B. Launder and D. Spalding, "The Numerical Computation of Turbulent Flows," Computer Methods in Applied Mechanics and Engineering, 1974.

[59] A. Amsden, "KIVA 3-V: A Block Structured KIVA Program for Engines with Vertical or Canted Valves," Los Alamos National Laboratory Report No. LA-13313-MS, 1997.

[60] P. Senecal, E. Pomraning, K. Richards and S. Som, "Grid-convergent spray models for internal combustion engine CFD simulations," in Proc. ASME ICEF, ICEF2012-92043, 2012.

[61] Hockett, Andrew & Hampson, Greg & Marchese, Anthony. (2017), “Natural gas/diesel RCCI CFD simulations using multi-component fuel surrogates,” International Journal of Powertrains. 6. 76. 10.1504/IJPT.2017.082915.

[62] Zdanowicz, A. et al., “End-gas autoignition fraction and flame propagation rate in laser-ignited primary reference fuel mixtures at elevated temperature and pressure,” Combust. Flame 234, 111661 (2021).

[63] Turns, S.R., “An Introduction to Combustion: Concepts and Applications,” McGraw-Hill, New York, 1996.